UNIVERSITY OF COPENHAGEN

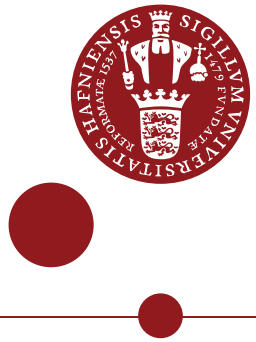

MSc in Physics

τ Decay Mode Identification in a Liquid Argon Electromagnetic Calorimeter at the FCC-ee

Katinka Wandall-Christensen

Supervised by Mogens Dam

December 13, 2021

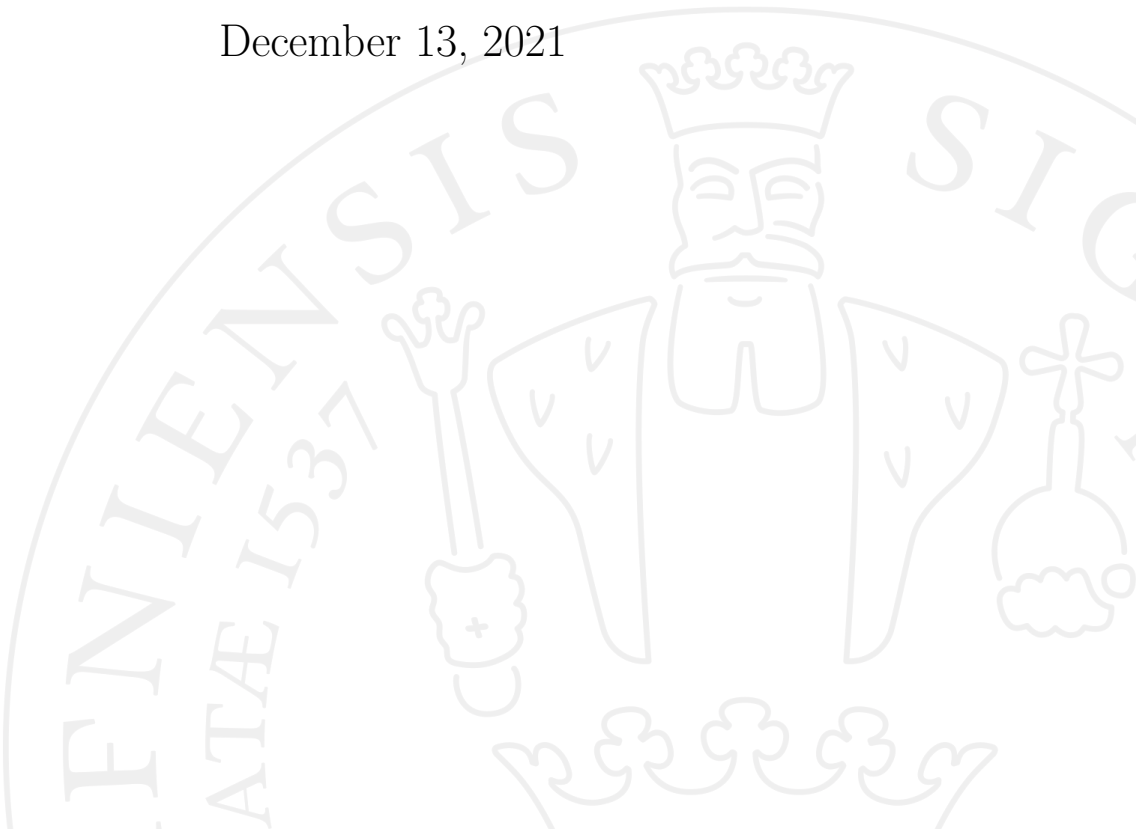

Katinka Wandall-Christensen

τ Decay Mode Identification in a Liquid Argon Electromagnetic Calorimeter at the FCC-ee

MSc in Physics, December 13, 2021

Supervisors: Mogens Dam

University of Copenhagen

Faculty of Science

Niels Bohr Institute

Blegdamsvej 17

2100 Copenhagen Ø

Abstract

Particle physics is entering a new era. From spending the last decades establishing the Standard Model (SM) the focus has now shifted towards answering the remaining open questions of the theory. With this new target in mind, scientists all around the world are designing the next generation of collider experiments. At CERN the highest-priority post-LHC accelerator is the Future Circular Colliders (FCC) [1] . In its first stage the 100 km tunnel will host an extreme luminosity electron-position collider (FCC-ee), covering the interesting energy range from the Z peak to the $t\bar{t}$ production threshold. The second stage will be a hadron-hadron collider (FCC-hh) with collisions reaching unprecedented energies of $\sqrt{s} = 100$ TeV.
One of the goals of the FCC-ee is gathering high precision measurements of key SM parameters [2]. In order to achieve this goal, it is of vital importance to construct the best detector system possible including a calorimeter system. A potential solution for the electromagnetic calorimeter (ECAL) is based on liquid argon (LAr). A variant of a noble liquid ECAL is currently operated by the ATLAS experiment at CERN and has proven itself highly stable with good energy resolution, linearity and uniformity indicating fine prospects for this technology [3]. The requirements at FCC-ee are rather different than at the LHC and it is therefore crucial to investigate whether the suggested solution satisfies these new requirements. This study investigates the performance of such a calorimeter for the particularly challenging task of achieving a clean and well-understood separation of the different hadronic decay modes of the τ lepton. Simulation studies of the proposed calorimeter is performed by first concentrating on single particle studies and subsequently on full τ decays. A key part of the analysis is a π^0 reconstruction method, which can only be achieved with a high performance ECAL. The study suggests that the performance of the LAr ECAL is indeed appropriate and the design remains an interesting calorimeter option for the FCC-ee. Especially its fine granularity, high energy resolution and low noise levels are essential properties. A liquid krypton (LKr) ECAL design is also investigated and the performances of the noble gas options are compared.

Acknowledgements

I would like to thank the people that made this study possible. First and foremost, I would like to thank my supervisor Mogens Dam for his guidance and help with the project. I am grateful for the interesting physics discussions we have had throughout the process, as well as his expertise and countless inputs and suggestions regarding the analysis.
I would also like to thank Clement Helsens and the rest of the Noble Liquid Calorimetry working group for their cooperation and help.
A special thanks to my fiancée August Lohse for his support, patience and help during the past year. His encouragements, energy and all the meals he cooked me on evenings of working late helped me to complete the thesis.
Lastly, a thanks to my good friends Marie Cornelius Hansen and Frederik Guldaager Lund for reading my analysis and giving feedback. Also a thanks to Arnau Morancho for the nice study sessions, breaks and the loads of chocolate.

Contents

1 Introduction

Particle physics describes the smallest constituents of the universe. These objects, called elementary particles, and their interactions are described by the Standard Model (SM). Scientists has spend the last decades developing the model and today it describes most phenomena observed in collider experiments. The latest validation of the theory was the discovery of the Higgs boson in 2012 [4] [5]. Nonetheless, several experimental measurements cannot be explained by the model. It is therefore a pivotal moment in the history of particle physics where the focus has shifted towards testing the Standard Model and searching for the missing elements. Eventually, this search might propose a need for new physics.

The Standard Model does not provide any clues to what the potential new physics might be or how to probe it, but an interesting opportunity is precision measurements of Standard Model parameters. Precision measurements enables testing of the consistency of theory to unprecedented orders of magnitude. If the theory does not hold, precision measurements might help guide the further search for new physics or even reveal it directly [2]. There are many areas where such measurements could be interesting. One of them is τ physics. Precision measurements of the τ lepton and especially of the τ polarisation allow studies of the weak mixing angle and the, until the present day, assumed $e - \tau$ universality [6]. The former is one of the principal parameters in the electroweak sector of the Standard Model and the latter is a central concept stating that the leptons couple with equal strength to the force-carring Z boson.
Conduction of these precision measurements demands suitable experiments. For this purpose, scientists at Conseil Européen pour la Recherche Nucléaire (CERN) and all around the world have begun designing a new accelerator - the Future Circular Colliders (FCC). This integrated accelerator programme will consist of two collider stages: an electron-positron collider (FCC-ee) and a hadron-hadron collider (FCC-hh). The combination of the two colliders allows for an extremely wide search. The electron-position collider will provide extreme luminosities and thereby statistics in the energy range from the Z peak to the $t\bar{t}$ production threshold making it well suited for the precision measurement approach, whereas the high energies reached in the

hadron collider (up to $\sqrt{s} = 100$ TeV) encourages a direct search for new particles [1]. The first collisions at the FCC-ee are scheduled to occur in the 2040s. At the time of writing, the main focus is thus conducting feasibility studies as well as determining the exact design of the detectors, which will be placed at the accelerator's collision points. The latter is the focus of this thesis.

Currently, two main detector concepts are planned for the FCC-ee: The IDEA and CLD detector concepts [2]. They each consist of several sub-detectors which should all be optimized individually. One of these sub-detectors is the electromagnetic calorimeter (ECAL) which measures the energies of e.g. electrons and photons. The Noble Liquid Calorimetry working group at CERN has proposed a new design for a state-of-the-art detector, inspired by the current sampling ECAL in the ATLAS experiment. It will consist of layers of lead and liquid argon (LAr) with a high energy resolution and granularity which fulfills some of the central requirements for a new detector [3].
A high performance ECAL is especially important for future τ polarisation measurements. The precision of these measurements heavily depends on the ability to obtain a clean and well-understood separation of the τ decay modes in addition to measuring the energies of the daughter particles. The former is not a trivial task due to the presence of many close-by particles, making examining the best possible separation a good benchmark for the ECAL performance. This thesis presents a method for obtaining the inter-channel separation for the brand new LAr ECAL design by starting at the most primal analysis level of shower reconstruction, performed by a specially developed clustering algorithm. Building the analysis tools completely from scratch is necessary since no current methods are yet developed for this ECAL geometry. Following the shower reconstruction is a particle identification scheme and a π^0 reconstruction method, which is one of the most central elements of this analysis. Collectively, these methods enable the desired decay channel identification.

The study also investigates the performance of a tungsten and liquid krypton ECAL design as well as a revised LAr and lead design with finer granularity. The goal of this alternate analysis is indicating and comparing the performances of the different ECAL designs.

2 The Standard Model and beyond

The Standard Model (SM) describes our current day understanding of Natures most fundamental building blocks, the elementary particles. The elementary particles are believed to be the smallest constituents of the observable universe, which, according to the model, can be constructed from just 12 matter particles and five force carrying particles. The models' success is especially due to its unifying structure and the verifiability is allows. Since its first formulation in the early 1970s numerous experiments have tested and consolidated its predictions. An overview of the SM particles along with their properties and interactions can be seen in Figure 2.1 and Figure 2.2.

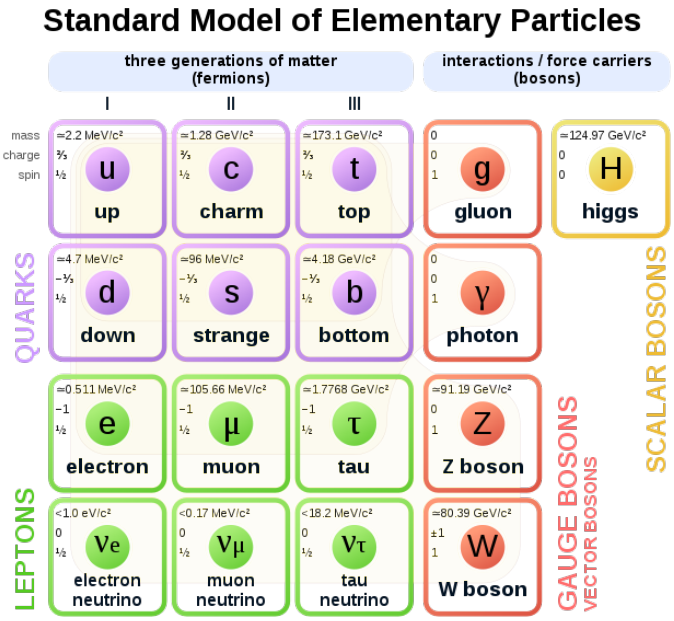

Figure 2.1: The particles of the Standard Model and their properties [7]

The two principle particles species of the theory are the fermions (matter particles) and the bosons (force-carrying particles). The fermions all have spin-$\frac{1}{2}$ and they are arranged in three generations based on their internal mass hierarchy, with the first generation being the lightest. Each generation consists of four particles: an up-type quark carrying charge $+\frac{2}{3}$, a down-type quark carrying charge $-\frac{1}{3}$, a charged lepton

carrying charge -1, and a neutral lepton (a neutrino). The first generation consists of the up-quark, the down-quark, the electron and the electron neutrino. They are the most common elementary particles in our Universe and engage in many well-known physical mechanisms and phenomena for example the hydrogen atom.
For each fermion there exisists an anti-particle with the same mass but opposite electrical (and colour) charge. The anti-particles behave much like their corresponding particle and participate in the same interactions.

The boson group consists of four Gauge bosons: the gluon, the photon, the Z and $W^{\pm}$ bosons, and one scalar boson: the Higgs boson. The Gauge bosons have spin 1 and mediate the weak, the strong and the electromagnetic interactions. These are the three of the four basic interactions in nature. Gravity is not yet embedded in the framework of the SM but with the small masses of the SM particles, its influence can anyway be neglected here.

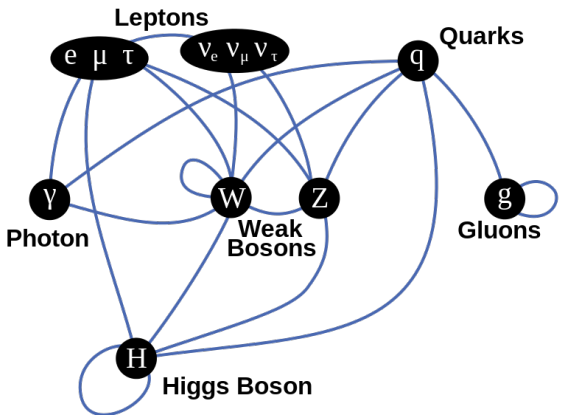

Figure 2.2: Interactions of the Standard Model particles [8]

The electromagnetic interaction is mediated by the photon. All electrically charged fermions can undergo this interaction and since photons are massless and can propagate freely, the range of the force is infinite.
The associated gauge bosons of the weak interaction are the Z and the $W^{\pm}$ bosons. The weak neutral-current interaction is mediated by the Z boson and the charged-current weak interaction is mediated by with the $W^{\pm}$ bosons. All fermions experience the weak force and the range of force is about 10^{-18} m, which is largely due to the heavy mass of the W bosons as the propagator of the particle has a $1/m_{\mathrm{W}}^2$ dependence with $m_{\mathrm{W}} \approx 80$ GeV. This is what makes the weak interaction weak.
The strong force is the interaction seen between coloured objects such as the quarks. It earns its name by being the strongest of the four forces within the distance of 1 fm. The strength of the force increases with growing distance which is a very special property for this force and ultimately leads to the formation of hadrons. The associated boson is the gluon. The massless gluons do not propogate freely due to a phenomenon called colour confinement. The strong force therefore has a finite range of approximately 10^{-15} m(1 fm) corresponding roughly to the size of a nucleus [9].

The only scalar boson in the SM is the Higgs boson. It has spin-0 and no electrical charge. It is through interactions with the Higgs field that all SM paricles gain their mass. This process is described in the Higgs mechanism which was proposed by the physicist Peter Higgs and others in 1964 [10]. The experimental discovery of the Higgs boson by the CMS and ATLAS experiments at the Large Hadron Collider (LHC) at CERN is one of the strongest arguments supporting the Standard Model [4] [5].

2.1 Quantum Field Theories

Quantum Field Theory (QTF) is the mathematical framework behind the SM and combines special relativity, quantum mechanics and field theory. QFT treats the physical particles as excitations of quantum fields, and interactions and dynamics are described by the Lagrangian formalism. Two central quantum field theories in the SM are quantum electro dynamics (QED) and quantum chromo dynamics (QCD). QED describes the interactions between charged particles and an electromagnetic field, whereas QCD describes the interactions of the strong force. This section presents key aspects of the QFTs as well as defining symmetries in the SM.

The Lagrangian formalism

The dynamics of a classical system can be described by specifying the Lagrangian and obtaining the equations of motion using the Euler-Lagrange equation [11]. The Lagrangian is defined as

$$L\left(q_i, \frac{\mathrm{d}q_i}{\mathrm{d}t}\right) = T - V \ , \tag{2.1}$$

with T and V being the kinetic and potential energy, respectively. Here q_i is a set of generalized coordinates. In QFT, these discrete coordinates are replaced by continues fields. The Lagrangian is then redefined as

$$L\left(q_i, \frac{\mathrm{d}q_i}{\mathrm{d}t}\right) \rightarrow \mathcal{L}(\theta_i, \partial_\mu \theta_i), \tag{2.2}$$

with $\theta_i = \theta_i(t, x, y, z)$ being continues fields in space-time, and $\partial_\mu \theta_i$ the derivative defined as $\partial_\mu \theta_i \equiv \frac{\partial \theta_i}{\partial x^\mu}$. The resulting Euler-Lagrange equation becomes

$$\partial_\mu \left(\frac{\partial \mathcal{L}}{\partial(\partial_\mu \theta_i)} \right) - \frac{\partial \mathcal{L}}{\partial \theta_i} = 0. \tag{2.3}$$

The Dirac equation

The fermion fields in QFT are described by the Dirac equation. To provide a unification of special relativity and quantum mechanics, the Dirac equation needs to be Lorentz invariant. This is a necessity that is not upholded by the Schrödinger equation since it is not first order derivative of both space and time. The Dirac equation, being first order derivative of both space and time, is formulated in the covariant way

$$(i\gamma^\mu \partial_\mu - m)\psi = 0, \tag{2.4}$$

with γ^μ being the four Dirac γ-matrices. These matrices are indeed Lorentz invariant and can be built using the three 2×2 Pauli spin matrices.

The solutions to the Dirac equation are four component wavefunctions and represent spin-$\frac{1}{2}$ particles. These Dirac spinors are defined as:

$$\psi = \begin{pmatrix} \psi_1 \\ \psi_2 \\ \psi_3 \\ \psi_4 \end{pmatrix} \tag{2.5}$$

and are linear combinations of two eigenspinors: the spin-up and spin-down states. There is a spin-up and spin-down state for both the negative and postive energy solution to the Dirac equation. Since quantum mechanics demands a complete set of basis states, the negative energy solutions cannot be discarded and these solutions are instead interpreted as the anti-particles [9] [11].

The Local Gauge Principle

The demand of local gauge invariance is central in the SM. Gerard t'Hooft showed that only theories upholding local gauge invariance are renormalisable [9]. As a consequence of this extremely powerfull statement, all QFT's of the SM must fulfill this symmetry. When enforcing it, it gives rise to the gauge bosons. Local gauge invariance is introduced by requiring either U(1) (for QED), SU(2) (for the weak interaction) or SU(3) (for QCD) local phase invariance of the fields. U(1), SU(2) and SU(3) are the gauge groups of the QFT's. An example is electrodynamics where the underlying symmetry group is the U(1) group. The requirement of U(1) local phase invariance in this theory gives rise to a new vector field A_μ, which interacts with the fermion field. The transformation of these fields are

$$\psi(x) \rightarrow \psi'(x) = e^{iq\chi(x)}\psi(x) \tag{2.6}$$

$$A_\mu \rightarrow A'_\mu = A_\mu - \partial_\mu \chi(x)\ , \tag{2.7}$$

where $q\chi(x)$ is a phase which can take different values in all points of space-time. The transformations exactly describe the gauge field of the photon and thereby the interactions of the photon and the electron in the requested renormalisable way. Following this logic it can be shown that the QED Lagrangian can be formulated as

$$\mathcal{L}_{QED} = \bar{\psi}\left(i\gamma^\mu D_\mu - m_e\right)\psi - \frac{1}{4}F_{\mu\nu}F^{\mu\nu}, \tag{2.8}$$

where the normal derivative ∂_μ has been replaced by the covariant derivative

$$\partial_\mu \rightarrow D_\mu = \partial_\mu + iqA_\mu\ , \tag{2.9}$$

in order to satisfy the local gauge invariance. This is an important result, but the request for local symmetry has consequences beyond the QED formulation. It ultimately leads to the entire SM being invariant under

$$SU(3) \times SU(2) \times U(1) \tag{2.10}$$

gauge transformations [9].

Helicity and Chirality

Quantum numbers correspond to conserved quantities of quantum mechanical systems. For example, in non-relativistic quantum mechanics, the spin along the z-axis is used as a quantum number. In relativistic quantum mechanics, however, only spin measured along the direction of momentum is a good quantum number. This quantity is called helicity and is defined as

$$h \equiv \frac{\mathbf{S}\cdot\mathbf{p}}{p}, \tag{2.11}$$

where $\mathbf{S}$ and $\mathbf{p}$ are the spin and the momentum of the particle, respectively. Helicity has eigenvalues $\pm 1/2$, and the two states are called right-handed and left-handed. Because helicity depends on the direction of motion, it cannot be invariant under Lorentz transformations for massive particles, as reversing the direction of the particle will switch the helicity. A non-geometrical but Lorentz invariant quantity, chirality, is therefore introduced for all fermions.
Chirality is defined as the eigenstates of the γ^5-matrix which is constructed of the Dirac matrices, $\gamma^5 = i\gamma^0\gamma^1\gamma^2\gamma^3$. Its eigenvalues are $+1$ and -1 and correspond to right-handed and left-handed chiral states, respectively. Helicity and chiral states are identical in the limit where masses of the particles can be neglected, i.e. the relativistic limit [9] [11].

2.1.1 The Electroweak Unification

Electroweak unification is a theory within the SM that combines the weak interaction with QED. It was developed in the 1960s by Glashow, Salam and Weinberg (GSW). The symmetry group describing the weak charged-current interaction is the $\mathrm{SU}(2)_L$ group. The L indicates that the gauge transformation is only for left-handed particles and right-handed anti-particles, corresponding to the V-A structure of the charged-current weak interaction. By requiring invariance under SU(2) local phase transformations, it is necessary to introduce three new gauge fields $W^1_\mu, W^2_\mu, W^3_\mu$ to insure that the Dirac equation is still fulfilling local gauge invariance. The first two gauge fields can be associated with the $W^\pm$ bosons and the third gauge field with a

linear combination of the photon and Z boson. The physical W bosons mediating the weak charged-current interactions are described by

$$\mathrm{W}_{\mu}^{\pm} = \frac{1}{\sqrt{2}}\left(\mathrm{W}_{\mu}^{(1)} \mp i\mathrm{W}_{\mu}^{(2)}\right) \quad , \tag{2.12}$$

which means that they are a combination two fields.

The same applies to the the photon and the Z boson. Their fields, A_μ and Z_μ, can be described by a linear combination of the third vector field W_μ^3 and another field B_μ. The new field B_μ was introduced by GSW to replace the U(1) symmetry group of QED with the $\mathrm{U}(1)_Y$ local gauge symmetry. Y indicates that the field couples to weak hypercharge. Using these fields, the photon and the Z boson can, in the unified electroweak theory, be described as:

$$A_\mu = B_\mu \cos\theta_W + W_\mu^{(3)} \sin\theta_W \tag{2.13}$$

and

$$Z_\mu = -B_\mu \sin\theta_W + W_\mu^{(3)} \cos\theta_W, \tag{2.14}$$

with θ_W being the weak mixing angle. This unification indicates a relationship between the coupling constants of the weak and the electromagnetic interaction. The relation can be given as a function of the weak mixing angle:

$$e = g_W \sin\theta_W = g' \cos\theta_W \tag{2.15}$$

with the weak hypercharge given as $Y = 2Q - 2I_W^{(3)}$. The weak mixing angle is vitally important in the electroweak model as it can be used to describe the relation between the coupling of the weak and electromagnetic couplings. It also plays a central role in determining the coupling strength of the Z boson to fermions. The coupling of the Z boson is

$$g_{\mathrm{Z}} = \frac{g_{\mathrm{W}}}{\cos\theta_{\mathrm{W}}} \equiv \frac{e}{\sin\theta_{\mathrm{W}}\cos\theta_{\mathrm{W}}}. \tag{2.16}$$

This can be used to determine the form of the neutral-current of the Z boson and furthermore its coupling to LH and RH chiral states:

$$j_{\mathrm{Z}}^{\mu} = \frac{1}{2} g_{\mathrm{Z}} \bar{u}\left(c_V \gamma^{\mu} - c_A \gamma^{\mu}\gamma^5\right) u \tag{2.17}$$

with the vector and axial vector couplings

$$c_V = (c_L + c_R) = I_{\mathrm{W}}^{(3)} - 2Q\sin^2\theta_{\mathrm{W}} \, , \qquad c_A = (c_L - c_R) = I_{\mathrm{W}}^{(3)}. \tag{2.18}$$

This shows that the Z boson couples to both LH and RH particle states but with different strengths. The strengths are again determined by the weak mixing angle [9].

2.1.2 Quantum Chromodynamics

Quantum chromodynamics (QCD) is the theory describing the strong interaction. The strong interaction is the interaction seen between coloured objects such as quarks and gluons. The gluons are the mediating gauge boson and arise from the underlying SU(3) symmetry. Requiring local phase invariance forges a need of eight new gauge fields interpreted as the eight gluons. The gluons and their interactions are described by the Lagrangian

$$\mathcal{L}_{QCD} = \bar{\psi}\left(i\gamma^{\mu}D_{\mu} - m\right)\psi - \frac{1}{4}G^{a}_{\mu\nu}G^{\mu\nu a}. \tag{2.19}$$

where D_{μ} is the covariant derivative, analogous to QED. It is described by

$$D_{\mu} = \partial_{\mu} + ig_{\mathrm{s}}T_{a}G^{a}_{\mu}. \tag{2.20}$$

with T_a being the generator of the group and G^a_μ the field.
The eight generators of QCD are represented by 3×3 matrices with three extra degrees of freedom called colour. They are labeled red (r), green (g) and blue (b). Particles will carry colour and anti-particles will carry anti-colours denoted anti-red ($\bar{r}$), anti-green ($\bar{g}$) and anti-blue ($\bar{b}$). The colours are orthogonal in colour space and colour is conserved at all vertices. The states are described by two quantum numbers: colour hypercharge, Y^c, and the third component of the colour isospin, I^c_3.

In order for colour to be conserved at each vertex, gluons must carry both colour and anti-colour charges. The colour charge cannot be chosen randomly as only specific combinations are allowed. Because gluons are related to the generators of the SU(3) group, the eight gluons form an octet coloured state consisting of the following colour combinations:

$$r\bar{g},\ g\bar{r},\ r\bar{b},\ b\bar{r}, g\bar{b},\ b\bar{g},\ \frac{1}{\sqrt{2}}(r\bar{r} - g\bar{g}) \quad \text{and} \quad \frac{1}{\sqrt{6}}(r\bar{r} + g\bar{g} - 2b\bar{b}). \tag{2.21}$$

The non-zero colour charge of the gluons allows them to self-interact. This is a special property of QCD and has several consequences for the theory. They interact with themselves and other particles carrying non-zero colour charges to form colour-less objects as demanded by colour confinement. Colour confinement is a concept stating that only colourless objects i.e. colour singlet states can propagate freely. A singlet state does not only require that net sum of colour quantum numbers of a state is zero. It also demands that the state is invariant under SU(3) colour transformations and additionally, that the ladder operator $T_{\pm}$, $U_{\pm}$ and $V_{\pm}$ (defined in the same way as for SU(3) flavour symmetry) all give zero when used on the state. These impose strict rules for allowed states and explains for example why the propagation of single quarks are not observed in nature.

It is believed, although not yet proven, that colour confinement arises from gluon self-interactions. When two free colour charges are pulled apart, they exchange virtual gluons. Due to self-interactions of these virtual gluons, the colour field between the two colour charges is compressed into a flux tube. The potential of this field is described by $V(\mathbf{r}) \sim \kappa r$ with $\kappa \sim 1$ GeV/fm and r being the distance between them. This relation shows that it would take an infinite amount of energy to separate the two colour charges at an infinite distance. Colour charges such as quarks are therefore always confined in colourless states for example as hadrons [9].

2.2 The Higgs mechanism

The description of the elementary particles and their interactions presented so far have one major problem: the demand of local gauge symmetry can only be met if all particles are massless. It is obvious that this is not true for our Universe. Many ferminos as well as the $W^{\pm}$ and Z bosons are observed to have a non-zero masses. The Higgs mechanism solves the problem by introducing the masses of both fermions and bosons without breaking local gauge invariance.

The SM Higgs mechanism is embedded in the $U(1)_Y \times SU(2)_L$ local gauge symmetry. This symmetry group involves the electroweak sector of the SM. The Higgs potential is a complex scalar field described by:

$$V(\phi) = \mu^2 \phi^\dagger \phi + \lambda (\phi^\dagger \phi)^2, \tag{2.22}$$

with $\mu^2 < 0$. A drawing of the potential of a single complex scalr field can be seen in Figure 2.3.

ϕ in Eq. 2.22 is a weak isospin doublet of two complex scalar fields:

$$\phi = \begin{pmatrix} \phi^+ \\ \phi^0 \end{pmatrix} = \frac{1}{\sqrt{2}} \begin{pmatrix} \phi_1 + i\phi_2 \\ \phi_3 + i\phi_4 \end{pmatrix}. \tag{2.23}$$

Because $\mu^2 < 0$ there is an infinite set of the Higgs potential minima corresponding to the lowest energy states of the field also called the vacuum states (illustrated as the ring of minima for the single complex scalar in Figure 2.3). The Higgs potential minima are given by:

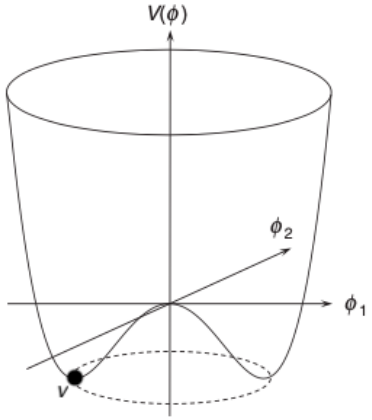

Figure 2.3: Illustration of the Higgs potential for a single complex scalar field [9]

$$\phi^\dagger\phi = \frac{1}{2}\left(\phi_1^2 + \phi_2^2 + \phi_3^2 + \phi_4^2\right) = \frac{v^2}{2} = -\frac{\mu^2}{2\lambda} \tag{2.24}$$

$$\Rightarrow \quad v^2 = \frac{-\mu^2}{\lambda}\ , \tag{2.25}$$

where v is the vacuum expectation value of the Higgs field. It is hugely important for the SM physics. The degenerate set of solutions forces a choosing (by Nature) of vacuum state which spontaneously breaks the symmetry of the Lagrangian. After the spontaneous symmetry breaking, the scalar field doublet can be chosen as

$$\phi(x) = \frac{1}{\sqrt{2}} \begin{pmatrix} 0 \\ v + h(x) \end{pmatrix}, \tag{2.26}$$

using a unitary gauge transformation. This field is no more complex and $h(x)$ now represents the physical Higgs field. The resulting Lagrangian will consist of terms describing the massive Higgs scalar, the massive and massless gauge bosons, the interactions between the Higgs and the scalar bosons and the Higgs self-interactions. From the Lagrangian, the mass of the W bosons are found as

$$m_W = m_Z \cos\theta_W = \frac{1}{2} g_W v \tag{2.27}$$

which shows that the vacuum expectation value of the Higgs field sets the scale for the masses of the electroweak sector of the SM. It's value is determined to be

$$v = 246 \text{ GeV} \tag{2.28}$$

and results in a Higgs mass of

$$m_H \approx 125 \text{ GeV}. \tag{2.29}$$

The fermion masses can furthermore be found using the Higgs mechanism by following the same logic as for the electroweak bosons. Here, it is shown that the Yukawa coupling of the Higgs boson to the ferminons is described by

$$g_f = \sqrt{2}\,\frac{m_f}{v}. \tag{2.30}$$

This suggests that v also sets the scale of the fermion masses. Additionally, it shows that the Higgs couples to all fermions but with a strength proportional to the fermion mass. This proportionality also applies for the gauge bosons [9] [11].

2.3 Open questions and Beyond the Standard Model physics

Regardless of the many compelling arguments supporting the SM, scientists agree that the model does not give a complete description of particle physics. Questions remain that cannot be answered within the current model and these could lead particle physics to new far-reaching discoveries and maybe even new physics.

One sector with many interesting unknowns is the Higgs sector. Because of the boson's important role in the SM, it is essential to fully understand its properties and their origins. Nonetheless, the Higgs boson remains the least understood particle within the theory. Consider for example the vacuum expectation value of the Higgs field, $v = 246$ GeV. This value is not predicted in the SM, but found from Eq. 2.27. As it sets the scale of the masses of the electroweak bosons and the Higgs boson mass itself, the exact value is hugely important. As a result, the mass of the Higgs boson is just $m_{\mathrm{H}} \approx 125$ MeV, which gives rise to the Hierarchy Problem, asking why the weak force seems to be 10^{24} times as strong as gravity. An understanding of the origin of the Higgs potential is necessary to solve this problem [2].
The Higgs boson is the only scalar boson in the SM. Since it does not carry an electric charge or spin it could possibly interact with undiscovered scalar bosons or new particles [12]. Further studies of its branching fractions are therefore of special interest. A potential discovery of so-called exotic Higgs decays or invisible

decays could reveal new physics and maybe even help answer other open questions. Measurements of the total width of the Higgs boson along with precise determinations of its branching fractions would therefore be immensely valuable. However, the lack of observations of exotic decays suggests very small branching fractions, if any, and so a dedicated Higgs factory is needed for these studies.

One of the biggest mysteries of physics concerns the origin and composition of Dark Matter (DM). DM was proposed as the cause of an inconsistency between observations of galaxies' rotation curves and the predicted values. The high rotation velocities suggested a need for additional non-luminous heavy matter (DM), surrounding the galaxies in a halo. Calculations suggest there is 5.4 times more DM than luminous matter in the universe. The SM does not give any indications to what dark matter is or the mass scale of the DM particles. The DM problem is regarded as a strong indication of Beyond the Standard Model (BSM) physics [9] [13].

The insufficiency of the SM is also demonstrated by the presence of flavour violation. Flavour violation was first observed for neutrinos as neutrino oscillations. The weak eigenstate of the neutrino is a linear superposition of three mass eigenstates and hence, it allows the neutrinos to alternate between the flavours, violating the laws of the SM. As a result, the neutrino wavefunction will collapse when the neutrino interacts and a weak eigenstate, i.e. flavour, is chosen. This was a ground-breaking discovery. While it solved the problems for inconsistencies between experimental measurements and predictions, (e.g. the Solar neutrino problem [14]) it also posed new discussions since the phenomenon of neutrino oscillations requires the neutrinos to have a non-zero mass. This is a contradiction to the SM where they are chosen to be massless by convention. Measurements nonetheless supported the neutrinos having a small but non-zero mass. However, a theoretical explanation is still missing [15].

Another open question is the baryon-antibaryon asymmetry. Our universe today is dominated by baryons and not anti-baryons and it is believed that this asymmetry arose in the early universe and cannot have happened without C (charge conjugation) and CP (charge conjugation and parity) violation. The SM only allows for CP violation in the weak interactions of the quark sector but this alone cannot explain the observed asymmetry. The lack of an explanation in the SM again suggests BSM physics.

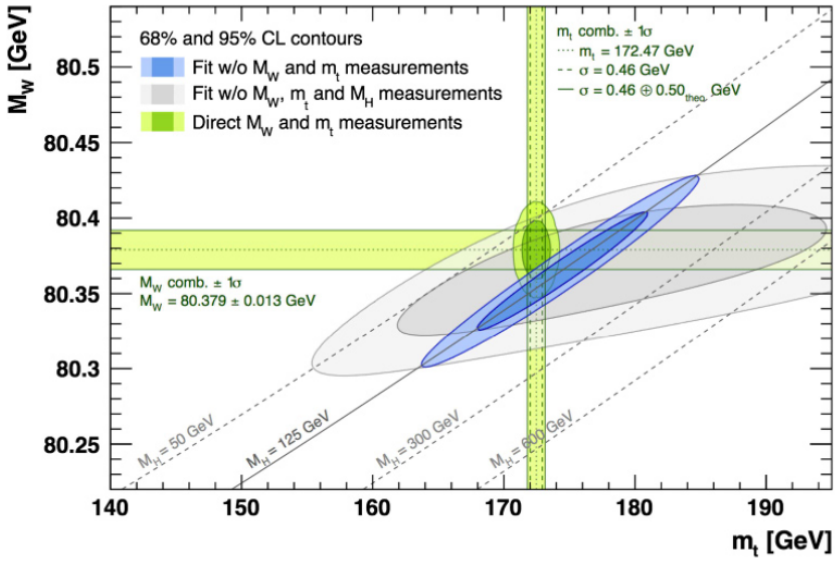

Figure 2.4: A summary of the SM predictions at the 68% and 95% confidence level. The blue ellipse is the result the SM predictions for the W and top quark masses including the measurements Higgs boson mass. The gray area is this prediction without the Higgs mass measurement. The green bands are the direct measurements of the W and top quark masses within 1σ [2].

These questions and more set the agenda for the next period of exploration in the field of particle physics. However, it still needs to be decided where and how to search for BSM physics. One suggestion is through precision measurements of the electro-weak model [2]. The SM consists of several free parameters with values determined by experimental measurements which allows for a comparison to theoretical predictions. Increasing the precision of the measured values thereby automatically tests the consistency of the SM. If breaches or discrepancies are found, they hint a presence of other underlying physics phenomena. This has however not been the case to the present day as measurements have only confirmed SM predictions. This means that effects of potentially undiscovered physics are smaller than current uncertainties which immediately motivates for precision measurements.

The electro-weak model is especially suited for precision measurements since it contains many important free parameters of the SM. The parameters include the masses of the Z and $W^{\pm}$ bosons, the weak mixing angle $\sin^2(\theta_W)$ and the top quark mass. The overall results, their uncertainty and the agreement with the SM predictions can be seen in Figure 5.2 [16]. The results show a consistency between the predicted values (blue ellipse) and the direct measurements (dark green ellipse).

Another option is precision measurements of the τ lepton with a special focus on measurements of its polarisation. Such measurements allows for simultaneous testing of the assumed $e - \tau$ universality of the SM and provide the numerical value of the

key electro-weak model parameter, the weak mixing angle. This thesis concentrates on the τ polarisation approach for which a τ decay mode identification is central.

τ studies

3

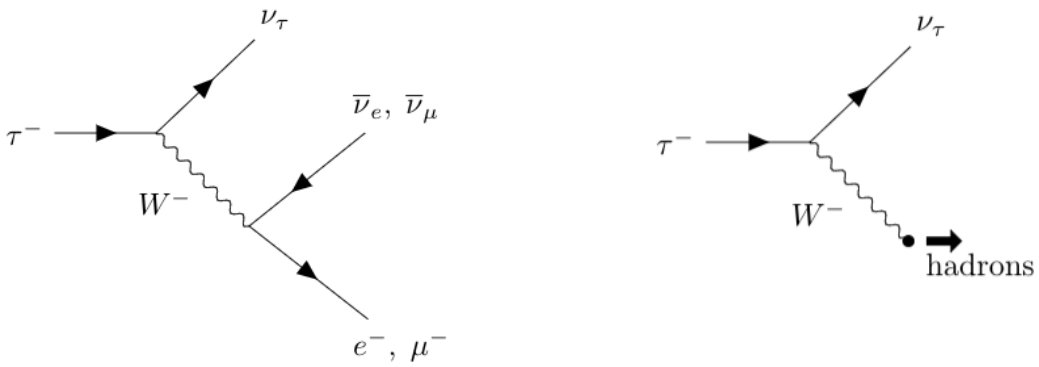

Figure 3.1: The leptonic and hadronic decay channels of the τ lepton

The τ lepton was discovered in 1975 by Martin Lewis Perl (and others), who, in 1995, was awarded the Noble Prize in physics for his work [17]. The τ lepton is the heaviest of the three leptons with a mass of 1.77686 ± 0.00012 GeV [18]. Because of the mass, the mean lifetime of the τ is only $(290.3 \pm 0.5) \times 10^{-15}$ s. Unlike the lighter leptons the τ can decay both hadronically and leptonically because of the sufficiently high mass. Both happen through weak charged-current interactions as shown in Figure 3.1. The τ decays hadronically in $\sim 65\%$ of the cases and leptonically in $\sim 35\%$ of the cases. The branching fractions for the most dominant decays can be seen in Table 3.1. For the hadronic decays, it is seen that the channels mostly differ by the number of π^0's created in an event. Being able to count the number of π^0's is therefore a useful tool for differentiating between the different hadronic final states. However, the π^0 also decays as $\pi^0 \to \gamma\gamma$ which complicates the counting.

3.1 τ polarization measurements

The polarisation of the τ lepton can be studied through asymmetries in the $e^+e^- \to Z \to \tau^+\tau^-$ process. These asymmetries arise from the parity violating nature of the neutral-weak current interaction and means that the Z couples with different strengths to right-handed and left handed helicity states. Because helicity is a conserved quantity, the Z boson only couples to two τ's of opposite helicities. The

Decay modes	Branching fraction [%]
$e^- \bar{\nu}_e \nu_\tau$	17.82 ± 0.04
$\mu^- \bar{\nu}_\mu \nu_\tau$	17.39 ± 0.04
$h^- \nu_\tau$	11.51 ± 0.05
$h^- \pi^0 \nu_\tau$	25.93 ± 0.09
$h^- 2\pi^0 \nu_\tau$	9.48 ± 0.10
$h^- 3\pi^0 \nu_\tau$	1.18 ± 0.07
$h^- 4\pi^0 \nu_\tau$	0.16 ± 0.04
3 prongs	15.20 ± 0.06

Table 3.1: The dominant decay modes and their branching fractions of the τ lepton. h^- represents a K^- or a π^- [18]

resulting two possible final states are thereby: $\tau_R^- \tau_L^+$ or $\tau_L^- \tau_R^+$. Using the helicity states, the longitudinal polarisation asymmetry can be defined as:

$$A^{\text{pol}} = \frac{\sigma_R - \sigma_L}{\sigma_R + \sigma_L}, \tag{3.1}$$

where σ_R and σ_L are the cross-sections for the production of right-handed particle or left-handed particle helicity final states [19]. Eq. 3.1 only applies in the limit $E \gg m$ where chrial and helicity states are identical. Due to parity violation, the left-handed cross section will exceed the right-handed in magnitude. The cross sections are proportional to the squared chiral couplings of the Z boson to the τ's. Hence, the relative difference of the cross sections can be described as:

$$A^{\text{pol}} = \frac{\sigma_R - \sigma_L}{\sigma_R + \sigma_L} = \frac{\left(c_R^\tau\right)^2 - \left(c_L^\tau\right)^2}{\left(c_R^\tau\right)^2 + \left(c_L^\tau\right)^2} = -\mathcal{A}_\tau \tag{3.2}$$

where $\mathcal{A}_\tau$ is the τ asymmetry parameter. It is more generally defined as the fermion asymmetry parameter

$$\mathcal{A}_{\text{f}} = \frac{\left(c_L^{\text{f}}\right)^2 - \left(c_R^{\text{f}}\right)^2}{\left(c_L^{\text{f}}\right)^2 + \left(c_R^{\text{f}}\right)^2} \equiv \frac{2 c_V^{\text{f}} c_A^{\text{f}}}{\left(c_V^{\text{f}}\right)^2 + \left(c_A^{\text{f}}\right)^2} \tag{3.3}$$

with c_V^{f} and c_A^{f} being the vector and axial vector couplings, respectively.

The Z boson also couples asymmetrically to the electron-position helicity states. There are also two allowed states here, giving a total of four allowed combinations for the process, which are shown in Figure 3.3 in the center-of-mass frame of the colliding particles. The unequal coupling to the initial states, results in an angular

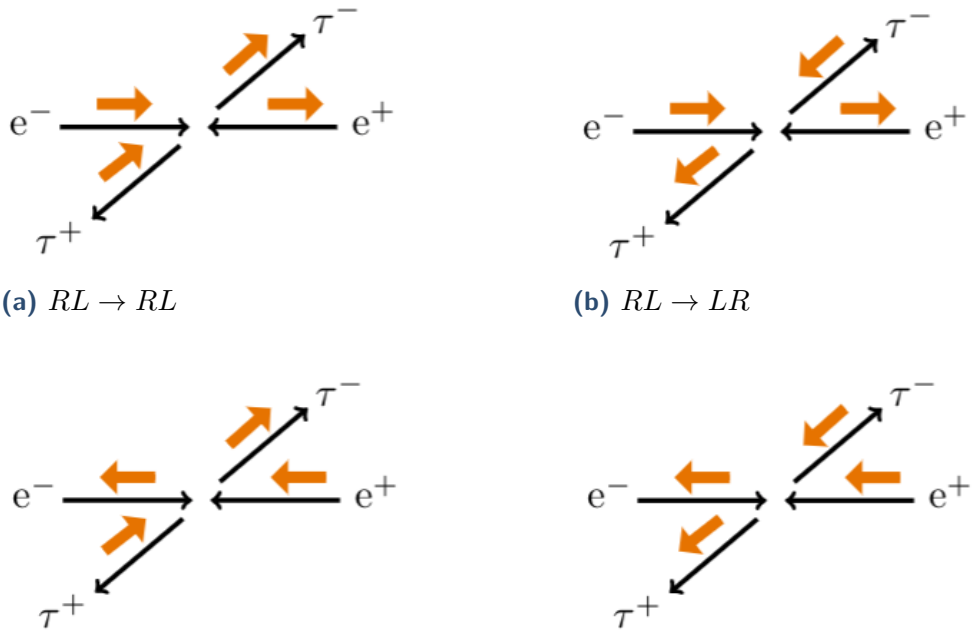

(a) $RL \to RL$ (b) $RL \to LR$

(c) $LR \to RL$ (d) $LR \to LR$

Figure 3.3: Allowed helicity combinations for the $e^+e^- \to Z \to \tau^+\tau^-$ process. The black arrows describe the direction of motion of the particles and the orange arrows their helicities

dependence of total τ polarisation. The total polarisation can be described using the improved Born approximation at the Z peak, which is given by

$$P_\tau(\cos\theta) = -\frac{\mathcal{A}_\tau\,(1+\cos^2\theta) + 2\cos\theta\mathcal{A}_e}{(1+\cos^2\theta) + 2\mathcal{A}_\tau\mathcal{A}_e\cos\theta}, \tag{3.4}$$

where θ is the angle between the e^- beam and the τ^- direction of flight [20]. The mean polarisation is equal to the longitudinal polarisation asymmetry (equal to $-\mathcal{A}_\tau$) whereas the amplitude of the Born approximation will describe its angular dependence determined by the $\mathcal{A}_e$ parameter. This is illustrated in Figure 3.2.

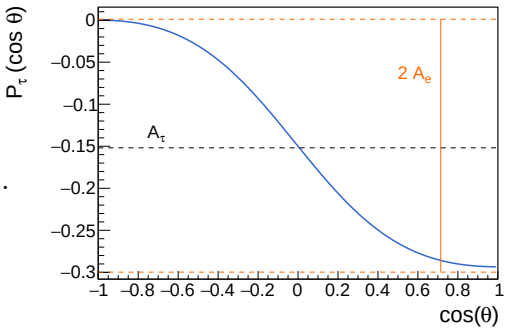

Figure 3.2: The total polarisation $P_\tau(\cos\theta)$ for $\mathcal{A}_e = \mathcal{A}_\tau = 0.15$

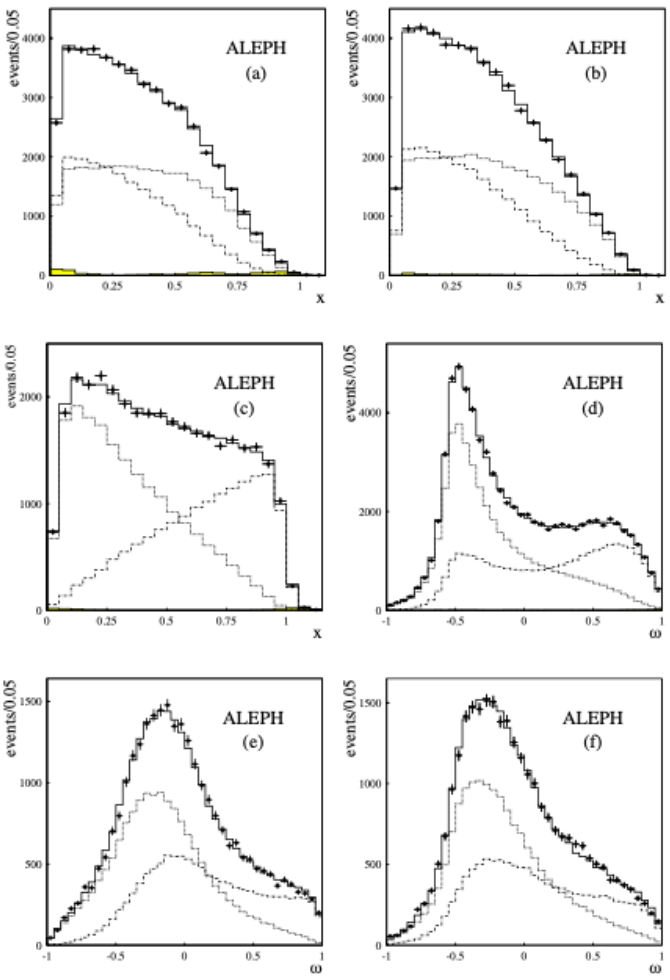

Figure 3.4: Distributions of the x and ω kinematic variables for different τ decay channels. The distributions for only left-handed (dotted line) and right-handed (dash-dotted line) τ's for a perfect $V - A$ coupling are also shown. The shaded area is non-τ background. Decay channel: a) $\tau \to e\nu\bar{\nu}$, b) $\tau \to \mu\nu\bar{\nu}$, c) $\tau \to h\nu$, d) $\tau \to \rho\nu$, e) $\tau \to 3h\nu$, f) $\tau \to h\,2\pi^0\,\nu$ [20]

Eq. 3.4 shows that a measurement of the polarisation demands a measurement of the helicity states and the angular distributions of the particles. Such measurements have been performed by the Apparatus for LEP PHysics (ALEPH) experiment at the Large Electron-Position Collider (LEP) [20]. Here, τ decays were used as spin analysers to determine the fraction of left- and right-handed final state particles.

Figure 3.4 shows two theoretical kinematic distributions for an ensemble of only right- or left-handed particles compared to the experimentally measured values. The kinematic variable x is used for the leptonic channels and the $\tau \to h\nu_\tau$ channel as the τ daughter particles in these channels to not decay. x is defined as the fraction of beam energy carried by the lepton or charged pion, $x = E_{\ell \text{ or } \pi}/E_{beam}$. For the remaining hadronic channels, the parameter ω is used instead. It is a one dimensional combination of two angular distributions θ and ψ. For the rho decay channel, θ is the angle between the emitted rho meson and the τ, whereas ψ is the angle between the rho and the $\pi^\pm$ when it further decays. Experimentally they are described by [21]:

$$\cos\theta \propto \frac{E_{\pi^-} + E_{\pi^0}}{E_{Beam}} \quad \text{and} \quad \cos\psi \propto \frac{E_{\pi^-} - E_{\pi^0}}{E_{\pi^-} + E_{\pi^0}} \ . \tag{3.5}$$

Recon → Gen ↓	$h\,\nu$	$h\,\pi^0\,\nu$	$h\,2\pi^0\nu$	$h\,3\pi^0\nu$	$h\,4\pi^0\nu$
$h\,\nu$	**0.9270**	0.0670	0.0047	0.0010	0.0003
$h\,\pi^0\,\nu$	0.0457	**0.8756**	0.0728	0.0053	0.0006
$h\,2\pi^0\nu$	0.0044	0.1470	**0.7499**	0.0900	0.0087
$h\,3\pi^0\nu$	0.0008	0.0288	0.3098	**0.5768**	0.0837

Table 3.2: The migration matrix of a selection hadronic τ decays obtained at the ALEPH experiment. Each row shows the fraction of e.g. $\tau \to h\,\nu$ decays classified as each of the considered channels [22]

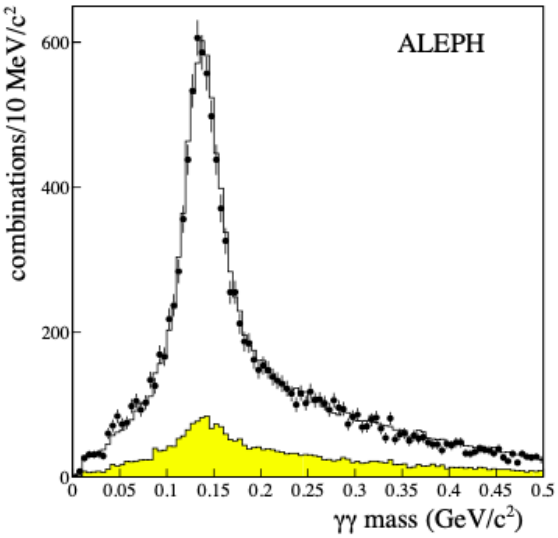

Figure 3.5: The mass of two photons in four photon events, where one π^0 has already been identified. The histogram represents Monte Carlo data and the black circles ALEPH data. The shaded histogram shows the contribution from backgrounds [20]

Before the kinematic fitting can occur, a decay mode identification is done to determine which events belong to which x or ω distribution. The classification is based on the number of reconstructed charged hadrons and π^0's as well as a charged hadron classification. The inter-channel separation results are summarized in the migration matrix shown in Table 3.2. For simplicity, only the channels relevant for this thesis are presented but the complete results can be found in reference [22]. The diagonal elements hold the dominant fractions which proves that the separation is working and most decays will be classified correctly. It is clear that the classification becomes more difficult with the rising number of π^0's and a smaller percentage is labeled correctly. For the two and three π^0 decays, the migration is bigger towards the channels with less π^0's which shows that some π^0's are lost in the analysis. For the rho channel the migration is mainly towards the $h\,2\pi^0\nu$ channel.

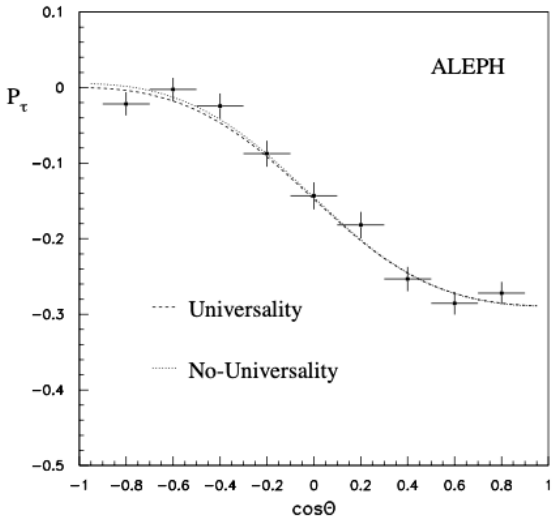

Figure 3.6: The total polarisation of the τ's in the process $e^+e^- \to Z \to \tau^+\tau^-$ measured by the ALEPH experiment [20]

The purity of the channel selection is illustrated in Figure 3.5, which shows the mass distribution of two photons in four photon events where one π^0 has already been identified. It shows a clear peak at the π^0 mass which will only appear if the true photons are correctly reconstructed and combined with their right partner. As there are six possible pairs of these four photons, this plot shows a high quality in the τ decay mode identification and π^0 reconstruction.

The total polarisation can now be measured. It is obtained by a fit of the experimental data to a combination of the left- and right-handed contributions from Figure 3.4. The result of the total polarisation of the τ's can be seen in Figure 3.6. Since the mean of this distribution provides the $\mathcal{A}_\tau$ parameter and the amplitude the $\mathcal{A}_e$ parameter, the two values can be compared and constitute a valuable tool to investigate the $e - \tau$ universality that the SM assumes. Their obtained values are

$$\mathcal{A}_\tau = 0.1451 \pm 0.0059 \tag{3.6}$$

$$\mathcal{A}_e = 0.1504 \pm 0.0068. \tag{3.7}$$

These values are consistent within the uncertainties and suggests a $e - \tau$ universality. From these measurements and the universality assumption, it is also possible to determine the weak mixing angle by

$$\frac{c_V}{c_A} = 1 - 4\sin^2\theta_{\mathrm{W}}. \tag{3.8}$$

The value of this central parameter in the electro-weak model is found to be

$$\sin^2 \theta_{\mathrm{W}}^{\mathrm{eff}} = 0.23130 \pm 0.00048. \tag{3.9}$$

3.1.1 Future studies

To further test the $e - \tau$ universality in future experiments, the uncertainties of the ALEPH measurements should be reduced. In order to do so, especially three things are important:

1. A clean and well-understood separation of the tau final states. This includes a precise π^0 counting method.

2. A good γ/π^0 separation

3. The ability to measure the energy of the $\pi^{\pm}$ and the π^0 separately in hadronic decays with $n_{\pi^0} > 0$

Having an accurate inter-channel separation for the τ decays will improve for example the τ branching fraction measurements and enable precision studies of the lepton in general. For the polarisation study, it is important as mixing the channels will disturb the kinematic fits and thereby the measured polarisation. Table 3.3 shows the relative weight the decay channels have for the τ polarisation measurements. It is clear that polarisation measurements mostly depend on having a clean separation of the hadronic channels, especially the hadron and rho channels. These are unfortunately also the most difficult to distinguish a as they mainly differ by the number of π^0's. This leads to the need for a precise π^0 counting scheme. In an experiment, there is a possibility that not all π^0's will be observed, for example if have a low energy. Conversely, the presence of e.g. radiation photons or the inevitable noise (which can be confused with photons) can lead to reconstructing extra fake π^0's. These two feed-down and feed-up mechanisms need to be addressed. The latter effect can be suppressed by having a good γ and π^0 separation. The γ/π^0 separation was one of the dominant factors for the uncertainties in the ALEPH results. Figure 3.7a shows the obtained precisions of the six decay channels and it can be seen that the two most precise channels, according to the systematic uncertainty, is the hadron and rho channels. The statistical uncertainty is not as interesting as

Channel	$\mathcal{A}_\tau$ (%)	$\mathcal{A}_e$ (%)
hadron	$15.21 \pm 0.98 \pm 0.49$	$15.28 \pm 1.30 \pm 0.12$
rho	$13.79 \pm 0.84 \pm 0.38$	$14.66 \pm 1.12 \pm 0.09$
a1(3h)	$14.77 \pm 1.60 \pm 1.00$	$13.58 \pm 2.11 \pm 0.40$
a1(h2π^0)	$16.34 \pm 2.06 \pm 1.52$	$15.62 \pm 2.72 \pm 0.47$
electron	$13.64 \pm 2.33 \pm 0.96$	$14.09 \pm 3.17 \pm 0.91$
muon	$13.64 \pm 2.09 \pm 0.93$	$11.77 \pm 2.77 \pm 0.25$
pion inclusive	$14.93 \pm 0.83 \pm 0.87$	$14.91 \pm 1.11 \pm 0.17$
Combined	$14.44 \pm 0.55 \pm 0.27$	$14.58 \pm 0.73 \pm 0.10$

(a) Measurements of the $\mathcal{A}_e$ and $\mathcal{A}_\tau$ parameters. The first error is the statistical error and the second the systematic error

	A_τ						
Source	h	ρ	$3h$	$h2\pi^0$	e	μ	Incl. h
selection	-	0.01	-	-	0.14	0.02	0.08
tracking	0.06	-	0.22	-	-	0.10	-
ECAL scale	0.15	0.11	0.21	1.10	0.47	-	-
PID	0.15	0.06	0.04	0.01	0.07	0.07	0.18
misid.	0.05	-	-	-	0.08	0.03	0.05
photon	0.22	0.24	0.37	0.22	-	-	-
non-τ back.	0.19	0.08	0.05	0.18	0.54	0.67	0.15
τ BR	0.09	0.04	0.10	0.26	0.03	0.03	0.78
modelling	-	-	0.70	0.70	-	-	0.09
MC stat	0.30	0.26	0.49	0.63	0.61	0.63	0.26
TOTAL	0.49	0.38	1.00	1.52	0.96	0.93	0.87

(b) Contributions to the systematic uncertainties (%) of $\mathcal{A}_\tau$ measurement for the different decay modes

Figure 3.7: The results and uncertainties for the $\mathcal{A}_e$ and $\mathcal{A}_\tau$ parameters obtained by the ALEPH experiment [20]

Decay modes	Sensitivity S	Branching fraction BR	Relative Weight $\propto S^2BR$
$e^- \bar{\nu}_e \nu_\tau$	0.22	0.18	0.06
$\mu^- \bar{\nu}_\mu \nu_\tau$	0.22	0.18	0.06
$\pi \nu_\tau$	0.58	0.12	0.30
$\rho \nu_\tau$	0.49	0.25	0.44
3 prongs	0.45	0.09	0.13

Table 3.3: The sensitivity, branching fraction and relative weight wrt. τ polarisation measurements for different τ decay channels. The relative weight is normalised to 1 [19]

this is mainly due to limited number of collisions at LEP. Figure 3.7b shows all the separate contributions to the systematic uncertainty and demonstrates that the most dominant contribution for the interesting rho and hadron channels (expect for the unexciting Monte Carlo statistics contribution) is the γ/π^0 separation. An improved γ identification would therefore be one way to improve the overall precision of the measurements. If a photon is accepted as a π^0 or vice versa, the decay will most likely be mis-classified and thereby worsen the precision the final polarisation measurements.

The last point on list concerns the ability to measure the energy of the $\pi^\pm$ and π^0 separately. This is important in order to obtain the x or ω variable. For the hadron channel this straight-forward calculation of x only demands a measurement of the $\pi^\pm$ energy, which can be determined by the tracking devise in a detector. For the rho and remaining hadronic channels this is more complicated as they also contain the decaying π^0. Eq. 3.5 shows that it is necessary to not only measure the total energy of the system, but to also measure the energies of the π^0's and $\pi^\pm$ separately.

3.1.2 Initial τ decay studies and detector requirements

The understanding of the measurements and separations needed for future τ polarisation measurements can now be used to infer a list of experimental requirements. Such requirements can be set by investigating the kinematics of τ decays. The kinematics are investigated using a simulation of the $\tau \to \rho\nu$ decay. Figure 3.8 shows some of the central variables based on the 4-vector information from the simulation.
The momentum of the ρ meson is shown in Figure 3.8a. It shows an almost uniform

distribution for $p > 10$ GeV with an average ρ energy of $E_\rho \sim 25$ GeV. Figure 3.8b shows the invariant mass of the charged and neutral pions. A clear peak at the ρ mass $m_\rho = 775$ MeV can be seen.
The momentum of the charged pion and the π^0 daughter photons can be seen in Figure 3.8c and3.8d. They show that the $\pi^\pm$ and π^0 momentum distributions are equivalent. Furthermore, it demonstrates that many photons appear at very low energies. Reconstructing all photons, and in extension all π^0's, is vital for a successful decay mode identification. Providing an experimental sensitivity to these low energy photons is therefore key. This means reducing noice and having a high energy resolution.

Figure 3.8e shows the opening angle between the two photons. This angle is energy dependent in the following way:

$$m^2_{\gamma,\gamma} = 2E_1E_2(1 - \cos\,\alpha(\gamma,\gamma)) \; . \tag{3.10}$$

The mass $m_{\gamma,\gamma}$ is the invariant mass of photon-photon system, E_1 and E_2 are the photon energies and $\alpha(\gamma,\gamma)$ is the opening angle between the photons [23]. The expression is only valid for two mass-less particles. To illustrate the angular dependence, it is helpful to examine the special case where $E_1 = E_2$. As the opening angle is generally small the expression simplifies to

$$\alpha(\gamma,\gamma) = \frac{m_{\gamma,\gamma}}{E_\gamma}, \tag{3.11}$$

where E_γ is the photon energy. This means that at higher energies the particles will be geometrically closer. At an average π^0 energy of ~ 15 GeV (based on Figure 3.8d), which corresponds to $E_\gamma = 7.5$ GeV, the opening angle becomes $\alpha(\gamma,\gamma) = 0.018$ rad. This is comparable with the experimental measurement of the opening angle shown in Figure 3.8e. For the π^0's of the highest possible energy ($E_{\pi^0} = 45.6$ GeV), this opening angle will be $\alpha(\gamma,\gamma) = 0.006$ rad which corresponds to 1.2 cm at a radius of 2 m. Being able to spatially separate such two photons in an experiment demands a high granularity of the detector. If the granularity is insufficient, the photon signals will merge into one and the π^0 might be mistaken for a single photon. This will disrupt the π^0 counting.

Figure 3.8f shows the angle between the charged pion and the photons. It can be seen that the distributions peak at ~ 0.05 rad which gives a spatial separation of 1.0 cm at a radius of 2 m.

The kinematics of the τ decay show that the detector requirements a future experiment can be summarised as:

1. A need for sensitivity to low energy photons in order to detect all π^0's.

2. A minimization of the noise levels to enhance precision in the π^0 counting.

3. A high granularity to spatially separate the π^0 daughter photons.

There are different options for such new experiments, but for scientists at CERN the FCC-ee experiment is the highest preference. However, before studying the specific experiment, it is important to understand how particles are detected in collider experiments. This demands an explanation of how particles interact with matter.

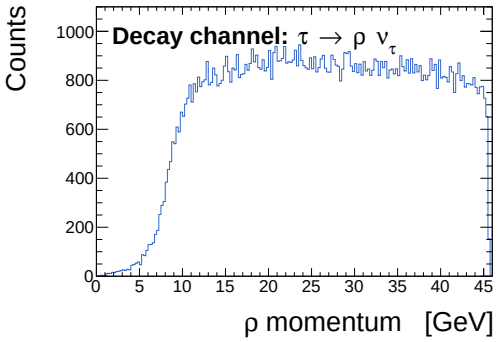

(a) Momentum of the ρ meson

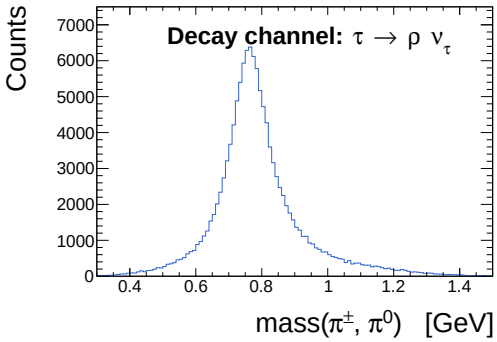

(b) Invariant mass of the $\pi^{\pm}$ and π^0

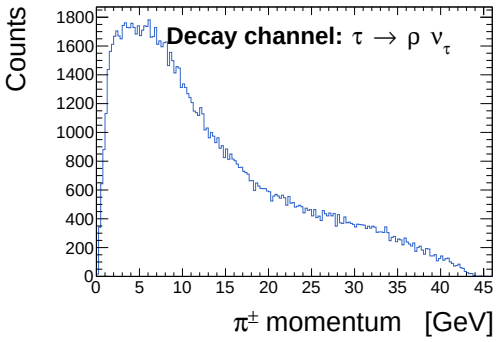

(c) Momentum of the charged pion

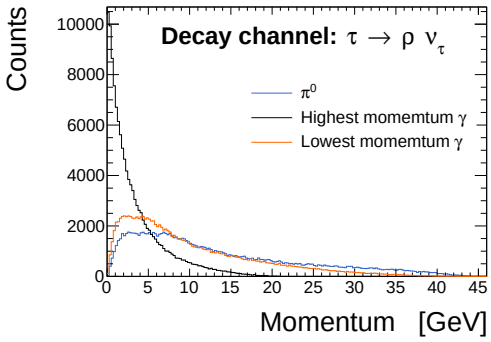

(d) Momentum of the π^0 and its two daughter photons

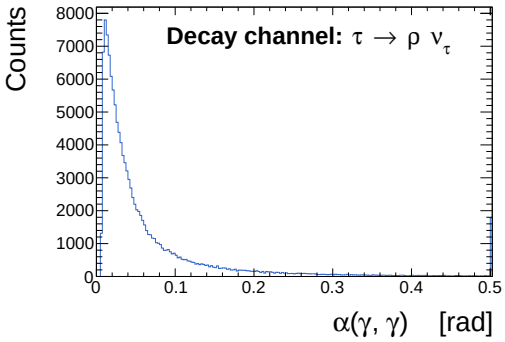

(e) Opening angle between the photons from the $\pi^0 \to \gamma\gamma$ process

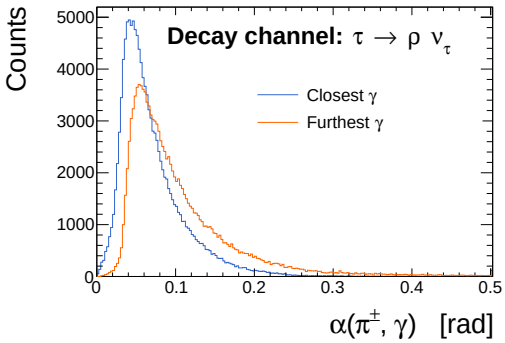

(f) Smallest and largest opening angle between the π^0 daughter photons and the $\pi^{\pm}$

Figure 3.8: Variables describing the kinematics of a $\tau \to \rho\nu_\tau$ decay. All plots are based on the 4-vector information

4 Interactions of particles and matter

As a particle traverses a detector it will interact with the material it penetrates. It is these interactions a detector records and exploits for later reconstructions of the particle. The type of interaction depends on the identity of the particle and can be sub-categorized in three classes: the interactions of charged particles, interactions of photons and electrons and interactions of hadrons [9].

4.1 Interactions of charged particles

Relativistic charged particles mainly interact electromagnetically. They ionize the atoms in the detector material which causes an energy loos for the charged particle itself. The magnitude of the ionisation energy loss mainly depends on the energy of the charged particle and on the density of the material it traverse. This dependence is shown in Figure 4.1, where ρ is the material density, dE/dx is the energy loss per unit length, $\beta = v/c$ and γ is the Lorentz factor given by $\gamma = 1/\sqrt{1 - v^2/c^2}$.

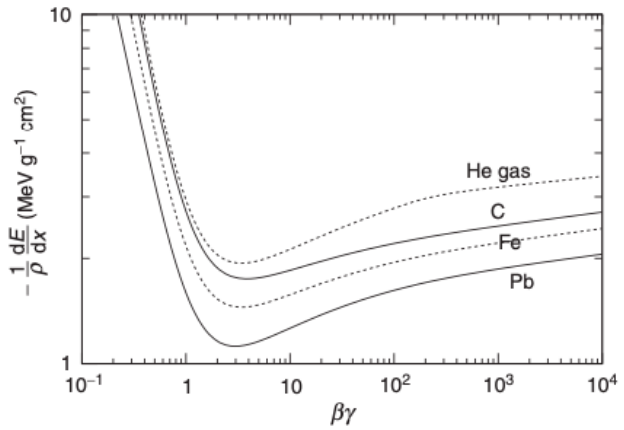

Figure 4.1: Energy loss due to ionisation for a single charged particle passing through different materials [9]

The figure shows the same behaviour for the materials and it can be seen that the energy loss for each material varies with approximately a factor 2. It is also clear that

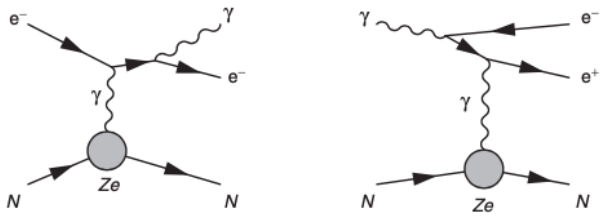

Figure 4.2: Left: the bremsstrahlung process. Right: the e^+e^- pair production. N is the nucleus and has charge $+Ze$ [9]

the energy loss is greatest at lower energies. For relativistic energies the dependence becomes almost logarithmic. This increasing energy loss is called "the relativistic rise". Some particles, such as cosmic-ray muons, will an energy loss close to the minimum of this curve, which is $\beta\gamma \approx 3$. They are therefore labeled as Minimum-Ionizing Particles (MIPs). This definition is however often expanded to include all particles that only looses energy due to ionisation. The latter definition is used in this thesis. An example of such particles are muons.

4.2 Interactions of photons and electrons

The second kind of interactions are the interactions of photons and electrons. The energy loss for low energy electrons is also mostly caused by ionisation, but when they exceed a critical energy (E_c), the energy loss becomes dominated by bremsstrahlung instead. Bremsstrahlung is the process where a charged particle is accelerated by the electric field of the atomic nuclei and therefore emits a photon. It is illustrated in Figure 4.2. The energy loss due to bremsstrahlung is linearly dependent on the energy of the particle and can occur for all charged particles. The probability of such an interaction occurring is inversely proportional to the squared mass of the particle. As for example muons are heavy, their energy loss is dominated by ionisation, whereas the lighter electrons are disposed to this process.

Since photons are neutral objects, they do not undergo bremsstrahlung, but they still interact electromagnetically. At low energies their energy loss is mainly due to photoelectric interactions. In these interactions, the photon will be absorbed by an atomic electron which causes an emission of the electron. At higher energies, the majority of the energy loss is instead due to e^+e^- pair production. Pair production in general, is the process where a neutral boson creates a particle and its anti-particle. For the photon, this can happen when it is subjected to the field of a nucleus. It is

illustrated in Figure 4.2. For this process to occur, the photon energy must be above the total rest mass energy of the e^+e^- pair and low energy photons do therefore not undergo this process.

For particle physics experiments, the high energy interactions are the most important. A central parameter for these electromagnetic interactions is the radiation length, X_0. It defines the average distance travelled by an electron when its energy is reduced by a factor $1/e$ due to bremsstrahlung. For a photon, the radiation length corresponds to approximately 7/9 of the mean free path of pair production. The radiation length varies with the atomic number of the material the photon/electron penetrates. Materials with higher atomic numbers will in general have shorter radiation lengths.

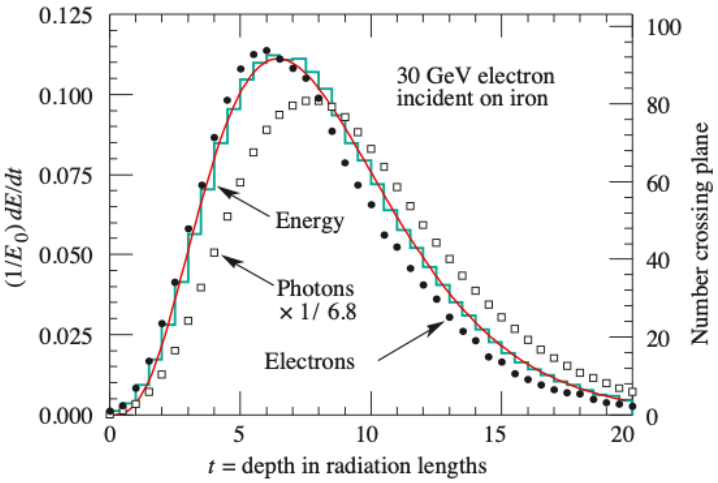

Figure 4.3: A simulation of the mean longitudinal profile of an electromagnetic shower produced by a 30 GeV electron in iron. The histogram shows the longitudinal profile per radiation length with a gamma-function fit (the curve). The circles (squares) shows the number of electrons (photons) with $E > 1.5$ MeV ($E \geq 1.5$MeV) crossing planes with a distance of $X_0/2$. They are measured by the scale on the right [24]

The interactions of an electron or photon will usually create an electromagnetic shower. When an electron undergo bremsstrahlung and radiates an photon, this photon will then undergo pair production creating an e^+e^- pair. The pair production electrons can then radiate a new bremsstrahlung photon, continuing to create a cascade of secondary particles until the average particle energy falls below critical energy. Beyond this point the energy loss is mainly due to ionisation. The number of particles in such a shower approximately doubles for every radiation length the

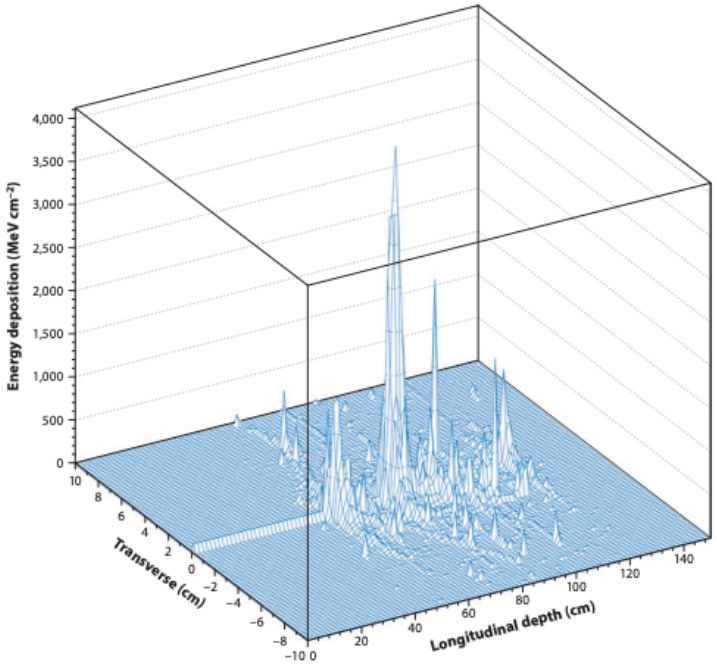

Figure 4.4: An example of a hadronic shower in Pb from a 100 GeV pion [25]. The particle enters from the left and leaves a MIP signal before creating a hadronic shower

shower penetrates. The energy deposition of the shower is described by the mean longitudinal energy profile. This is parameterized by:

$$\frac{dE}{dt} = E_0 b \frac{(bt)^{a-1} e^{-bt}}{\Gamma(a)}, \tag{4.1}$$

where t is the depth in radiation lengths and a, b are constants and E_0 is the initial energy of the particle [24]. An illustration of this gamma function can be seen in Figure 4.3. It shows a rapid increase in deposited energy followed by a slower decent as particles fall below the critical energy.

A useful quantity to describe the transverse development of an EM shower is the Molière radius. It is defined a the radius of a cylinder that, on average, contains 90% of the detected shower energy. It scales linearly with the radiation length of the detector material and is therefore useful when developing detectors as a smaller Molière radius means narrower showers and thereby better particle separation and position resolution.

4.3 Interactions of hadrons

The remaining form of interactions is the interactions of hadrons. Hadrons also loose energy due to ionisation but unlike the previously discussed particles, they can also interact with the atomic nuclei through the strong force. These interactions creates cascades of secondary hadrons which will subsequently interact. Additionally, if any π^0's are produced, their two daugther photons ($\pi^0 \rightarrow \gamma\gamma$), will create electromagnetic showers within the hadronic shower. A hadronic shower becomes vastly complicated and irregular compared to an electromagnetic shower.

For hadronic showers, the nuclear interaction length (λ_n) describes the average distance travelled by a hadron between interacting hadronically with the material it traverses, and can therefore be used to characterise the scale of the shower. There is also a pion interaction length (λ_π) , which describes the same distance specifically for pions. Even though a hadron on average travels one interaction length before starting a hadronic shower, it does not mean that no interactions occur before this point. Hadrons will still loose energy due to ionisation and these interactions will usually appear as a MIP-like signal. Figure 4.4 shows an example of a hadron traversing lead and creating a hadronic shower. The initial particle enters from the left and interacts hadronically after penetrating approximately 1/3 of the lead. Until this point a MIP signal appear. Afterwards, the hadron showers, creating irregular energy depositions as a result of the numerous hadronic and electromagnetic interactions. Some of the energy depositions are even spontaneous energy depositions around the interactions. These are called satellites [9] [25].

4.4 Detection of particles

In order to detect all the different types of interactions, a particle detector will need to consist of many specialized sub-detectors. When detecting a charged particle, the trail of ionised atoms it leaves behind can be exploited to reconstruct the particles' trajectory and momentum. This measurement is obtained in the tracking detector, of which there are two main types. The first is gaseous tracking detectors. These are large volumes of gas with a strong electric field. When the gas is ionised by the charged particle, the electrons will drift to an anode where the electric field provokes the electrons to create an avalanche of secondary ionisation. This creates an amplification of the original signal, which can then be detected. Because the ejected

atomic electrons have to drift to the anode before being detected, it creates a time lag between the original ionisation and the detection of the avalanche. This time lag can be determined if the electron drift velocity of the devise is known. The obtained time lag can be used to reconstruct the position of the passing charged particle to a high precision and thereby increase the position measurement accuracy. A chamber with known drift time information is called a drift chamber.

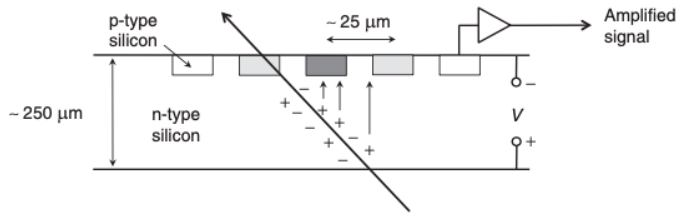

Figure 4.5: A illustration of charged particle passing through a silicon tracker, creating electron-hole pairs which will drift in opposite directions [9]

The other main tracking detector technique is silicon tracking detectors. They use semiconductors and consist of silicon pixels or strips. The silicon is doped to increase conductivity which induces the charged particle to create electron-hole pairs when traversing the detector. A potential difference is applied across the silicon and will force all holes to drift in the same direction where they are collected in a p-n junction. This is shown in Figure 4.5. A silicon tracker consists of several silicon layers in which a traversing particle will leave a hit. This tail of hits is then used for track reconstruction of the particle. The entire tracker is placed in a large solenoid which provides a uniform magnetic field in the direction of the beam axis (z-axis). Since a charge particle will move in a helix trajectory in a magnetic field, it is possible to parameterize its path. This parametrisation along with the known magnetic flux density of the applied field can be used to reconstruct the momentum of the particle. These silicon tracking detectors are becoming an increasingly popular for new experiments [9].

Electrons and photons are detected in the electromagnetic calorimeter (ECAL). There are two main types of ECALs: a homogeneous and a sampling ECAL. In the homogeneous calorimeter, the entire volume is sensitive and contributes to reconstructing the signal. The sampling calorimeter is constructed of sandwich-layers of active and absorber materials. The absorber material is usually a high-Z material, such as lead, to provoke the traversing particle to shower. The active material detects the EM showers and can be constructed in many different ways for example using plastic scintillators or noble liquid ionisation chambers. An advantage of the sampling calorimeter is that the sandwich structure allows for optimizing the individual materials for one specific task. The dis-advantage is that some of the particle energy

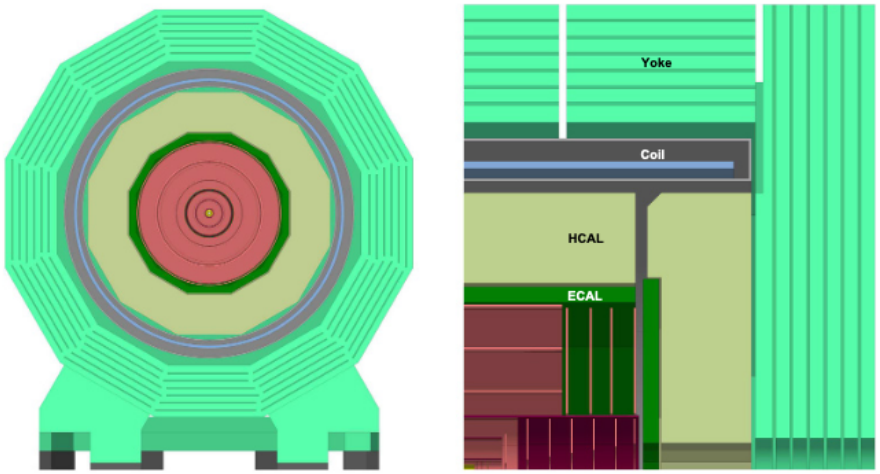

Figure 4.6: The CLD detector concept. Left: a cut-through view of the entire detector. Right: The sub-detector layers in the longitudinal direction. The center of the detector is the lower left corner [2]

will be deposited in the absorber layers and will thereby not be detected [26].
The ECAL is physically divided into read-out cells (in 3D). Each of these cells will register the energy deposited in the active material and provide a signal. The signals can then be combined to determine the total energy deposistion in the ECAL. The calorimeter is often also divided into segments in the longitudinal direction. The cells are assembled in towers from the interaction point to the outer radius of the detector. These cells and cell towers can be used to determine both the longitudinal and transverse energy dispersion. Since charged particles will also leave an ionisation tail in the ECAL, they will also be detected here and some hadrons might even shower in this calorimeter.

Hadrons are also detected in the hadron calorimeter (HCAL). Much like the ECAL, there are different design options for the HCAL, but one of them is also a sampling type, consisting of absorber and active materials. However, because the nuclear interaction length is usually significantly larger than the radiation length, it takes a longer distance before the hadrons have deposited all their energy. Some hadrons might even penetrate the entire ECAL without interacting, leaving only a MIP signal here. For this reason, HCALs are usually much thicker than the ECAL [26].

All of these sub-detectors are stacked in layers around a collision point and their combined measurements allows for reconstruction of the total event. An example of a complete particle detector is the CLD detector concept [2]. This detector is one of the proposed detector concepts for the FCC-ee experiment - a future experiment at CERN. An overview of the detector can be seen in Figure 4.6. The tracking system

consists of a silicon pixel vertex detector and a silicon tracker. Surrounding this inner part is a high granularity sampling ECAL with active layers of silicon and absorber layers of tungsten. Then follows a scinillator-steel HCAL. Surrounding these calorimeters is a superconducting solenoid applying a 2T magnetic field and a steel yoke which will also include muon chambers. Muon chambers are usually applied as an outer layer of detectors as muons are highly penetrating due to their MIP behaviour.

The Future Circular Colliders

5

The Future Circular Collider (FCC) integrated programme is the highest priority post-LHC accelerator at CERN. Its impressive tunnel will have a circumference of 97.756 km and will host two colliders during different stages. The first stage will be an ultimate luminosity electron-position collider (FCC-ee) and will cover the interesting energy range from the Z peak to the $t\bar{t}$ production threshold. This includes the Higgs production threshold which is a high priority of the experiment.
The second stage is an extreme energy proton-proton (FCC-hh) collider. It will reach energies as high as $\sqrt{s} = 100$ TeV which is unseen to the present day [1].

The physics opportunities for these colliders is enormous and extremely exciting. For studying τ physics, the FCC-ee is of the highest interest. With the FCC-ee being the earliest stage of the FCC, it is important to start considering, testing and optimizing its design.

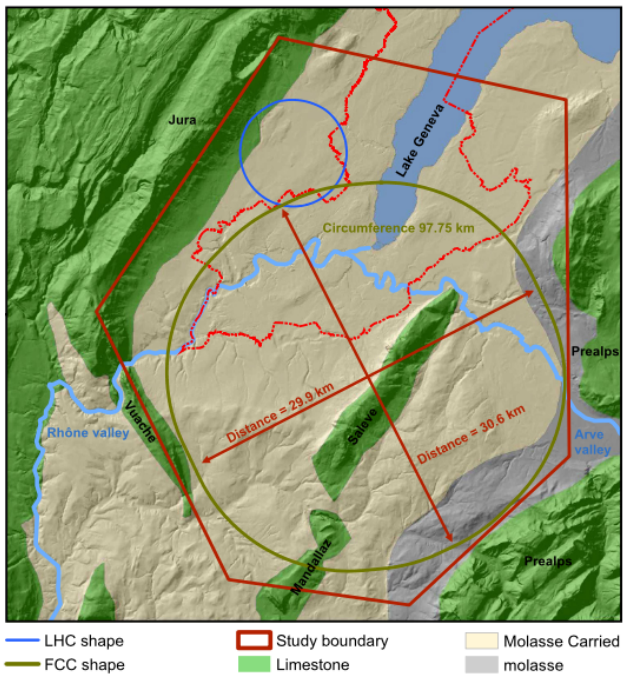

Figure 5.1: The placement of the FCC-ee ring compared with the current LHC ring [2]

5.1 Collider design

The placement of the FCC ring compared to the LHC and the geological boundaries in the surrounding area can be seen in Figure 5.1. The geological boundaries determines the study boundaries for the optimization of the placement.
The FCC-ee will be a quasi-circular double-ring collider. The tunnel will consist of straight and curved sections and if it is build, it will be one of the longest tunnels in the world exceeding the LHC in size by a factor ~ 4. There will be at least two interaction points (IPs) evenly spaced along the ring. Here, particles with a center-of-mass energies from 88 GeV to 365 GeV will be collided at a horizontal crossing angle of 30 mrad. The IPs are placed on straight sections of the tunnel to minimize the synchrotron radiation interfering with data from the collisions [2].

One of the goals of the FCC-ee design is achieving ultimate luminosities. This is, among other things, achieved by the top-up injection scheme which continuously re-fills the tubes with bunches using a booster synchrotron. Without this system the integrated luminosity would be more than an order of magnitude lower. An overview of the impressive luminosities as a function of the center-of-mass energies for FCC-ee can be seen in figure 5.2. The Z factory alone is expected to produce 5×10^{12} Z bosons which is 10^5 times the statistics from LEP. The expected number of $Z \to \tau^+\tau^-$ decays is 1.7×10^{11}, again providing enormous statistics and suggesting a reduction of statistical uncertainties of up to 300 times the uncertainties of former LEP measurements.
The extreme luminosities are also made possible by the double-ring structure as it eliminates parasitic collisions when storing large numbers of bunches. At the Z peak 16640 bunches will be stored with an average spacing of 19.6 ns and a bunch population of 1.7×10^{11}. At the Z peak the energy loss due to synchroton radiation is 0.036 GeV pr turn. The FCC-ee is also expected to produce 10^8 W pairs, 10^6 Higgs bosons and 10^6 $t\bar{t}$ pairs. From these numbers it is clear that unprecedented precision studies of the W, Z, Higgs boson and top quark are also possible [2].

Figure 5.2 also shows a comparison of the FCC-ee luminosity to the luminosities of three other potential future e^+e^- experiments [1]. The International Linear Collider (ILC) is a Higgs factory operating at $\sqrt{s} = 200 - 500$ GeV. The Compact Linear Collider (CLIC) will run at threshold energies from 380 GeV to 3 TeV to study the Higgs boson and the top quark. The Circular Electron Positron Collider (CEPC) is another circular collider planned to be built in China. It will run at energies

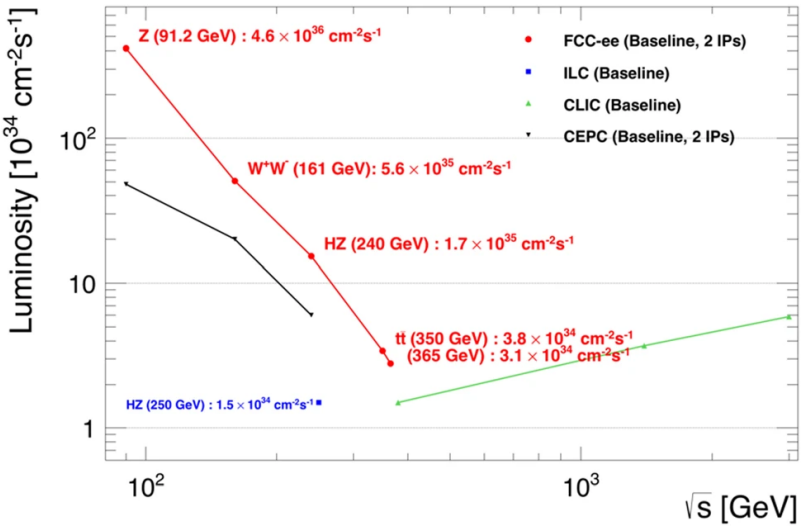

Figure 5.2: The expected luminosities for the center-of-mass energies ($\sqrt{s}$) planned for the FCC-ee collider. These luminosities are shown in comparison with other possible e^+e^- collider projects. [1]

between 90 GeV and 250 GeV and function as a Higgs, Z and W factory. It can be seen that the FCC-ee exceeds the linear colliders in luminosity at these relatively low energies (this would not hold for higher energies due to synchrotron radiation).

The design of the FCC-ee suggests impressive measurement potentials. Choosing to collide electrons and positions gives a clean experimental environment with little background and low radiation levels. Minimizing the background will make it easier to identify the interesting physics processes. Also the fact that the leptons are point-like will give a well defined initial state in terms of the particles' 4-vectors and polarisation. Constructing a circular collider instead of a linear one also ensures that the beam energy is explicitly known.

The construction of the ring is an ambitious project and the first collisions are scheduled to occur in the 2040s. Right now there are several on-going feasibility studies on many different aspects of the experiment. For τ polarisation measurements, especially performance studies of possible ECALs are of interest. One of the proposed ECALs is a liquid argon based design.

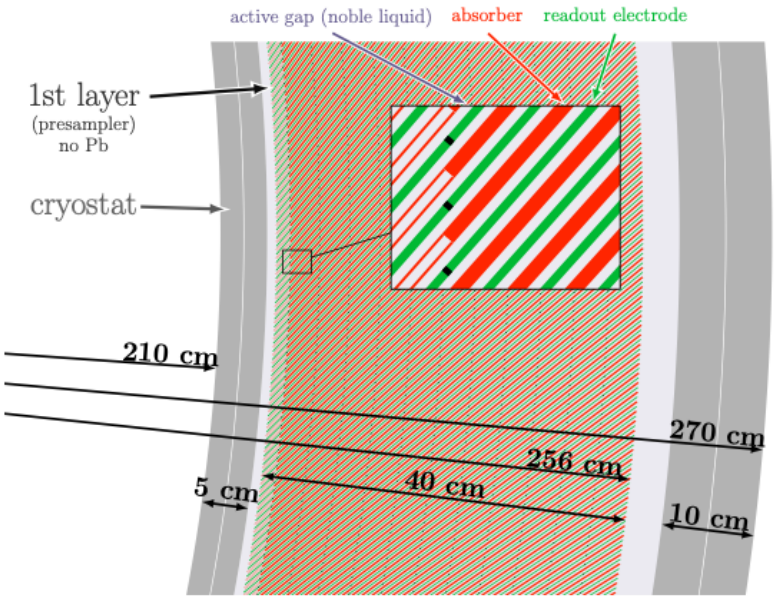

Figure 5.3: The design of barrel for the LAr ECAL proposed for the FCC-ee. The sampling calorimeter consists of layers of lead and steel (absorber) and LAr (active gap) that are tilted by a $\sim 50°$ angle wrt. the radial direction. In front of the calorimeter is a cryostat and a LAr pre-sampler [3]

5.2 A liquid argon electromagnetic calorimeter

A liqiud argon (LAr) electromagnetic calorimeter is currently installed in the ATLAS detector at the LHC and has proven to be highly stable and provide an high energy resolution, linearity and uniformity. It has therefore been proposed by the Noble Liquid Calorimetry working group at CERN to adapt this sampling calorimeter for the FCC-ee [3].

The proposed design can be seen in Figure 5.3. The central barrel of the proposed calorimeter is 40 cm deep which corresponds to $\sim$ 22 radiations lengths (X_0). It consists of 1536 sandwich layers composed by an absorber layer, a readout electrode and two active gaps. The absorber is a 2 mm thick lead layer with two 100 μm thick steel plates glued onto each side of the lead. It is followed by the first active LAr gap which varies from 1.2 mm at the inner radius to 2.4 mm at the outer radius. A layer of readout electrodes is placed before the second LAr gap which has a thickness identical to the first. In order to retrieve signals from the readout electrodes, all the sandwich layers are titled by $\sim 50°$ wrt. the radial direction. This construction also ensures a high sampling frequency of the ECAL without any acceptance gaps. The exact inclination is chosen to uphold a uniform signal in ϕ.

The sandwich layers are divided into 12 segments in the radial direction. The first of the segments is approximately half as thick as the following segments and does not contain lead in the absorber sections of the sandwich layers. This pre-sampler is included to facilitate a correction of the energy lost before particles reach the active ECAL layers. This is especially important for low energy particles.

Figure 5.4 shows the fine cell structure and the diamond shape cells formed from the titled layers. Here, the example cell is defined to include four sandwich layers expect for the pre-sampler which includes only two. A particle with a straight trajectory at $\theta = 90°$ will traverse ~ 50 sandwich layers before reaching the outer limit of the ECAL [27]. The cell sizes vary with the radius because the thickness of the LAr gaps are increasing. This induces the sampling fraction to be radial dependent as well. The behaviour is corrected by an energy calibration combined with a E/p calibration from the tracker.

All the sandwich layers are placed inside a cryostat and cooled to cryogenic temperatures which reduces thermal noise (as well as ensuring that the argon is liquefied). This has proven effective at the ATLAS experiment even for long cable connections. The careful design of the read-out electrodes also promote very low noise levels. They consists of multiple layer printed circuit boards (PCBs) and each calorimeter cell is expected to contain one to four electrodes in ϕ. The estimated noise per readout cell is 2-10 MeV. Since a minimum ionizing particle is expected to leave ~ 32 MeV per cell, it should be possible to detect these low energy signals with the current estimated noise levels. The exact number of sandwich layers per cell will be optimized by studies of the requirements for π^0 and particle-flow reconstructions [3].

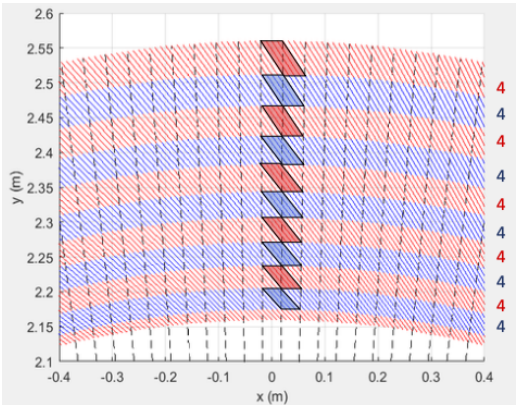

Figure 5.4: Example cells for a 11 layer calorimeter with each cell containing four sandwich layer, expect for the pre-sampler which contains two [28]

There are many other on-going optimization studies regarding the design of this ECAL. The main focus is to optimize it for better particle identification such as the π^0/γ separation. This study seeks to investigate the performance of the proposed

LAr design with respect to future τ polarisation measurements. A clean and well-understood separation of the hadronic τ decays is vital for polarisation measurements but in order to achieve it, a precise π^0 reconstruction is needed. This is instrumentally demanding as the decay products of the τ are close-by and requires a sensitivity to low energy photons. An examination of the best τ decay mode separation possible with the LAr ECAL is therefore a good benchmark for its performance.

6 Simulations

The results presented in this thesis are based on events generated in simulations. These simulations and the applied ECAL geometries are discussed in this chapter.

6.1 Generating event files

The event files are produced using Pythia [29] and the FCC software (FCCSW) [30]. There are two main type of events: Single particle gun (SPG) events and full τ events. The full τ event files contain the decay products of the τ's from $e^+e^- \rightarrow Z \rightarrow \tau^+\tau^-$ events at the Z peak ($\sqrt{s} = 91.2$ GeV). An overview of the generation of these events can be seen in Figure 6.1. The τ events are generated using Pythia. The τ's are not polarized in this simulation and they are forced to decay to a predetermined final state. The simulations are also conducted without applying any magnetic field. The 4-vectors of the generated particles are saved in Les Houches files and passed on to the Geant4 toolkit which is embedded in the FCCSW [31]. Geant4 and the FCCSW provides the detector simulation using a specified ECAL geometry. The output are so-called hit files which are ROOT files containing all the energy depositions (hits) of the event along with their coordinates. A ROOT macro then imports the hit files and establishes a cell structure. The cells are arranged in a fixed 3D grid and contains the collective hit energy deposited within them. The macro outputs a cell file in ROOT format which can then be used for clustering and further analysis. The hits and cell files are received as the starting point of this analysis.

For the full τ events, one of the τ's will decay through a fixed hadronic channel and this decay will be the interesting one for this analysis. The other τ lepton is forced

Figure 6.1: An overview of how the simulated events used for this analysis are generated

to decay through the $\tau \to \mu\nu_\tau\bar{\nu}_\mu$ channel and will be neglected. As the direction of the particle is arbitrary, the full τ events are produced at $\theta = \frac{\pi}{2}$.

The SPG events contain one single particle per event with a predetermined energy or energy range. These events are generated directly with Geant4 but otherwise goes through the same process as the full τ event simulation. For simplicity, all SPG events are generated along the x-axis of the detector with $\theta = \frac{\pi}{2}$ and $\phi = 0$. An overview of the central data files for the analysis along with their statistics can be seen in Table 6.1.

Single Particle Gun			**Full τ event**	
Particle	Energy	N events	Decay mode	N events
γ	0.5 GeV, 1 GeV	10k, 10k	$\tau \to \pi^\pm\nu$	20k
	5 GeV, 10 GeV	2k, 10k		
	20 GeV, 45.6 GeV	1k, 1k		
	0-45.6 GeV	20k		
π^0	5 GeV, 10 GeV	1k, 1k	$\tau \to \pi^\pm\pi^0\nu$	20k
	20 GeV, 45.6 GeV	1k, 1k		
	0-45.6 GeV	20k		
e^-	10 GeV, 20 GeV	10k, 10k	$\tau \to 2\pi^\pm\pi^0\nu$	20k
	0-45.6 GeV	20k		
π^+	10 GeV, 20 GeV	10k, 10k	$\tau \to 3\pi^\pm\pi^0\nu$	20k
	35 GeV, 0-45.6 GeV	10k, 20k		
π^-	35 GeV, 0-45.6 GeV	10k, 20k		
μ^-	10 GeV	10k		

Table 6.1: The event files (SPG and full τ events) used for this analysis. The particle species, energy and number of events is shown. The full τ events are produced in the $e^+e^- \to Z \to \tau^+\tau^-$ process where the electrons are collided at $\sqrt{s} = 91.2$ GeV.

It was unfortunately discovered late in the thesis process that the τ decays do not happen realistically. The initial and finial state particles are correct, but the intermediate ρ meson or a_1 particle is not produced. This means that for example the rho decay will be a direct decay from $\tau \to \pi^\pm\pi^0\nu_\tau$ giving a 3-body decay of the τ instead of a 2-body decay. The kinematics of the $\tau \to \pi^\pm\pi^0\nu$ decays used for this analysis is shown in Figure 6.2. The kinematics presented in Figure 3.8 are however from a later realistic τ decay simulation, and the two can be compared to investigate the difference. Figure 6.2a and 6.2b show that there is indeed no ρ meson produced in the events used for this analysis. The momentum distribution of the $\pi^\pm$ and π^0 (Figure 6.2c and 6.2d) are also slightly different than for the realistic decays (Figure 3.8c and 3.8d). Figure 6.2f shows that the opening angle between the photons and the

$\pi^{\pm}$ is enhanced, since it is a direct 3-body decay. However, the π^0 decays, which is one of the crucial aspects of this analysis, happen realistically. The distributions of the photon opening angle shown in Figure 6.2e and 3.8e are also consistent. The majority of the results presented in this analysis are therefore valid, but results concerning the full τ events should be treated with some caution.

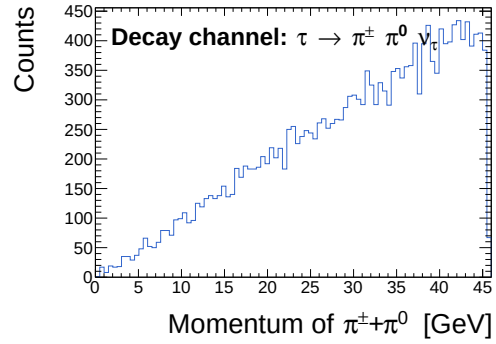

(a) Total momentum of the $\pi^{\pm}$ and π^0

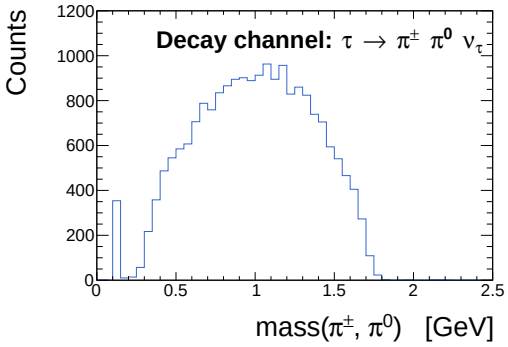

(b) Invariant mass of the $\pi^{\pm}$ and π^0

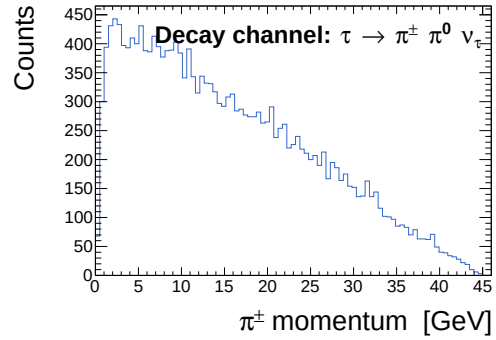

(c) Momentum of the charged pion

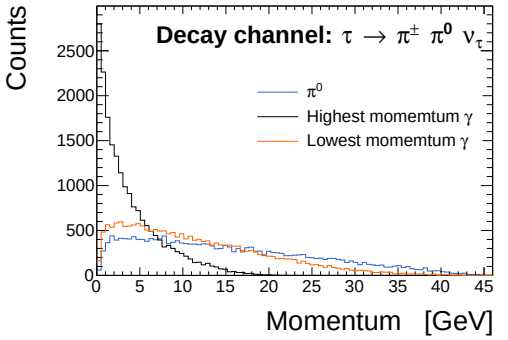

(d) Momentum of the π^0 and its two daughter photons

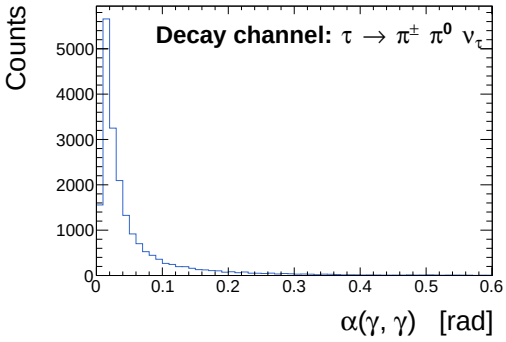

(e) Opening angle between the photons from the $\pi^0 \to \gamma\gamma$ process

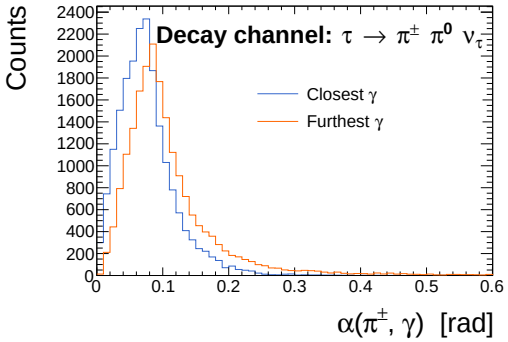

(f) Smallest and largest opening angle between the π^0 daughter photons and the $\pi^{\pm}$

Figure 6.2: Variables describing the kinematics of the (unrealistic) $\tau \to \pi^{\pm}\pi^0\nu_{\tau}$ decay. All plots are based on the 4-vector information.

6.2 Simulated geometries

The proposed LAr ECAL geometry is set up using the FCCSW. The simulation is based on an original FCC-hh simulation design made by J.Faltova and A.Zaborowska. To accommodate this generic framework for the LAr geometry, the radius (both inner and outer) was adjusted and a PCB layer was added to the sandwich layers. The virtual geometry is however not an exact replica of the proposed LAr geometry. A few simplifications is introduced since the proposed design is still being developed and so including all details is unnecessary. The focus of this simpler geometry is persevering the longitudinal and transverse granularity of the proposed ECAL and ensuring a correct material composition. One simplification is a substitution of the titled layers by concentric cylinders. This is because square cells are simpler for a first study. The analysis is still valid as the physics is not affected by the cell shape. Nevertheless, it does make the design unrealistic and impractical as retrieving signals from such a detector in real life would be impossible (this is of cause not an issue for simulations). The titled layers can be introduced at a later time without major changes in the analysis.

The sandwich layers of the proposed ECAL are simplified by merging the PCB and glue layer into one. An average material constant is used to ensure a realistic material composition. The placement of this mixed layer can be seen in Figure 6.3. The simulated sandwich layers are 5.7 mm thick and consists of 0.37 mm steal, 1.44 mm PCB/glue, 1.39 mm lead and 2.5 mm LAr. The overall geometry consists of 70 layers in total and is 40 cm deep.
A 50 mm cryostat made of aluminium and a 20 mm LAr pre-sampler are placed before the sandwich layers.

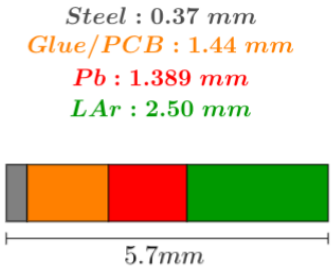

Figure 6.3: A sandwich layer of the simulated LAr geometry

The LAr ECAL design is not unique. For a noble liquid sampling calorimeter such as this, both the active and absorber layers can be exchanged and investigating other compositions is a natural part of design optimization. A liquid krypton (LKr) and tungsten (W) ECAL will therefore also be investigated in this thesis. This study is less comprehensive and some methods are simplified to make a fast comparison of the performances for the two noble liquid options. The LKr and W materials are interesting because they have smaller radiation lengths and Molière radii which

possibly lead to more compact showers. Having compressed showers might be advantageous for the separation of spatially close particles and could thereby enhance the π^0 reconstruction. The constituting materials of the both ECALs along with their interaction lengths, radiation lengths and Moliére radii, can be seen in Table 6.2. The total thickness of a sandwich layer in the LKr design is 3.7 mm instead of the former 5.7 mm for the LAr ECAL. As the LKr design still consists of 70 concentric cylinder layers, the LKr ECAL is 140 mm thinner than the LAr ECAL. The thickness of the tungsten and LKr layers are adjusted to match the depths of the LAr ECAL measured in radiation lengths. For the LKr ECAL the total depth is $21.3X_0$ whereas it is $20.6X_0$ for the LAr design.

Material	λ_n [mm]	λ_π [mm]	X_0 [mm]	Molière radius [mm]	Thickness LAr ECAL [mm]	Thickness LKr ECAL [mm]
LAr	857.7	1067	140.03	90.43	2.5	-
Pb	175.9	199.3	5.613	16.02	1.389	-
LKr	618.0	734.7	47.03	58.57	-	1.0
W	99.46	113.3	3.504	9.327	-	0.889
Steel	170.12	205	17.75	-	0.37	0.37
Glue+PCB	482.62	482.62	178.89	-	1.44	1.44

Table 6.2: Nuclear interaction length, pion interaction length, radiation length, Molière radius and thickness of the materials in the sandwich layers for both the LAr and LKr ECAL designs [32].

The total interaction length of the two ECALs can be computed using the information given in Table 6.2 and the expression:

$$\frac{1}{\lambda} = \sum \frac{w_j}{\lambda_j}, \tag{6.1}$$

summing over the different materials of the ECAL. λ_j is the interaction length and w_j is the thickness fraction of material j. The radiation length in a sandwich layer can be found in a analogues manner. The interaction and radiation lengths of the sandwich layer compositions can be seen in Table 6.3 and shows shorter lengths for all parameters for the LKr design.

6.2.1 A first comparison of the noble liquid designs

As a first comparison of the two calorimeters, the shower development in each calorimeter will be studied using the hit files. Figure 6.4 shows the longitudinal

ECAL	λ_n [mm]	λ_π [mm]	X_0 [mm]
LAr	356.75	404.12	19.44
LKr	235.14	264.08	12.18

Table 6.3: Interaction and radiation lengths of the LAr and LKr sandwich layers

profile of 10 GeV photons showering in each of the two ECALs. The profiles show the regular shapes of EM showers and compares nicely to the theoretical profile shown in Figure 4.3. The means of the distributions in Figure 6.4a and 6.4b show that photons shower slightly earlier in the LKr ECAL. The fact that both distributions end at ~ 0 GeV after the 70 sandwich layers demonstrates that even though the LKr ECAL is 140 mm thinner than the LAr ECAL, the shorter Molière radii of these materials ensures that almost all the initial energy of the particle is still deposited in the ECAL.

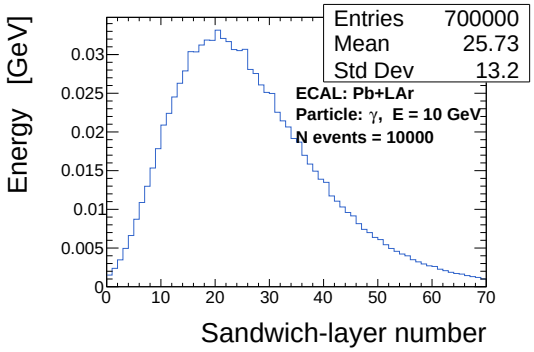

(a) The energy deposited per sandwich layer for the LAr ECAL

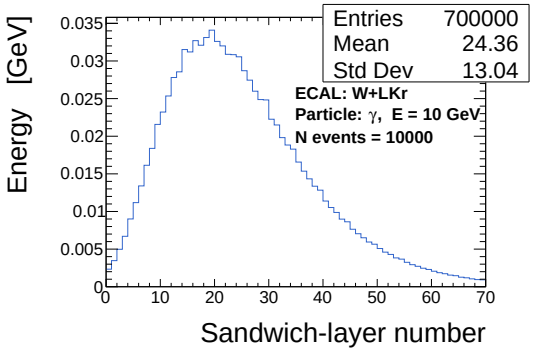

(b) The energy deposited per sandwich layer for the LKr ECAL

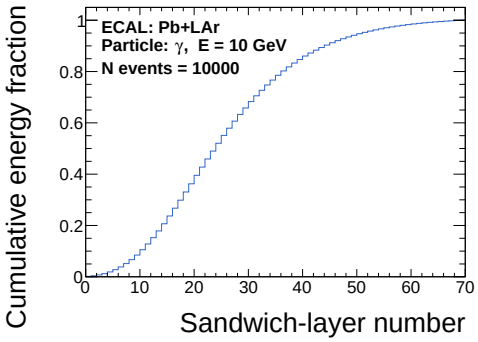

(c) The cumulative energy fraction deposited in each sandwich layer of the LAr ECAL

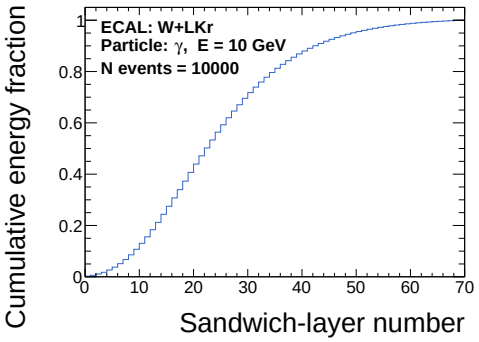

(d) The cumulative energy fraction deposited in each sandwich layer of the LKr ECAL

Figure 6.4: The longitudinal shower development in the LAr (left) and LKr (right) ECALs

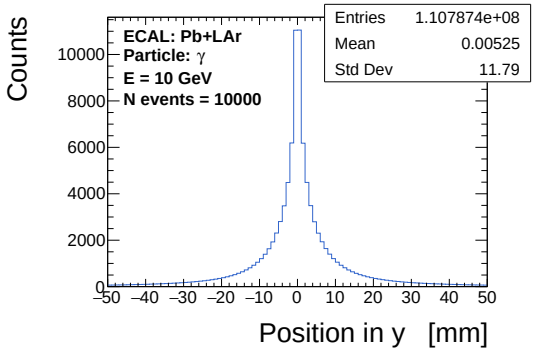

(a) The hit position along the y-direction for the LAr ECAL

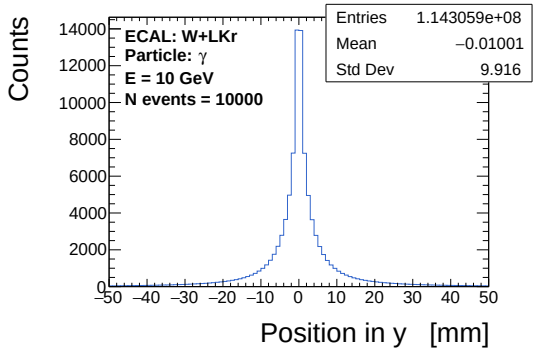

(b) The hit position along the y-direction for the LKr ECAL

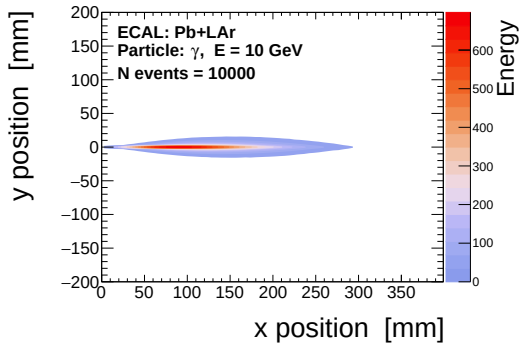

(c) The transverse dispersion of energy for the LAr ECAL

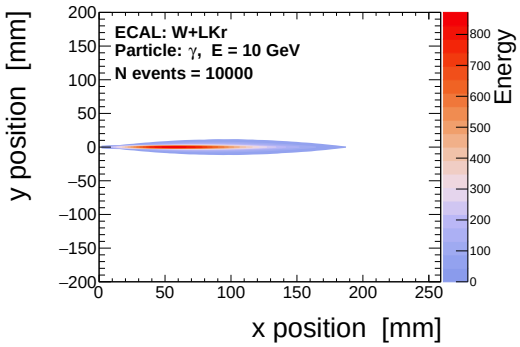

(d) The transverse dispersion of energy for the LKr ECAL

Figure 6.5: The transverse shower development in the LAr (left) and LKr (right) ECALs

The transverse profile is can be seen in Figure 6.5. As the events are produced along the x-axis, the y position is centered around zero and the x-position will imitate the previously discussed longitudinal profile. By comparing the standard deviations in both directions, it is clear that the showers are more compact in the LKr ECAL. This is also illustrated in the Figure 6.5c and 6.5d, which show the energy dispersion in the transverse plane. A comparison of the two figures show that the LKr showers are narrower.

Figure 6.6 shows the energy deposited in the ECAL as a function of the distance from the track line. When comparing the means of the distributions shown in Figure 6.6a and 6.6b, it is again clear that the particles deposit more energy at shorter distances for the LKr ECAL. This is explicitly shown in the integrated distributions from which the Molière radius can be directly extracted. The Molière radius is found at the 90% mark on the y-axis, which is indicated by a horizontal line. For the LAr ECAL the Molière radius is 41 mm whereas it is 27 mm for the LKr ECAL. This

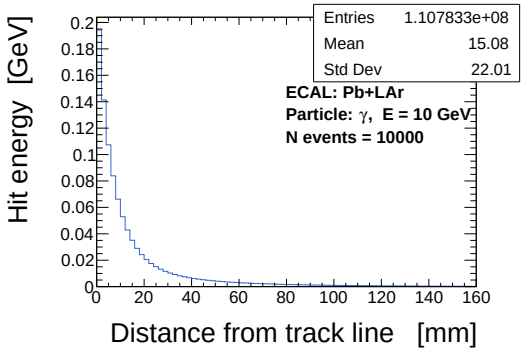

(a) The hit energy as a function of its distance to the track line for the LAr ECAL

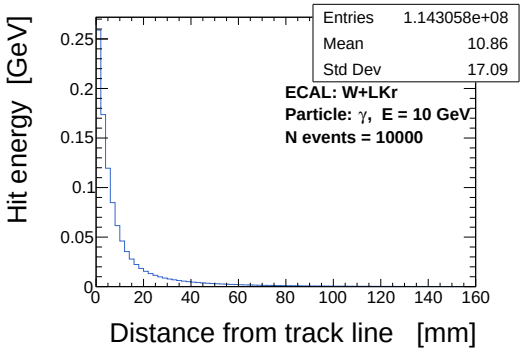

(b) The hit energy as a function of its distance to the track line for the LKr ECAL

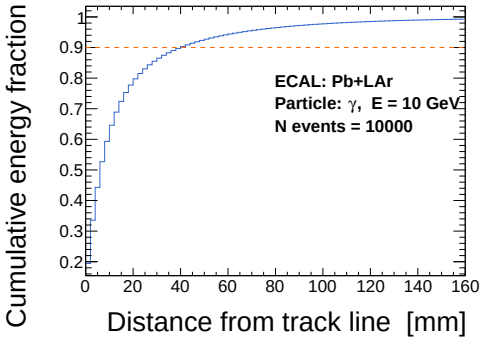

(c) The deposited energy fraction as a function of the distance from the track line for the LAr ECAL. The horizontal line indicates the Molière radius

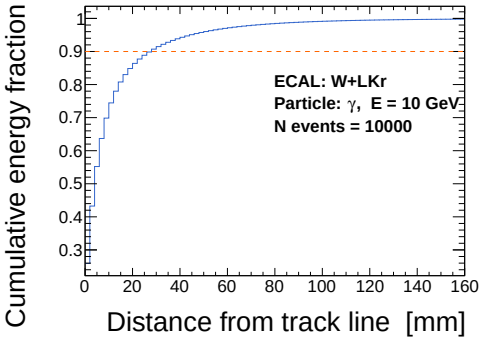

(d) The deposited energy fraction as a function of the distance from the track line for the LKr ECAL. The horizontal line indicates the Molière radius

Figure 6.6: The deposited energy as a function of the distance from the track line for both the LAr (left) and LKr (right) ECALs

supports the overall argument that a LKr ECAL will provide more compact showers. Investigating this option further therefore remains interesting.

6.3 Cell structures

There is no build-in cell structure in the simulated geometries. The cell structure is implemented subsequently and all hits from the particles are assigned a cell. The sandwich layers of the LAr calorimeter is divided in 680 cells in the $\phi-$direction, 300 cells in the $z-$direction, 10 cells in the radial direction, giving an approximate cell size of $2 \times 2 \times 4$ cm^3. Because all single particles are generated parallel to the x-axis, the events will have a bias towards the cell structure of the detector. To avid this, the position of the entire event is displaced randomly within the area of one cell. This smearing is shown in Figure 6.7.

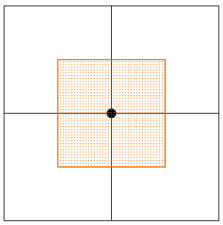

Figure 6.7: Smearing of event position (black dot) within the area of 1 cell (orange square)

The choice of not integrating the cell structure into the geometry allows for testing other cell sizes on the same simulations. To exploit the more compact showers of the LKr design the cell size is decreased to $1 \times 1 \times 2.6$ cm^3. The LKr design will thereby consist of 1360 cells in $\phi-$direction, 600 cells in the $z-$direction and 10 cells in the $r-$direction. The event smearing is also applied here.

In order to make an apples-to-apples comparison of the noble liquid detectors, a the revised LAr design with $1 \times 1 \times 4$ cm^3 cells is studied and compared to the $2 \times 2 \times 4$ cm^3 cell design (see section 10.1). The smaller cell size is interesting to investigate in general as it was shown in section 3.1.2 that the spacing of the photons from a 45 GeV π^0 is 1.2 cm at r = 2 m. Cells of 1×1 cm^2 in the transverse plane will therefore have a better chance of separating two photons. The main focus of this thesis is however on the proposed LAr $2 \times 2 \times 4$ cm^3 cell design and next three chapters will concern this detector.

6.4 Initial energy resolution

To account for the fact that only energy deposited in active layers is recorded, a calibration is implemented. It is observed that only $\sim 1/8$ of the energy is deposited in the active layers of the LAr detector and a linear calibration factor of $f_{cali} = 7.92$ is obtained. This corresponds to a sampling fraction of 12.6%. The total energy deposited after this calibration for 10 GeV photons can be seen in Figure 6.8. The distribution is nicely centered around the initial energy due to the successful calibration. The fit shows an energy resolution of $\frac{\sigma_E}{E} = \frac{7.75\%}{\sqrt{E}}$.

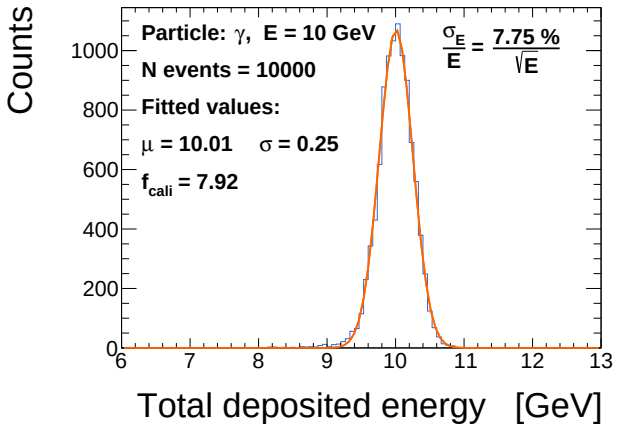

Figure 6.8: Total energy deposited by a 10 GeV photon in the LAr ECAL

7 Shower reconstruction

The simulation described in chapter 6 provide cell files containing the energy deposited in each cell along with the cell position. In order to reconstruct a particle shower, these cells need to be assembled into a 3D cluster which collects the total energy of the original particle. This re-assembly is performed by a specially developed clustering algorithm. The optimal algorithm will ensure that one cluster corresponds to exactly one particle. Real-life collisions can contain several particles with different energies and directions, which complicates separate reconstructions of all particles. The design of the clustering algorithm and its performance is discussed in this chapter.

7.1 Clustering algorithm

The clustering algorithm build for this analysis is inspired by the CLUstering of Energy (CLUE) method developed by the CMS collaboration [33]. The method used in this thesis is however implemented from scratch by Mogens Dam with several changes from the original CLUE algorithm. The optimization of the algorithm was performed by the author of this thesis. The method relies on three prerequisite variables: a zero-suppressed list of cells, i.e. a list of all cells with recorded energy depositions, and two adjustable energy thresholds, called the low and the high threshold. The thresholds define the energy limits for cells to be included in (low threshold) or start a new cluster (high threshold). For this study, the limits are $\text{thrs}_{low} = 10$ MeV and $\text{thrs}_{high} = 20$ MeV. The thresholds have been defined after consulting the Noble Liquid Calorimetry working group to ensure that the values are realistic and in agreement with the previously presented expected noise per cell.

The algorithm starts from the zero-suppressed list of cells by defining a list of 3D neighbours for each cell. For flexibility, the number of neighbours can be adjusted from 26 neighbours (a 3×3 box of cells) via 18 neighbours (suppressed corners of 3×3 box) to 6 neighbours (only cells with faces touching). Throughout this analysis, the 26 neighbour option is being used.

The neighbour list allows for identifications of a highest-neighbour for each individual cell. The highest-neighbour is the highest energy neighbouring cell exceeding both the low threshold and the energy of the cell itself. If no highest-neighbour is found, the cell is an energy maximum and will either be classified as a seed or an outlier. An outlier is an energy maximum cell without any neighbours that exceeds the low threshold and it will not be considered for clustering. A seed is an energy maximum cell that exceeds the high threshold and has at least one neighbour.
During this step each cell is additionally provided with a list of followers. The list contains all cells that point to this cell as their highest-neighbour.

Now the actual building of the clusters can occur. Starting at the seeds, cells are collected iteratively using the list of followers. Each seed will thereby create a proto-cluster.

The energy depositions within a shower can fluctuate and have multiple energy maxima leading to the creation of several clusters per shower. To avoid this, a last merging step is included in the clustering process. Here, the proto-clusters will be merged into larger final clusters if two clusters have neighbouring cells exceeding the low threshold additional to meeting one of two sub-requirements. More specifically, it is required that the opening angle between the seeds is $\alpha_{\text{seed 1,seed 2}} < 0.02$ rad or that at least one of the seeds is located in the last half (last five layers) of the ECAL. After the merging, all clusters are saved and ready for further analysis.

There are a few things to notice with this method. First of all, since there is no energy limit for cells to point a highest-neighbour, there will be one extra layer (in 3D) of cells at the edge of the clusters that are collected irrespective of their energy. This design choice ensures a more complete containment of the energy of the original particle as it is often deposited in a cloud without definite boarders.
Secondly, a reconstruction threshold of 200 MeV is enforced after the clustering. This means that all clusters with energies below this limit will be dismissed and not used in the subsequent analysis. It is extremely hard to determine if these very low energy clusters emerge from actual particles or not, and since it is rarely the case, they can be dismissed with a minimal the loss of signal.

The cluster-merging and its requirements demand a more detailed explanation. The merging process has been optimized with the goal of ensuring that each cluster corresponds to one particle. Without merging, one shower could be split up into several clusters, but without strict merging requirements too many clusters will be merged.

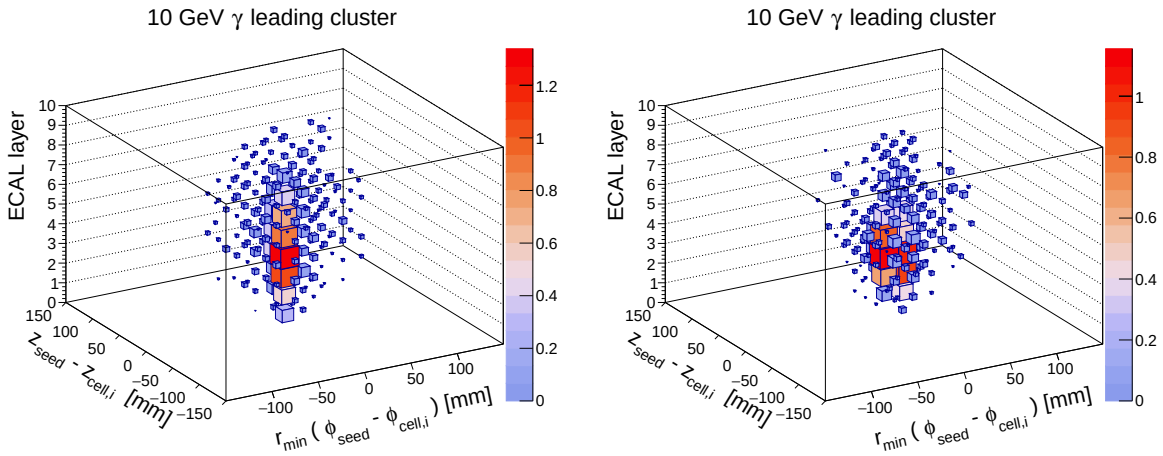

Figure 7.2: Two examples of clusters from 10 GeV photons. The color bar indicates the energy deposited in each cell measured in GeV

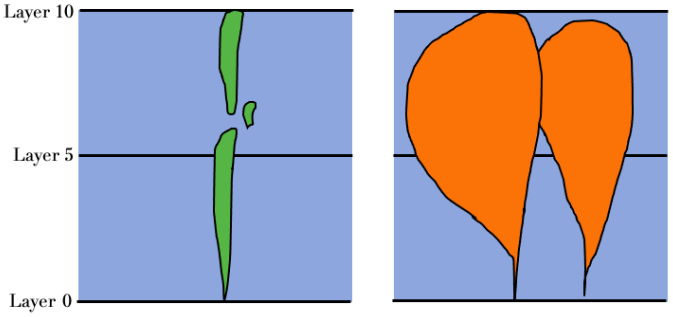

Figure 7.1: Illustration of showers in the ECAL. Left: An example muon shower. Right: An example π^0 consisting of two daughter photons

Two example events where merging is central are illustrated in Figure 7.1. The left figure illustrates a muon/MIP passing through the ECAL, whereas the right figure imitate a photon pair from a π^0. In order to reconstruct the muon properly the proto-clusters should be merged into one, but the two photons should still be reconstructed as two separate clusters. The design of the merging step tries to accommodate both situations. The angular requirement ($\alpha_{\text{seed 1,seed 2}} < 0.02$) ensures a proper reconstruction of the example muon shower by merging close-by proto-clusters to avoid splitting up the MIP signal. The layer requirement on the other hand exploits the fact that showers are narrower in the first ECAL layers and are therefore possible to separate here, even if they touch in the later layers. Demanding one of these requirements to be true before a merging occurs can thereby help increase the precision in the clustering algorithm.

A successful clustering of two 10 GeV photons can be seen in Figure 7.2. It demonstrates the shape and energy distributions of the 3D clusters. The clusters are centered around the seeds with all the followers creating an energy cloud around them.

7.2 Clustering performance

To evaluate the design of the clustering algorithm, its performance will be studied using single photons with an energy of 10 GeV. The number of reconstructed clusters for such events can be seen in Figure 7.3a. The fact that exactly one cluster is reconstructed for most events indicates a successful clustering. Nonetheless, in 0.6% of the events, more than one cluster is reconstructed. This is a result of fluctuations in the shower development in combination with the workings of the clustering algorithm. The clusters are classified as either leading or sub-leading with the leading cluster being the highest energy one and the sub-leading being all remaining clusters. If multiple sub-leading clusters are reconstructed, these are also catalogued by highest energy. The energy of the first sub-leading cluster for the 10 GeV photons can be seen in Figure 7.3b. It shows that even if a sub-leading cluster is reconstructed, it contains a very small fraction of the initial particle energy. This indicates that only the leading cluster is physically interesting. The choice of dismissing all sub-leading clusters for this performance investigation will therefore have a minimal effect on the total recorded energy of a particle.

7.2.1 Energy response

The energy of the leading cluster along with the total deposited energy is shown in Figure 7.3c. The total recorded cell energy does not match the leading cluster energy as some energy will be lost in the clustering process. The lost energy is contained in possible sub-leading clusters or it is dismissed by the clustering threshold. The latter is an effect of the low threshold excluding some cells, causing an energy loss. This is illustrated in Figure 7.3d where the decrease in number of cells due to the clustering is clear. As a result, the energy distribution of the leading cluster will no longer be centered around the initial energy of the particle, which suggests a need for an energy re-calibration.

The clustering procedure disrupts the linear energy calibration used up to this point and the re-calibration factor is now described by an energy dependent function which can be seen in Figure 7.4a. The re-calibrated energy of the 10 GeV photons can be seen in Figure 7.4b. Similar distributions showing the effect of the re-calibration for different photon and electron energies can be seen in Appendix A.1. The figures show that the re-centering also works for electron clusters.

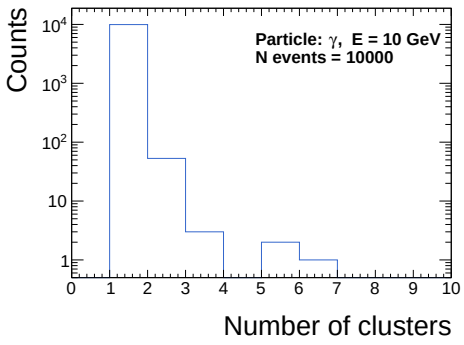

(a) Number of reconstructed clusters per generated photon

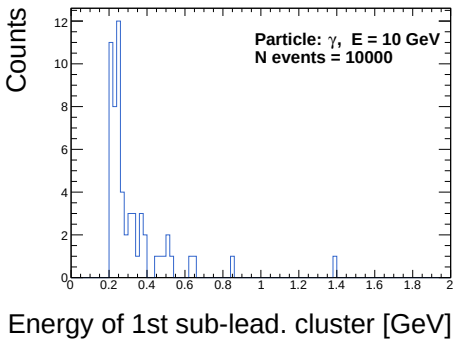

(b) Energy of the first sub-leading cluster

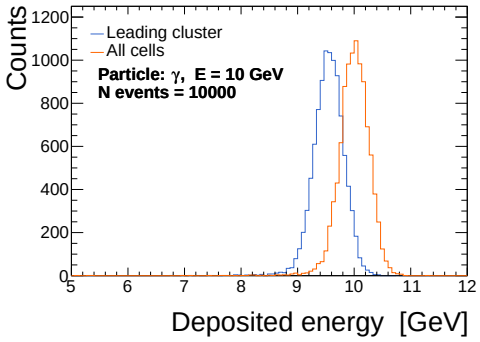

(c) The total energy of all cells compared to the energy of the leading cluster

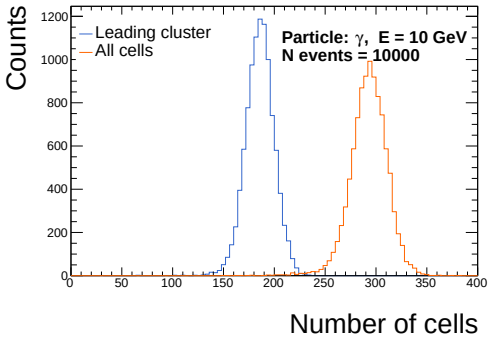

(d) The total number of cells with energy depositions compared to the number of cells in the leading cluster

Figure 7.3: Parameters showing the reconstruction of 10 GeV photons before energy recalibration

The total energy resolution is obtained by fitting a Gaussian function to the energy distribution and is found to be $\frac{\sigma_E}{E} = \frac{8.29\%}{\sqrt{E}}$ as seen in Figure 7.4b. This is a small reduction in precision compared to before the clustering (see Figure 6.8), but this is expected due to the inevitable energy loss. The fact that the energy resolution is only slightly reduced and that the majority of the shower energy is contained within the leading cluster shows that the clustering is successful.

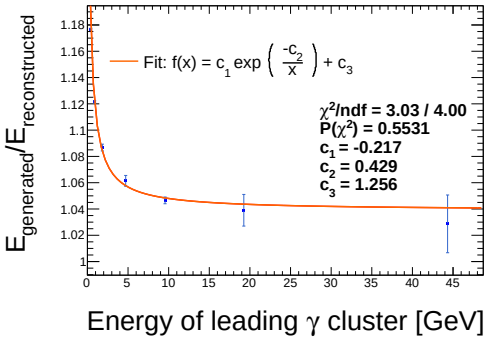

(a) Calibration factor for energy re-calibration as a function of the photon cluster energy

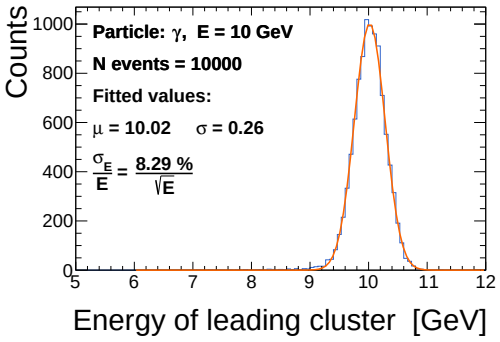

(b) Energy of the leading cluster for 10 GeV photons after energy re-calibration. An energy resolution of $\frac{\sigma_E}{E} = \frac{8.29\%}{\sqrt{E}}$ is obtained

Figure 7.4: The energy re-calibration factor (left) and the resulting calibrated energy for leading clusters of 10 GeV photons (right)

7.2.2 Position resolution

The cluster positions are calculated as the energy weighted mean of the associated cell positions:

$$z_{\text{clus}} = \frac{\Sigma_i E_i z_i}{\Sigma_i E_i} \qquad \text{and} \qquad \phi_{\text{clus}} = \frac{\Sigma_i E_i \phi_i}{\Sigma_i E_i}. \tag{7.1}$$

This procedure provides an $r\phi$ resolution of 1.95 mm for a 10 GeV photon at the inner radius of the ECAL ($r = 2160$ mm). This is already 1/10 of the cell width, but it can be enhanced even further. Figure 7.5 shows the ϕ and z resolutions for 45.6 GeV photons. The double-peak structure is an effect of the continues positions of the generated particles being forced into the discrete cell structure. This causes the difference of the generated and reconstructed coordinates to be described by a so-called s-curve [34]. This behaviour is illustrated in Figure 7.6 which shows the difference between reconstructed and generated coordinates as a function of the reconstructed coordinate. In order to correct this dispersion, a sine function is fitted to the s-curves and the fit result used as a correction. These corrections are displayed in Appendix A.2.

Figure 7.7 shows the ϕ and z resolutions for the 45.6 GeV photons after the correction. The double peak structure has successfully been corrected and the s-curve straightened as seen in Figure 7.8. The resulting position resolution is observed to be energy dependent and Figure 7.9 shows the overall improvement as a function of

the generated photon energy. It is clear that the resolution is especially improved for higher energies. For the 10 GeV photons the $r\phi$ precision at the inner radius of the ECAL is now 1.28 mm. The coordinate resolutions for other photon energies before and after applying the s-curve correction can be seen in Appendix A.2.

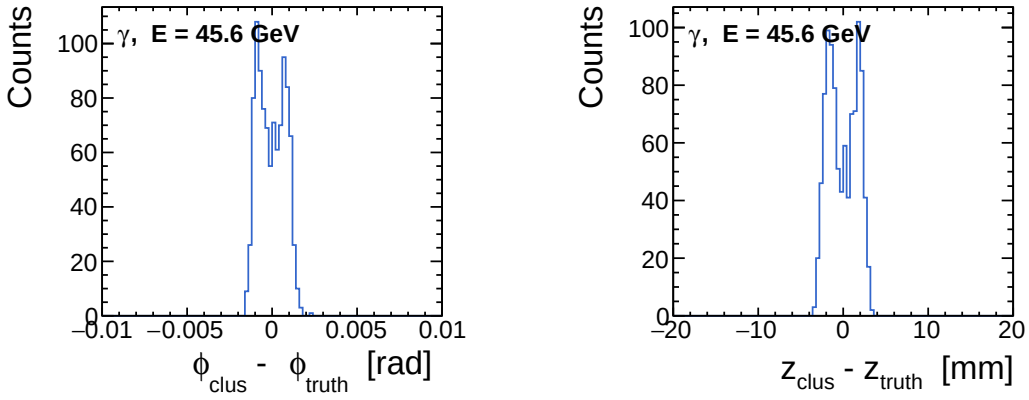

Figure 7.5: The difference in ϕ (left) and z (right) coordinates between generated 45.6 GeV photons and reconstructed clusters before s-curve correction

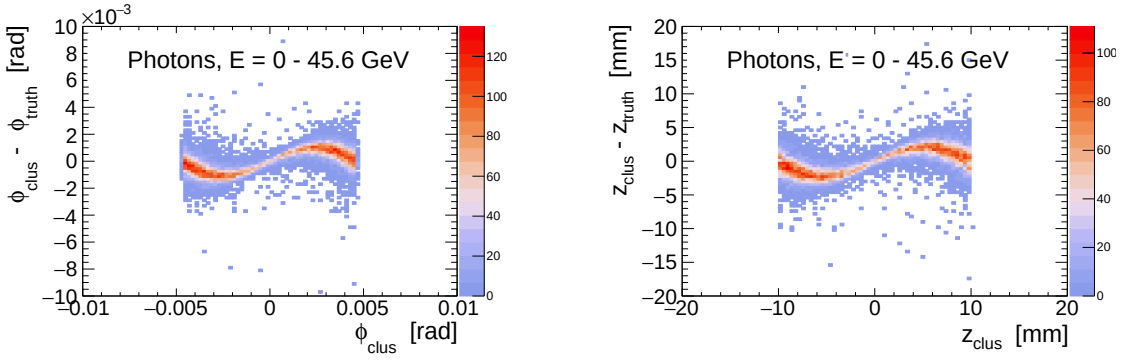

(a) ϕ coordinate **(b)** z coordinate

Figure 7.6: The difference in ϕ and z coordinates between generated photon and reconstructed cluster versus reconstructed coordinate within one cell width before s-curve correction

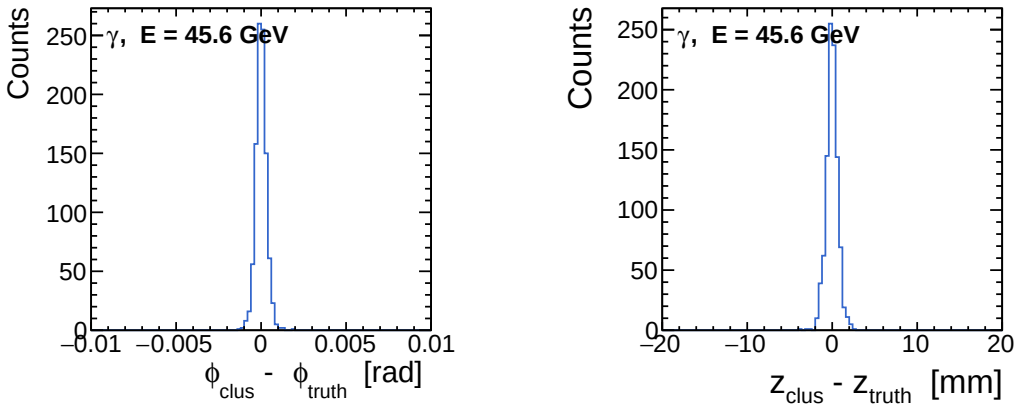

Figure 7.7: The difference in ϕ (left) and z (right) coordinates between generated 45.6 GeV photons and reconstructed clusters after s-curve correction

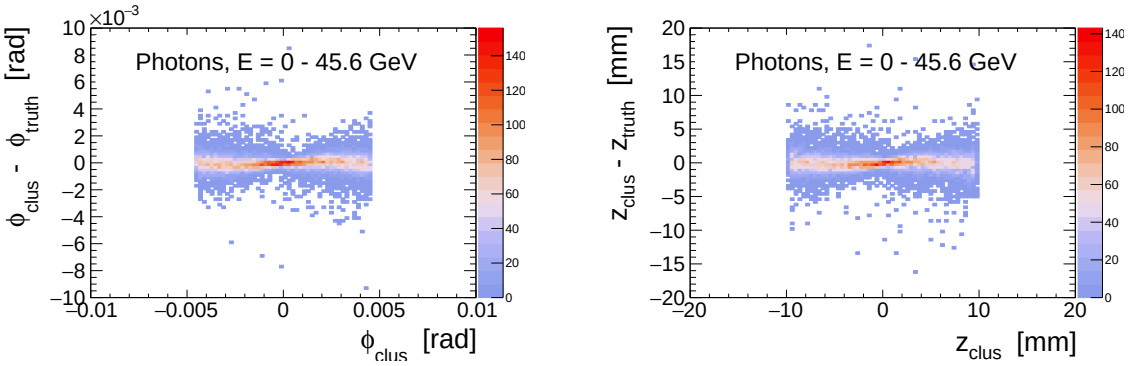

(a) ϕ coordinate **(b)** z coordinate

Figure 7.8: The difference in ϕ and z coordinates between generated photon and reconstructed cluster versus reconstructed coordinate within one cell width after s-curve correction

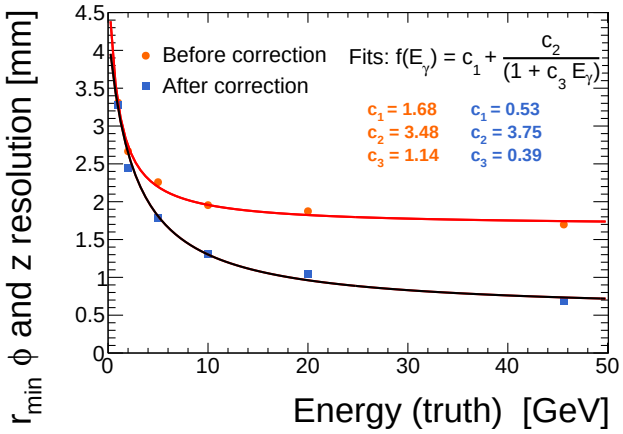

Figure 7.9: The overall $r\phi$ and z resolution before and after the s-curve corrections for 0-45.6 GeV photons

7.2.3 Invariant mass measurement

The position and energy resolutions will both contribute to the width of the π^0-mass distributions. In order to optimize the calorimeter, it is important to identify which contribution dominates. The π^0 mass is found by calculating the invariant mass of the two daughter photons from the π^0. For simplicity, the special case where the photons have equal energy is considered. The total mass can then be found from Eq. 3.11 and the resolution is obtained by

$$\frac{\delta m}{m} = \sqrt{\left(\frac{\delta E}{E}\right)^2 + \left(\frac{\delta \alpha_{\gamma,\gamma}}{\alpha_{\gamma,\gamma}}\right)^2}. \tag{7.2}$$

The energy contribution is simply given by $\frac{\delta E}{E} = \frac{0.083}{\sqrt{E}}$ (from Figure 7.4b) whereas the total $\frac{\delta \alpha_{\gamma,\gamma}}{\alpha_{\gamma,\gamma}}$ contribution for both daughter photons is found as

$$\frac{\delta \alpha_{\gamma,\gamma}}{\alpha_{\gamma,\gamma}} = \sqrt{2}\,\frac{A(E_{\pi^0}/2)}{r}\,\frac{1}{\alpha_{\gamma,\gamma}}. \tag{7.3}$$

The function $A(E_{\pi^0}/2)$ is the fit result from Figure 7.9 taken at half of the π^0 energy and r is the inner radius of the ECAL. As $E_\gamma = E_{\pi^0}/2$, the angle $\alpha_{\gamma,\gamma}$ can be re-written as $\alpha_{\gamma,\gamma} = \frac{2m}{E_{\pi^0}}$ and the position contribution becomes:

$$\frac{\delta \alpha_{\gamma,\gamma}}{\alpha_{\gamma,\gamma}} = \frac{A(E_{\pi^0}/2)}{r}\,\frac{E_{\pi^0}}{\sqrt{2} m_{\pi^0}}. \tag{7.4}$$

The results of the calculation are displayed in Figure 7.10. It can be seen that for energies below 6 GeV, the energy resolution is the biggest contribution to the width of the π^0-mass. Above this point the position resolution dominates. This calculation is only valid in the case where the π^0 daughter photons are reconstructed as two separate clusters (called resolved π^0's). Since the opening angle of the photons is inverse proportional to the π^0 energy, resolved π^0's are mostly found at lower energies and so it is mainly interesting to look at the contributions here. It can therefore be concluded that the energy resolution is the principal contribution to the π^0-mass width for most resolved π^0's. However, the angular resolution quickly becomes dominant when the π^0 energy rises.

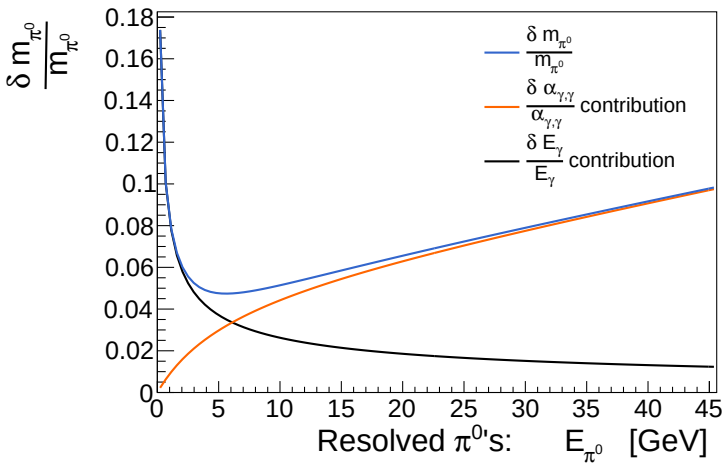

Figure 7.10: Predicted π^0 mass resolution for decays to two equal-energy photons. The contributions from the position resolution (orange) and energy resolution (black) are also shown

7.3 Shower shapes

The ECAL geometry has a high granularity in both the longitudinal and transverse directions. This section studies the difference in shower shapes for various particle species along these directions.

Muons

The results for the clustering of muons can be seen in Figure 7.11. Figure 7.11a demonstrates that a muon signal is being detected in all events. This suggests that the noise levels and clustering thresholds are sufficiently low for gaining a sensitivity to MIP signals. The total and layer-wise cluster energy of these signals can be seen Figure 7.11b and Figure 7.11c, respectively. Because the energy loss of the muons is purely due to ionization, both of these energies are well defined. The energy loss per layer is equal for all layers since the layers are identical in composition. It can be seen that the average energy deposition by a muon is $\sim$ 430 MeV. The reconstruction threshold at 200 MeV should therefore not dismiss any of these clusters. Figure 7.11d shows that muons penetrate the entire ECAL as expected.

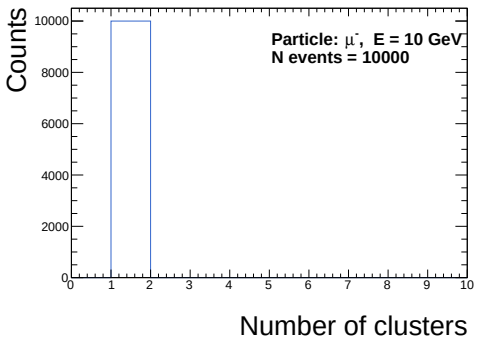

(a) Number of reconstructed clusters per single generated muon

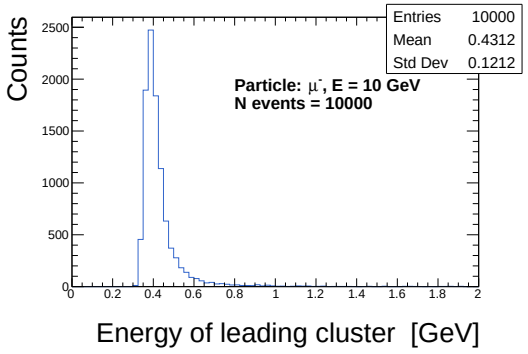

(b) Energy of the leading muon cluster

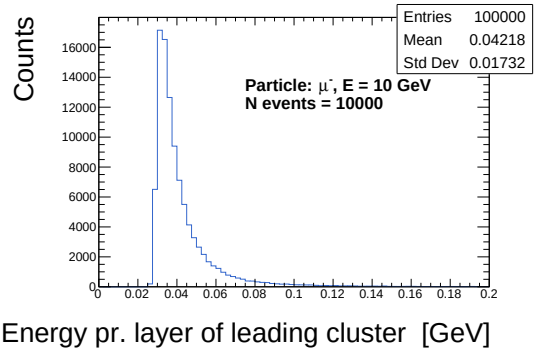

(c) Energy deposited pr ECAL layer for the leading muon cluster

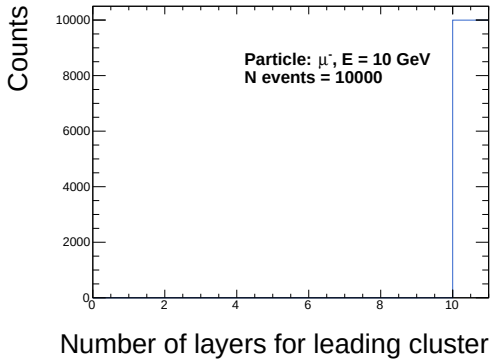

(d) Number of layers penetrated by the muon leading cluster

Figure 7.11: Parameters describing the reconstruction of 10 GeV muons

Charged pions

The results from the clustering of a 10 GeV π^+ signal can be seen in Figure 7.12. The number of clusters per generated particle (presented in Figure 7.12a) is significantly larger compared to the number of clusters reconstructed for both the muons and photons. This is due to the irregular hadronic showers. The average number of additional clusters per generated 10 GeV π^+ is 0.8 clusters. To distinguish the clusters from each other, they are categorised as either associated or non-associated clusters. The classification is based on the proximity to the charged track rather than the energy, since the hadron will not necessarily shower in the ECAL. The associated cluster (there can be maximally one pr track), is the cluster closest to the track and the charged track is approximated by the truth information. If no cluster lies within 0.02 rad of the track, the track has no associated cluster. This can occur if the asymmetric hadronic interactions drags the barycenter of the cluster outside the 0.02 rad cone.

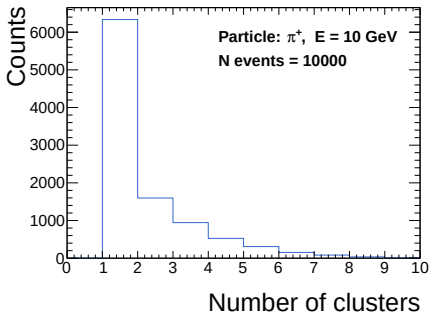

(a) Number of reconstructed clusters per generated π^+

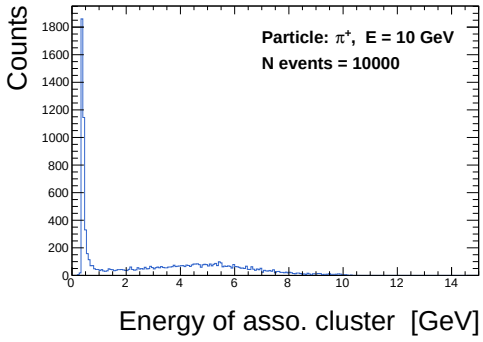

(b) Energy of the associated π^+ cluster

Figure 7.12: Parameters describing the reconstruction of 10 GeV π^+

Figure 7.12b shows the energy of the associated clusters in the 10 GeV π^+ sample. It reveals a clear a MIP peak as well as a continues energy distribution from the hadronic interactions.

The non-associated clusters are neutral objects and are therefore a priori easily confused with photon clusters which may disrupt the decay mode identification. It is therefore important to discriminate between these two types of neutral clusters. Throughout this study, neutral clusters not originating from a π^0 decay will be labeled as fake photons. Section 8.2 presents a fake-photon-killing (FPK) tool for identifying these clusters. The observed π^0 daughter photons are called genuine photons.

Photons, Electrons and π^0's

Photons, electrons and π^0 clusters have several similarities. Photons and π^0's because the π^0 almost immediately decays into photons and photons and electrons because they both interact electromagnetically. Figure 7.13 shows the last ECAL layer reached by either a photon or an electron and indicates that it rises with the energy of the cluster. Both particle species reach the last ECAL layer already at $E > 5$ GeV. Other features of the shower shapes for photons have already been studied section 7.2 along with the energy response of electrons (Appendix A.1).

One of most central observables for a π^0 decay is the opening angle between the daughter photons. This parameter was presented in Figure 6.2e. Using Eq. 3.11 the opening angle for a 20 GeV π^0 can be obtained and is found to be 2.72 cm at the inner radius of the ECAL. With a cell size of $2 \times 2 \times 4$ cm^3 (as used in the simulation), the photons will typically hit two adjoining cells and their clusters are therefore likely to

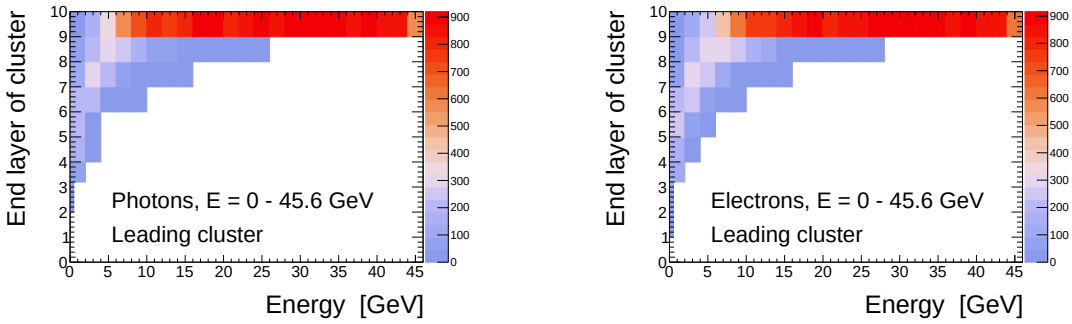

(a) For 0-45.6 GeV photons

(b) For 0-45.6 GeV electrons

Figure 7.13: The last ECAL layer reached by the photon or electron cluster vs. the cluster energy

merge. Figure 7.14 shows the fraction of π^0 events with one or two genuine photons as a function of π^0 energy. It can be seen that for energies above ~ 16 GeV, most daughter photons merge into one cluster and form a so-called unresolved π^0. For 2 GeV $< E <$ 16 GeV the larger opening angle generally allows for separate photon reconstructions, and the two clusters will form a resolved π^0. Below $E = 2$ GeV, many events only contain one cluster. This is typically not due to a merging, but because one of the photons is below the reconstruction limit and this particle will therefore not be observed. The remaining cluster is classified as a residual single photon.

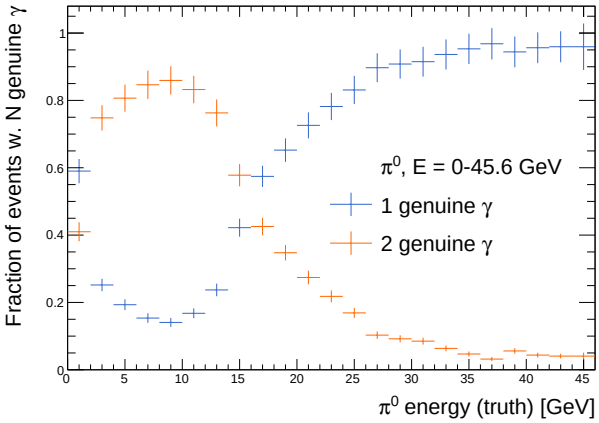

Figure 7.14: The fraction of one or two genuine photons in π^0 events as a function of the π^0 energy

The unresolved π^0's are easily confused with true single γ clusters. Figure 7.15a shows the reconstructed energy for true single photon events, and for π^0 events with one detected genuine photon (a possibly merged π^0). It can be seen that both clusters contain the initial energy of the generated particle. However, Figure 7.15b

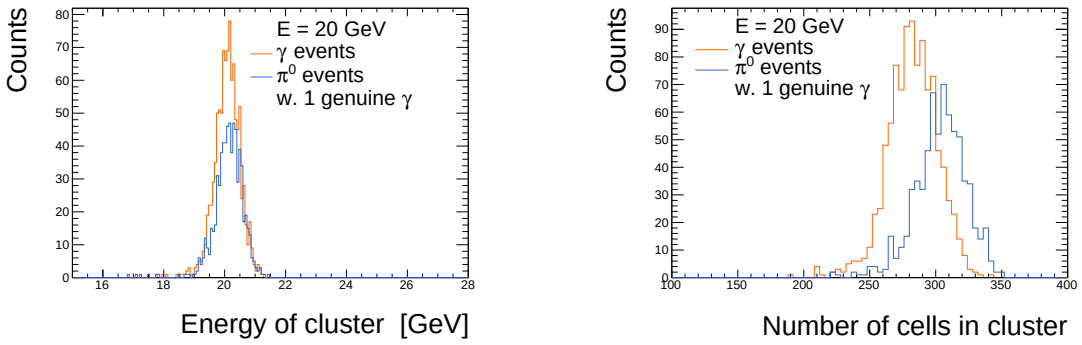

(a) Cluster energy **(b)** Number of cells in a cluster

Figure 7.15: The energy and number of cells contained in clusters from 20 GeV single photon events and one-genuine-photon π^0 events

demonstrates that a larger amount of cells is contained in the π^0 clusters compared to the single photon clusters. This difference indicates a merging of the two daughter photons into an unresolved π^0. Furthermore, it suggests a wider shape of the merged π^0 clusters, which can be used to separate the two neutral clusters. This will be discussed further in section 7.3.2.

7.3.1 Longitudinal shape

The mean longitudinal shower development for electromagnetic showers in the LAr ECAL is shown in Figure 7.16.

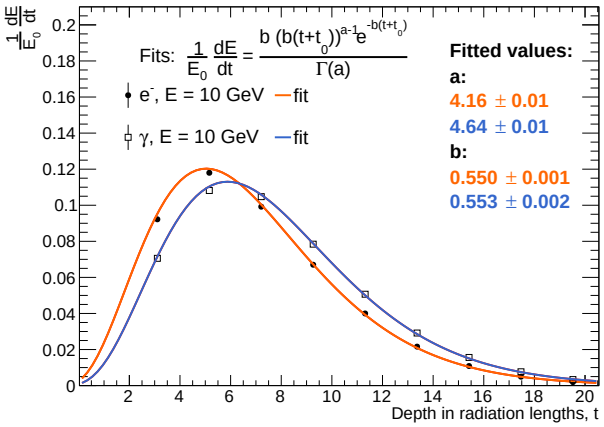

Figure 7.16: Mean longitudinal energy profile of 10 GeV EM showers created by electrons (open square) and photons (filled circles). The constant $t_0 = 0.7X_0$ accounts for the depth of the cryostat and LAr pre-sampler

The data is fitted with the function from Eq. 4.1, describing the mean longitudinal EM shower profile, with the small alteration of $t \to t + t_0$ with $t_0 = 0.7X_0$. This constant describes the depth of the cryostat and LAr pre-sampler placed before the sandwich layers. The distance is included, as passing through these layers affects when the EM shower starts.
The measured profile is consistent with the expected profile. The b-value is expected to be $b \approx 0.5$ which the fits consolidate [24]. The figure also shows that most of the electron/photon energy is deposited in the first five layers. It can be seen that photons on average penetrate more of the ECAL before interacting compared to electrons. The probability of a photon not interacting within depth x is described as

$$P(x) = Ce^{-x/\ell}, \tag{7.5}$$

where ℓ is the mean free path [35]. The mean free path correspond to 9/7 of the radiation length and is therefore expected to be $9/7 \cdot 19.44$ mm $= 24.99$ mm for the LAr ECAL (see Table 6.3). The experimental determination of the photon mean free path can be seen in Figure 7.17. The mean free path is here found to be $\ell = 23.0 \pm 0.4$ mm. This is not completely consistent with the expected value, but the values are close. This could be due to the fact that the distribution is not a perfect decreasing exponential function as seen from the fit.

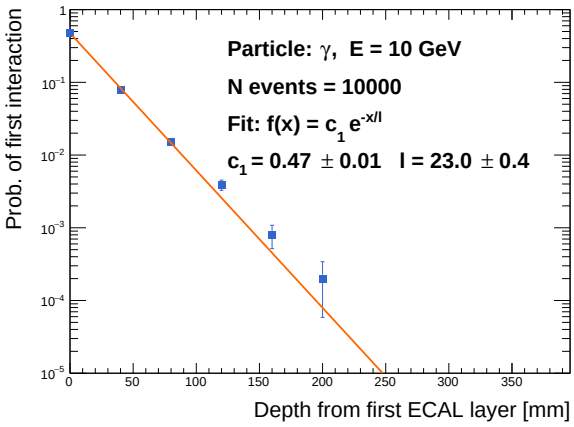

Figure 7.17: The probability of the first interaction of a 10 GeV photon within depth x. The fit result determines the mean free path of the photons to be $\ell = 23.0 \pm 0.4$ mm.

The longitudinal development of hadronic showers is studied using charged pions. Because of their initial MIP signal, a layer-by-layer MIP identification can be applied to $\pi^{\pm}$ samples in order to study the pion interaction as a function of depth. The numerical cut ensures a 99% efficiency for muons throughout all ECAL layers by stating that a MIP deposits less than 120 MeV pr layer. The probability of hadrons

not interacting is also described by Eq. 7.5 but the mean free path, ℓ, is replaced by the interaction length, λ [35]. Figure 7.18 shows the experimentally determined pion interaction lengths for both π^+ and π^- samples. For π^+, $\lambda_{\pi^+} = 499.70 \pm 5.85$ mm whereas for π^-, $\lambda_{\pi^-} = 490.94 \pm 5.71$. The total theoretical pion interaction length is $\lambda_\pi = 404.12$ mm as shown in Table 6.3. The experimental values are therefore not consistent with the calculation but the fits show that the dependence of the interaction probability on the traversed distance is exactly described by Eq. 7.5. A plausible cause the difference between the calculated and observed lengths is the rather loose requirement of 120 MeV on the energy per layer, resulting in not all interactions being observed.

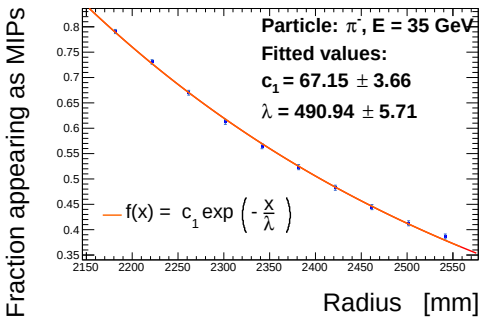

(a) For the π^- sample. The interaction length is found to be $\lambda_{\pi^-} = 490.94 \pm 5.71$ mm.

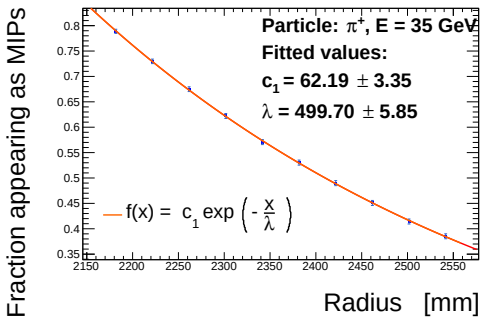

(b) For the π^+ sample. The interaction length is found to be $\lambda_{\pi^+} = 499.70 \pm 5.85$ mm

Figure 7.18: The fraction of $\pi^\pm$ appearing as MIPs as a function of calorimeter depth. The distributions are fitted with a decreasing exponential function to retrieve the pion interaction length

7.3.2 Transverse shape

To determine the size of a shower in the transverse plane, the dispersion (RMS) of the energy around the shower axis is calculated along the two orthogonal directions ϕ and θ. This dispersion-matrix is then diagonalized and the eigenvalues, called principal components, are obtained [36]. A set principal components are illustrated in Figure 7.19. Since the showers are rarely completely symmetric these two principal components will not, in general, be equal. The largest eigenvalue is defined as the major axis and the smallest eigenvalue as the minor axis of the cluster.

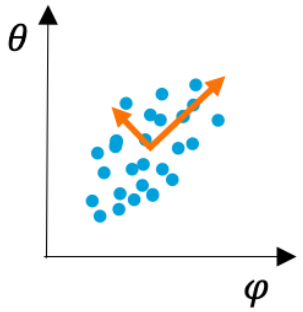

Figure 7.19: Illustration of the two principal components of a cluster

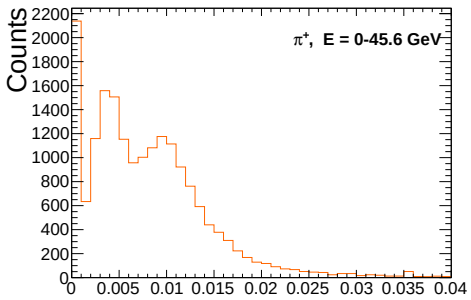

(a) Major axis length for hadronic showers

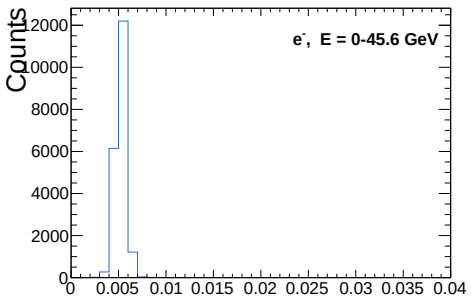

(b) Major axis length for EM showers

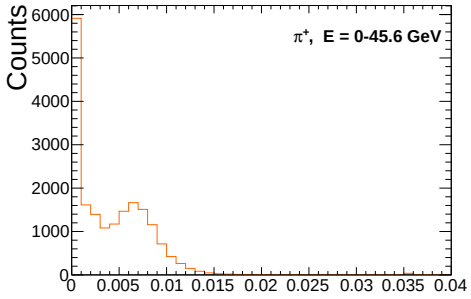

(c) Minor axis length for hadronic showers

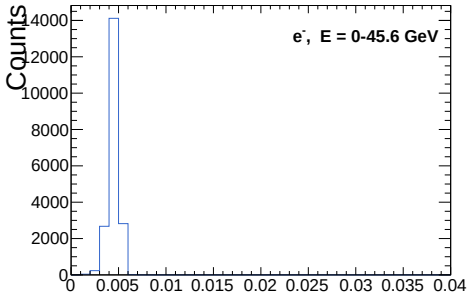

(d) Minor axis length for EM showers

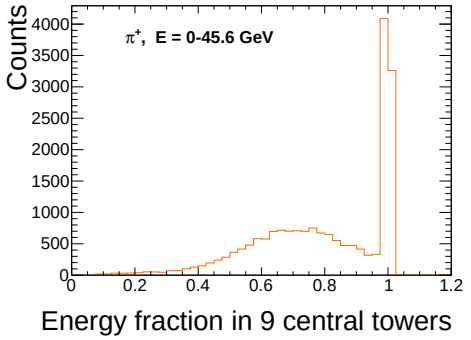

(e) The fraction of energy deposited in the central 9 cell towers for hadronic showers

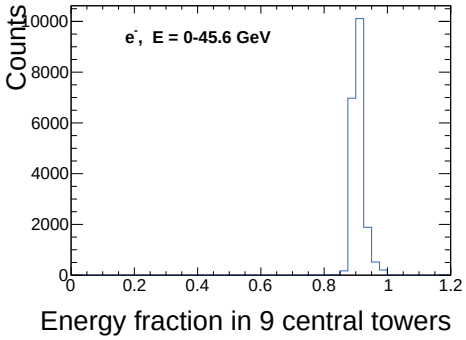

(f) The fraction of energy deposited in the central 9 cell towers for EM showers

Figure 7.20: Transverse shape variables of clusters from hadronic (π^+) and electromagnetic (e^-) showers

The major and minor axis lengths in layer 0-5 for hadronic (π^+) and electromagnetic (e^-) showers can be seen in the top two rows of Figure 7.20. For the electromagnetic showers, both distributions are Gaussian-like as these showers are generally regular in shape. For the hadronic showers there is a peak at very low values which arises from the MIP response, as $\sim 52\%$ of pions have not yet interacted within this first half of the ECAL (see Figure 7.18). The following continuous distribution arises from

the hadronic interactions which can create very wide transverse showers.

Another useful variable to describe the transverse shower profile is the energy fraction contained in the central 9 towers of a cluster (with the most central tower including the cluster seed). This variable is shown in the bottom row of Figure 7.20 for the hadronic and electromagnetic shower, respectively. Due to the regular shape of the EM showers, the energy dispersion is centered around the cluster seed which pushes this fraction towards higher values. The irregular shape of the hadronic showers in general pushes the variable towards lower values, with the exception of the MIP signals where the energy dispersion is extremely small.

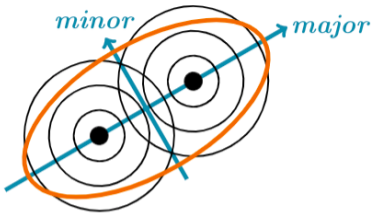

Figure 7.21: The major and minor axis of a merged cluster consisting of two photons

The transverse shower shape is especially important for the unresolved π^0 reconstruction. As both the single photons and unresolved π^0 are electromagnetic showers, their the difference in cluster shape mainly appears in the transverse plane.
The major axis for a merged π^0 cluster will be correlated with the spatial separation of the two photons as shown in Figure 7.21. The major axis length will therefore (in general) be longer for a merged π^0 cluster then for a single photon cluster. As illustrated in the figure, the minor axis will not show the same behaviour.

Figure 7.22 shows the major axis length for different particle energies of clusters from π^0 events with only one genuine photon as well as the major axis length of single photon clusters. For $E = 20$ GeV, it was shown in section 7.3 that most π^0's will be unresolved. This is consolidated by Figure 7.22c which demonstrates a longer major axis for the π^0 events compared to the single photon events.
For 45.6 GeV (Figure 7.22d) the difference between the distributions becomes less significant. This is because the opening angle between the daughter photons is so small that the sub-structure is hard to detect and hence, the difference in major axis length between diminishes.
For the 5 GeV samples (Figure 7.22a) there is no difference between the axis lengths in the two samples. Most of the π^0's are observed as residual single photons at this energy and the major axis lengths are therefore identical.
At 10 GeV (Figure 7.22b) a double peak structure starts to form since some π^0's will be observed as residual single photons, and some will become unresolved π^0's.

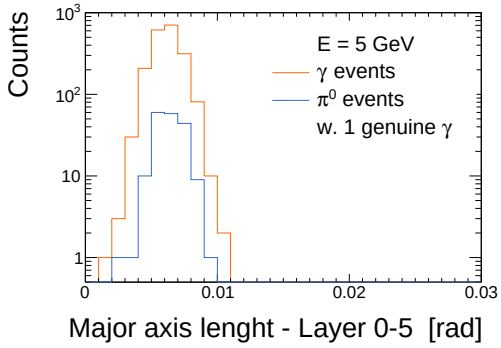

(a) For 5 GeV samples

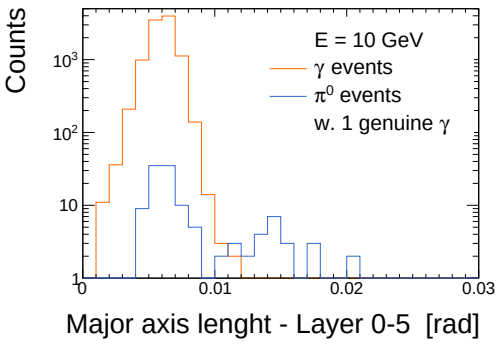

(b) For 10 GeV samples

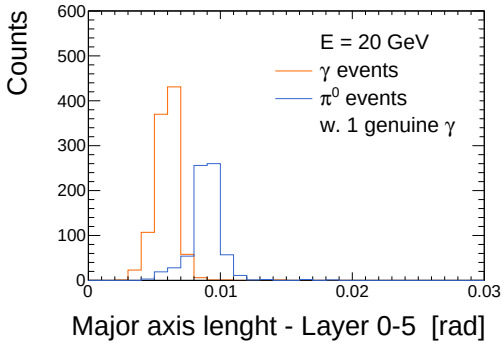

(c) For 20 GeV samples

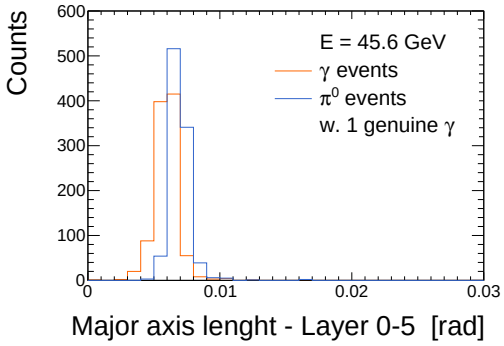

(d) For 45.6 GeV samples

Figure 7.22: The major axis length in layer 0-5 for photon events and one-genuine-photon π^0 events. The axis length is shown for different particle energies

8 Particle identification

A particle identification scheme seeks to classify the reconstructed particles by particle species. Achieving a precise classification requires different separation algorithms, which should be optimized individually. The designs and performances of the particle identification methods implemented for this study will be discussed in the following chapter.

The classification algorithms use different separation variables. An example of such a variable is the fraction of the track momentum a charged particle deposits in the ECAL. For MIPs this will be a very low fraction as they only loose energy due to ionisation, but for an electron this fraction will be close to 1. A separation of MIPs and electrons could therefore be achieved by enforcing a cut on this variable. To achieve a clear separtion, more than one cutting variable are often used.

8.1 Electron classification

When identifying electrons, it is important to have a clear separation of electrons and charged pions. The implemented separation exploits several differences between hadronic and EM showers. The signal in this separation is associated clusters of electrons with $E = 1 - 45.6$ GeV and the backgrounds are associated clusters of π^+ and π^- samples with $E = 1 - 45.6$ GeV. Particles with $E < 1$ GeV are neglected in this method since they would spiral and never reach the ECAL in the real detector due to the magnetic field.

The first separation variable is the E/p variable, where E is the cluster energy and p is the track momentum. The initial distributions of this cutting variable for the background and signal samples can be found in the first row of Figure 8.1. An electron deposits most of its energy in the ECAL giving $E/p \sim 1$ whereas $E/p < 1$ for many hadronic showers. The applied cut is $1 - 4\sigma_{E/p} < E/p < 1 + 4\sigma_{E/p}$ with a lower limit of $E/p > 0.8$. The energy dependence of $\sigma_{E/p}$ can be found in Appendix B. Applying this cut preserves only 1.4% of the π^+ events and 1.0% of the π^- events

while 99.4% of the e^- events remain. The different efficiencies for the two background samples could be related to the possibility of charge exchange for π^+ particles. Charge exchange is the process $\pi^+ + n \rightarrow p^+\pi^0$. As a p^- cannot be created because the ECAL consists of matter rather than anti-matter this process does occur for π^-. If charge exchange happens early in the ECAL more of the track momentum will be contained in the cluster, resulting in a higher E/p-value for the π^+ samples.

The second cut uses the transverse shower profile. A major axis cut enforces 0.002 rad $< major <$ 0.008 rad and preserves 70.0% of the π^+ background and 72.4% of the π^- background whereas 0.03% of the signal events are dismissed. The major axis distributions are shown in the second row of Figure 8.1.

The last separation variable is the energy fraction in the first three ECAL layers. It is shown in the third row of Figure 8.1. As hadrons tend to interact later than EM particles, this fraction is lower for hadron showers. The cut is defined as $E_{lay} > \mu_{E_{lay}} - 3\sigma_{E_{lay}}$ with $E_{lay} = E_{layer\,0-3}/E_{tot}$. Both the mean energy fraction and its standard deviation are energy dependent and described by the fits displayed in Appendix B. The cut conserves 64.6% and 68.1% of the π^+ and π^- samples respectively and 99.4% of the e^- sample.

Applied Cuts	**Background:** π^+ / π^-			**Signal:** e^-		
	Num. par	ϵ_{cut}	Accu. ϵ	Num. par	ϵ_{cut}	Accu. ϵ
None	π^+: 19264 π^-: 19256	1. 1.	1. 1.	19555	1.	1.
$1 - 4\sigma_{E/p} < E/p < 1 + 4\sigma_{E/p}$ $E/p > 0.8$	π^+: 270 π^-: 199	0.014 0.010	0.014 0.010	19440	0.994	0.994
$major >$ 0.002 rad $major <$ 0.008 rad	π^+: 189 π^-: 144	0.700 0.724	0.010 0.007	19434	1.	0.994
$E_{lay} = E_{layer\,0-3}/E$, $E_{lay} > \mu_{E_{lay}} - 3\sigma_{E_{lay}}$	π^+: 122 π^-: 98	0.646 0.681	0.006 0.005	19308	0.994	0.987

Table 8.1: Cuts applied in the electron identification method. Both the individual efficiency of cut i and the accumulated efficiency of each additional cut is shown. Both the background (π^+/π^-) and signal (e^-) samples have energies $E = 1 - 45.6$ GeV

All separation variables, along with the individual and accumulated efficiencies are summarised in Table 8.1. The distributions of the variables following each cut can be seen in Figure 8.1. The total efficiency of the separation leaves only 0.6% of the π^+ events, 0.5% of the π^- events while preserving 98.7% of the electron signal. It is clear that the E/p cut is especially effective for achieving a clean separation.

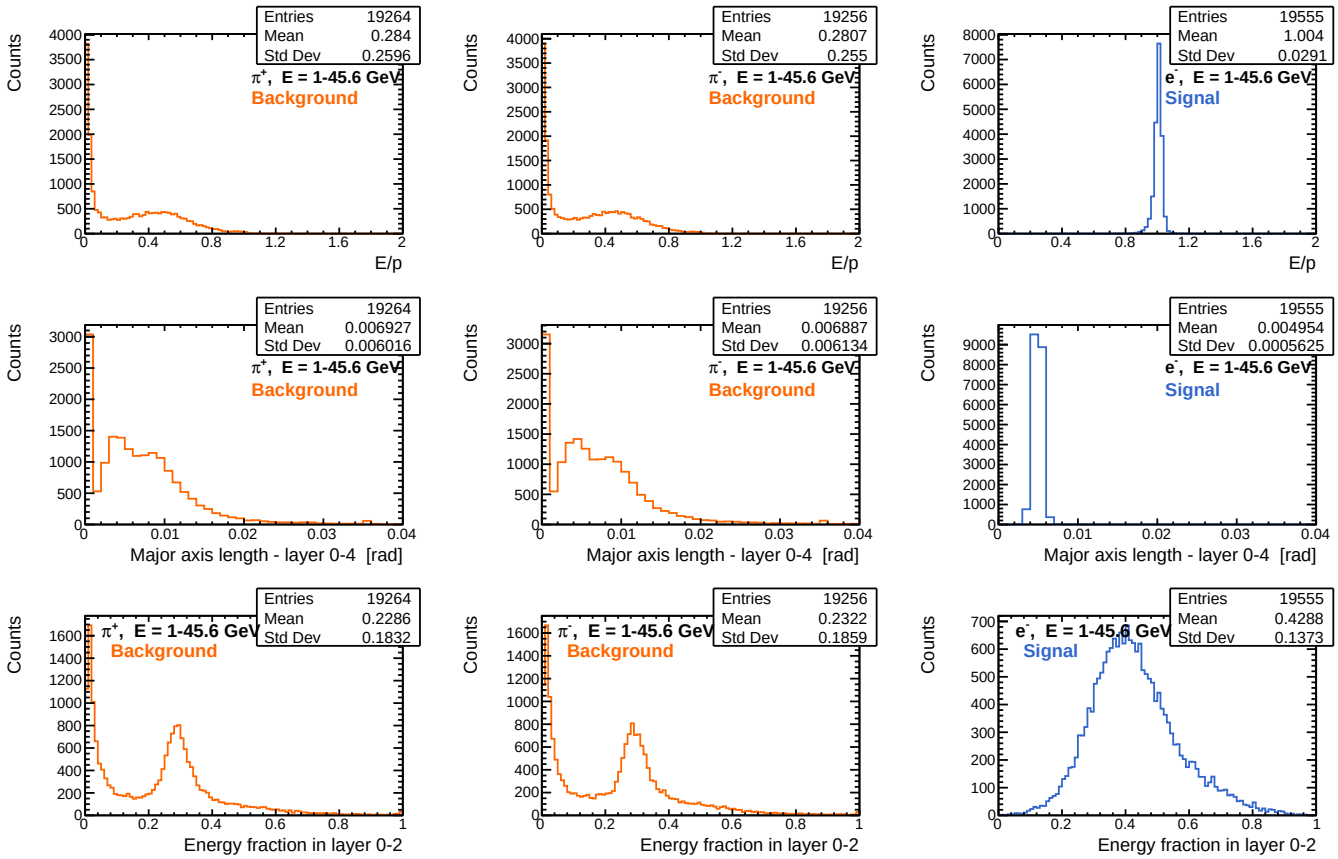

Figure 8.1: Initial distributions of the cutting variables used in $e^-/\pi^\pm$ separation for both background (π^+/π^-) and signal (e^-) samples

8.2 Fake photon killing

A $\pi^\pm$ event will contain several fake photons. Identifying and dismissing these fake photons is of great importance as a fake photon could be falsely interpreted as a π^0.

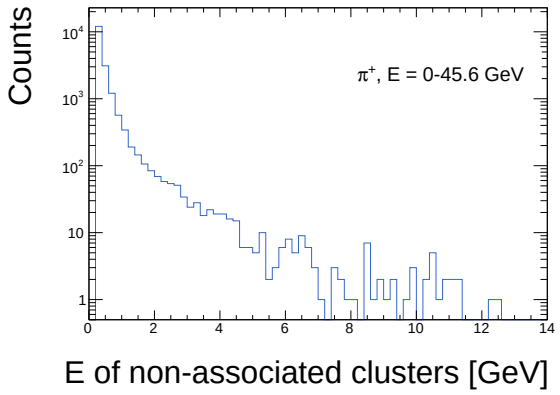

Figure 8.2: Energy of all non-associated clusters from 0-45.6 GeV charged pions

Fake photon clusters mostly have low energies as seen in Figure 8.2. Many of the fake photons actually have energies below the reconstruction threshold of 200 MeV. The limit reduces the number of fakes by a factor ~ 4 which results in an average of 0.9 fake photons per 20 GeV π^+ before the Fake Photon Killing (FPK).

The remaining fake photons are frequently confused with low energy sin-

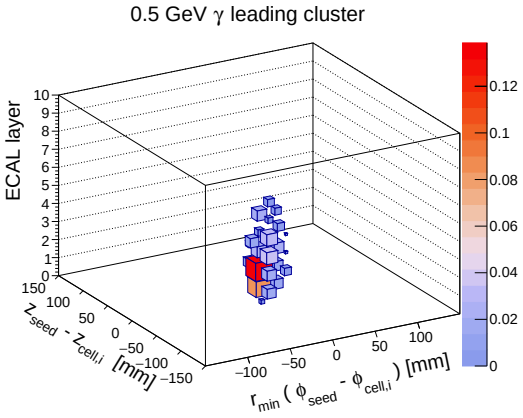

(a) The leading cluster from a 0.5 GeV γ

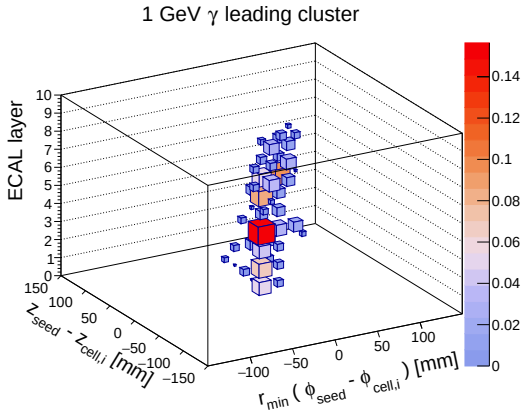

(b) The leading cluster from a 1 GeV γ

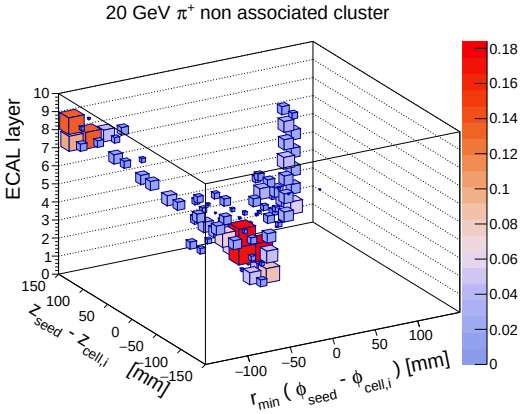

(c) A fake photon cluster from a 20 GeV π^+

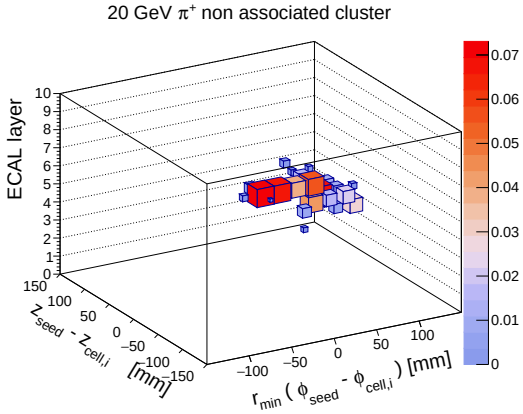

(d) A fake photon cluster from a 20 GeV π^+

Figure 8.3: Examples of single photon clusters (top) and fake photon clusters (bottom). The clusters are centered around the cluster seeds

gle photons. For this reason, the separation of the two is focused on low energy clusters with $E < 5$ GeV. Neutral clusters above this energy are automatically accepted as genuine photons. The photon identification is based on five separation variables. The signals are leading clusters from two low energy single photon samples with $E = 0.5$ GeV and $E = 1$ GeV. The background is non-associated clusters with $E < 5$ GeV from 20 GeV π^+ events.

Figure 8.3 shows examples of clusters from single and fake photons. Since the fake photons arise from hadronic interactions, their showers are much more irregular. Many of the separation variables exploit this difference.

The first separation variable is the energy fraction contained in the highest energy ECAL layer. The initial distribution of this variable for the background and signal samples can be seen in the first row of Figure 8.4 and the separation limit set at

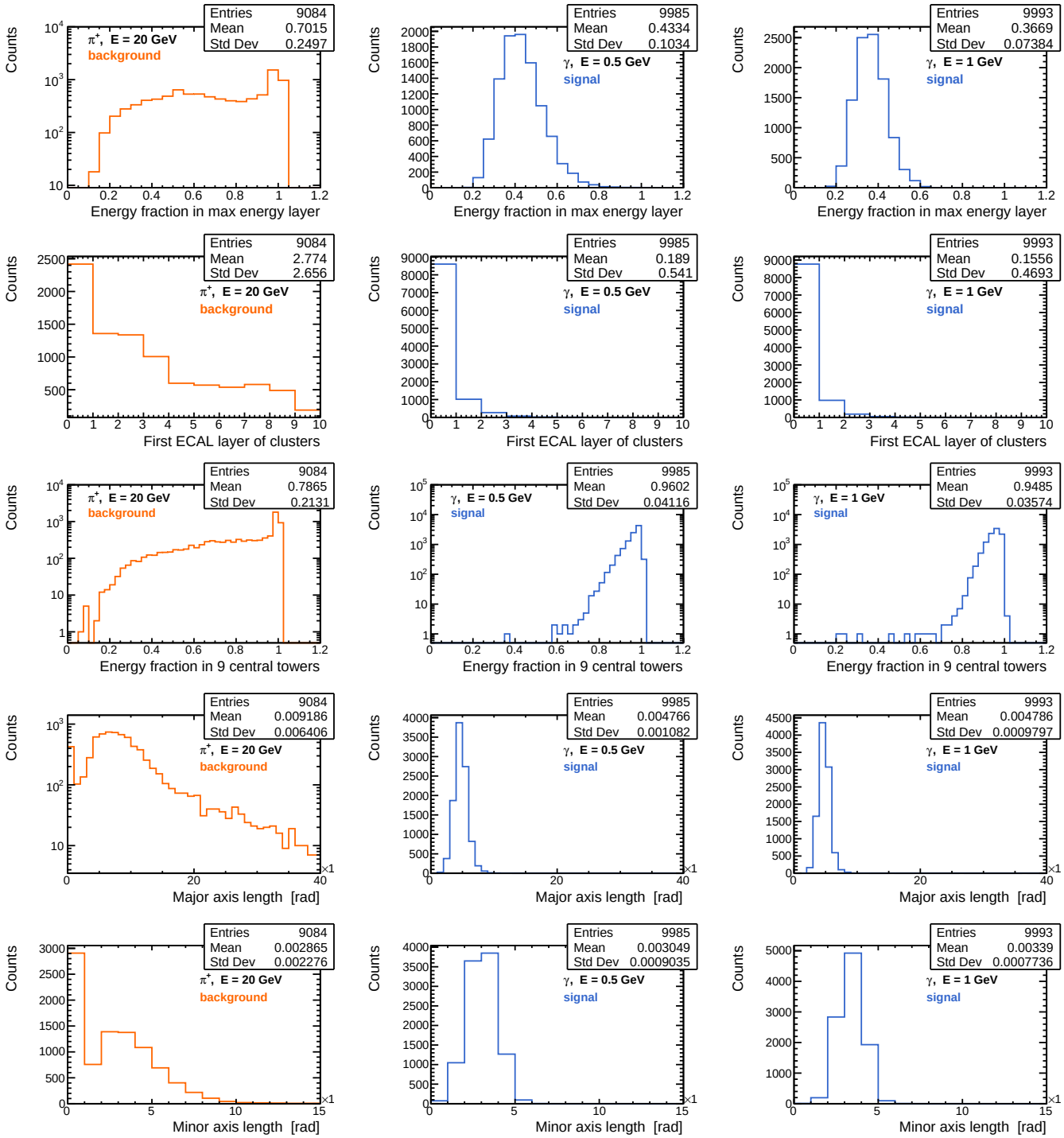

Figure 8.4: The distributions of separation variables for the FPK before any cuts are applied for both background and signal samples

$E_{lay}/E \leq 0.6$. Since photons penetrate many layers, they are likely to fulfill this demand in contrast to fake photons. The cut preserves 37.7% of the background and 93.6 % and 99.7 % of the 0.5 GeV and 1 GeV signal, respectively.

Applied Cuts	**Background:** Non-asso. π^+ 20 GeV			**Signal:** γ: 0.5 GeV / 1 GeV		
	Num. par	ϵ_{cut}	Accu. ϵ	Num. par.	ϵ_{cut}	Accu. ϵ
None	9084	1.	1.	**0.5 GeV:** 9985	1.	1.
				1 GeV: 9993	1.	1.
$E_{lay}/E \leq 0.6$	3424	0.377	0.377	**0.5 GeV:** 9350	0.936	0.936
				1 GeV: 9966	0.997	0.997
$Lay_{start} < 2$	1748	0.511	0.192	**0.5 GeV:** 9003	0.963	0.902
				1 GeV: 9718	0.975	0.972
$E_{9\,towers}/E \geq 0.85$	500	0.286	0.055	**0.5 GeV:** 8801	0.978	0.881
				1 GeV: 9603	0.988	0.960
$major \leq 0.008$ rad	391	0.782	0.043	**0.5 GeV:** 8763	0.996	0.877
				1 GeV: 9580	0.998	0.959
$minor > 0.001$ rad	352	0.900	0.039	**0.5 GeV:** 8713	0.994	0.873
$minor \leq 0.006$ rad				**1 GeV:** 9578	1.	0.958

Table 8.2: An overview of the cuts applied in the FPK. Both the individual efficiency of cut i and the accumulated efficiency of each additional cut is shown. The background is all non-associated clusters from 20 GeV π^+ events and the signals are leading clusters of 0.5 GeV and 1 GeV single photon events.

The second separation variable is the first layer with recorded energy deposition. This variable is shown in the second row of Figure 8.4. Since fake photons are mostly secondary particles, they tend to start later in the ECAL. Only clusters starting in layer 0 or 1 will pass through this cut. Applying it preserves 51.1% of the remaining background events, 96.3% of the 0.5 GeV signal events and 97.5% 1 GeV of the signal events.

The last three cuts all concerns the transverse shower profile. The fourth cut enforces a constraint on the energy fraction in the central 9 towers and the fifth and sixth cuts enforces constraints on the major and minor axis lengths, respectively. The limit of the fifth separation variable is $E_{9\,towers}/E \geq 0.85$ and the efficiency is 28.6% for the background sample, 97.8% for the 0.5 GeV signal sample and 98.8% for the 1 GeV signal sample. The major axis cut is $major \leq 0.008$ rad and preserves 78.2% of the remaining background and 99.6% and 99.8% of the remaining 0.5 GeV and 1 GeV signal, respectively. The minor axis cut enforces 0.001 rad $< minor \leq 0.006$ rad with an efficiency of 90.0% for the background, 99.4% for the 0.5 GeV signal and 0.02% for the 0.5 GeV signal.

An overview of the separation variables, the cutting limits and the cut efficiencies can be seen in Table 8.2. The distributions of all separation variables following each cut can be found in Appendix C. After the five cuts, the number of fake photons pr charged hadron is reduced by approximately a factor 26 to 0.035 fakes pr hadron. This leaves 3.9% of the background while preserving 87.3% of the 0.5 GeV signal and 95.8% of the 1 GeV signal.

8.3 Separation of unresolved π^0 and single γ

The separation of unresolved π^0's and single photons is based on a difference in major axis lengths as explained in section 7.3.2. The major is however only correlated with the opening angle between the photons but does not describe it directly. It is therefore convenient to reformulate this property into a more intuitive quantity, namely the invariant mass. The cluster mass can be calculated from the principal components as:

$$m_{\text{clus}} = c_1 E_{\text{clus}} x \tag{8.1}$$

with c_1 being a calibration factor and $x^2 = major^2 - minor^2$. To avoid statistical fluctuations, the average minor axis length for π^0 events with $E > 12$ GeV is used. It is found to be $\mu(minor) = 0.0057$ rad. The major axis is calculated for each shower individually. The calibration factor has value $c_1 = 0.9854$ with a small linear energy dependent correction.

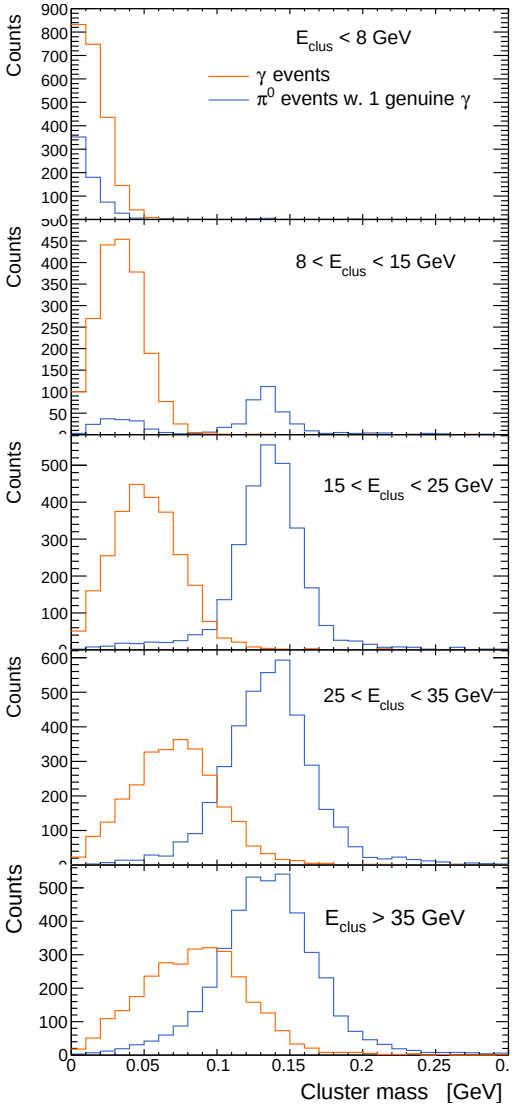

Figure 8.5: The cluster mass of single γ events (orange) and π^0 events with one genuine photon (blue)

The invariant mass distributions for single photons and one-genuine-photon π^0

events for different energy ranges is presented in Figure 8.5. For all energies above 8 GeV a peak at the π^0 mass can be seen for the π^0 sample. Below 8 GeV the clusters from π^0 events are inconsistent with the π^0 mass as these one-genuine-photon events most likely contain residual single photons instead of unresolved π^0. For energies between 8-15 GeV the double peak structure shows that both residual single photons and unresolved π^0's are present. For energies above this point, a wide peak around the π^0 mass is clear while the single γ peak remains inconsistent with the mass. This variable can therefore be used for a separation of the two, with the cleanest separation achieved in the energy range 8-25 GeV. For higher energies the mass peaks become more indistinguishable and it becomes harder to perform the separation. This is due to the diminishing cluster sub-structure at high energies which smears the peaks. Based on these results, a unresolved π^0 is defined as having $m > 0.1$ GeV.

9 Results

After implementing the necessary methods, the π^0 reconstruction and the decay mode identification can take place. The decay mode identification is based on a π^0 counting method along with some optimizations. Applying these optimizations requires a thorough understanding of the physics processes and analysis aspects causing confusion in the decay classification, and implementing them therefore becomes challenging.

The results for the π^0 reconstruction will be compared with similar results from the ALEPH experiment to evaluate the performance of the LAr ECAL. A direct comparison of the decay mode identification to ALEPH results is not possible due to the unrealistic kinematics of the full τ decays, but some interesting contrasts will be presented.

9.1 π^0 reconstruction

The goal of the π^0 reconstruction is finding every π^0 in an event without including any fakes. In order to only reconstruct true π^0's, the reconstruction is build on top of the FPK.

Decaying particles are (in general) reconstructed by combining the measured decay products and comparing their invariant mass to the mass of the assumed mother particle. The daughter photons therefore have to be reconstructed separately (resolved π^0's). However, as described in section 7.3.2, the π^0's can also be observed as either unresolved clusters or single residual photons. Every genuine photon should therefore be considered for all three types. The algorithm ensures that a genuine photon can only be accepted as one type of π^0. This method will first combines all genuine photon clusters and identifies all resolved π^0's. Then the π^0/γ separation is used to select the unresolved π^0's from the remaining clusters. Finally, the residual single photons are found from the leftover genuine photons. The results and the detailed method for reconstructing each type of π^0 is presented in the next sections.

9.1.1 Resolved π^0's

Finding resolved π^0's is the first step of the π^0 counting algorithm. The method calculates the invariant mass of all possible genuine photon pairs and compares the results to the true π^0 mass. If the mass is consistent with the π^0 mass, the photon pair is confirmed as a resolved π^0. A complication is that a genuine photon can appear in more than one accepted pair. To address this issue, the photon pair with the mass closest to the true π^0 mass will be selected first and these photons will not be included in other pairs. This selection will continue until there are no more photon pairs with an acceptable invariant mass. The accepted mass range is $m_{\pi^0} - 4\sigma_{m_{\gamma,\gamma}} < m_{\gamma,\gamma} < m_{\pi^0} + 4\sigma_{m_{\gamma,\gamma}}$ where $\sigma_{m_{\gamma,\gamma}}$ is found by fitting a Gaussian to the distribution of all two-genuine-photon events for the $\tau \to \pi^{\pm}\pi^0\nu$ channel. This fit is shown in Figure 9.1. With $\sigma_{m_{\gamma,\gamma}} = 0.010$, the numerical cut becomes $95\,\text{MeV} < m_{\gamma,\gamma} < 175\,\text{MeV}$. The figure additionally shows that the invariant mass of the photon pairs is centered around the true π^0 mass essentially without any background. Having such a distinct peak at the π^0 mass demonstrates the a successful suppression of fake photons.

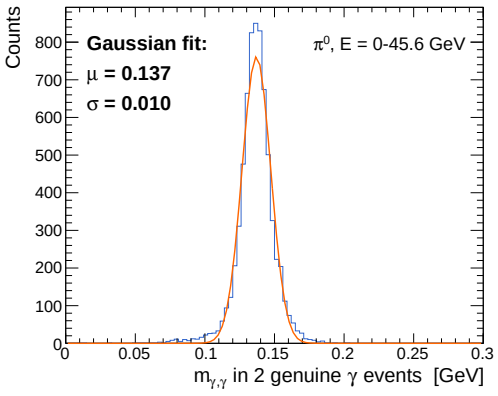

Figure 9.1: The invariant mass of two genuine photons in π^0 events

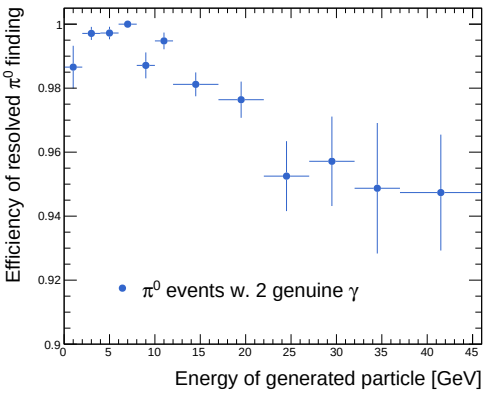

Figure 9.2: The efficiency of the resolved π^0 finding

The efficiency of the resolved π^0 finding can be seen in Figure 9.2. It shows an efficiency of $\epsilon > 94\%$ for the entire energy range. For energies below 16 GeV the efficiency rises even further to $\epsilon_{E<16\text{GeV}} > 98\%$ which is important since most resolved π^0s will have energies within this range (see section 7.3).

9.1.2 Unresolved π^0's

The unresolved π^0's are found among the genuine photons remaining after the resolved π^0 finding. As described in section 8.3, the biggest background for this π^0 type is the single photons. The cluster mass calculations presented in this section are used for the unresolved π^0 identification.

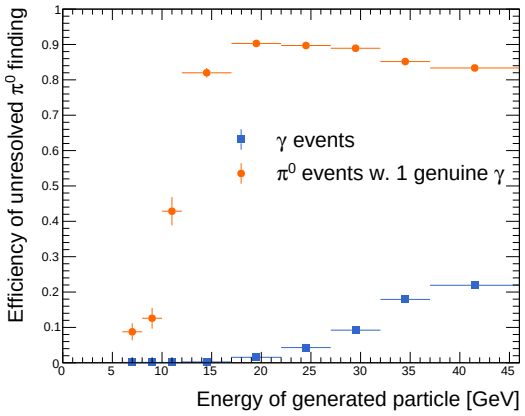

Figure 9.3: Efficiency of the unresolved π^0 finding for single γ events (background) and for one-genuine-photon π^0 events (signal)

Based on Figure 8.5, a genuine photon cluster with $m > 0.1$ GeV will be categorized as an unresolved π^0. Figure 9.3 shows the efficiency of the separation as a function of energy for both the background and signal samples. The signal efficiency is low for energies below $E < 15$ GeV. This is because many of the one-genuine-photon events will contain a residual single photon instead of an unresolved π^0s at this energy, which brings down the fraction of identified unresolved π^0's. For higher energies, the wide π^0 mass peaks of Figure 8.5 reduces the efficiency.
The figure shows that the amount of unresolved π^0's found in the background sample rises at higher energies, which is expected from Figure 8.5. In real τ decays not many π^0's will have energies above 25 GeV (see Figure 3.8d) and so, it is most important that the separation works below this limit, which seems to be the case. The efficiency in the limit $E > 16$ GeV for the signal sample is $82 - 90\%$.

9.1.3 Residual single photons

The residual single photons are, as stated earlier, resolved π^0's where one photon is most likely below the reconstruction limit. These clusters are thereby actual single photon clusters which greatly complicates distinguishing them from single

photons. There are in general not many single photons in a hadronic τ decays and so assuming all remaining genuine photons to be residual single photons seems acceptable. However, this is only true if efficiency of the PFK is high and if there are no radiation photons. Radiation photons are photons from other processes besides the τ decay and can for example arise from initial or final state radiation. They will most likely pass through the FPK but should of cause not be accepted as a residual single photon. In order to suppress the radiation photons, only genuine photons within a 0.3 rad cone of the $\pi^{\pm}$ track are accepted as single residual photons. The limit is based on the distribution shown in Figure 6.2f. The previous π^0 from the residual single photons will also be included in the total π^0 counting.

9.1.4 Summary of π^0 reconstruction

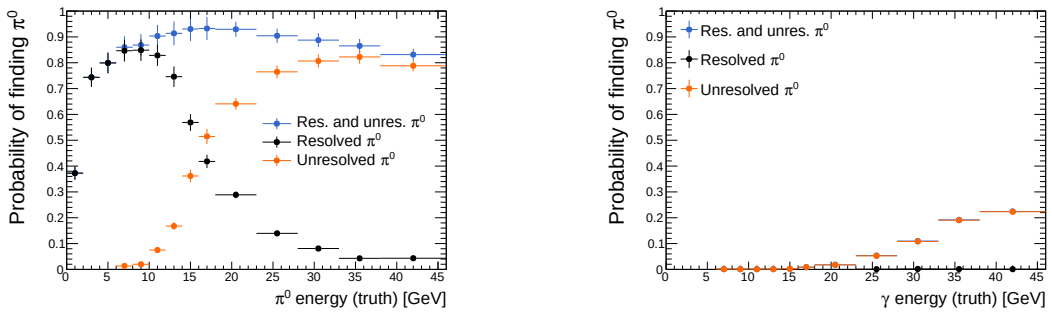

(a) For π^0 events

(b) For γ events

Figure 9.4: The probability of identifying a π^0 in π^0 and photon events

Figure 9.4 shows the efficiency of the overall π^0 reconstruction as a function of the π^0 energy, along with the contributions from resolved and unresolved π^0 identifications, respectively. The probability of reconstructing a π^0 is generally above 80%, but drops for $E < 5$ GeV. The decrease is due to the fact many generated π^0 at low energies will be observed as residual single photons and are therefore not identified by the two methods shown here. A decrease is also seen at high energies because the sub-structure of the unresolved clusters diminishes, and so these clusters might not be accepted as unresolved π^0's but instead as single residual photons.
Figure 9.4a furthermore shows that at energies below 16 GeV, the dominant observed π^0 type is the resolved π^0's. Above this point, the probability of observing an unresolved π^0's exceeds the probability of observing resolved π^0's as the photon clusters are more likely to merge.

The overall probability of reconstructing a π^0 as either resolved or unresolved for

all energies combined is 83.88% (using SPG events). For the ALEPH analysis this efficiency was $\sim 84\%$ [37]. This number, however, also includes the residual single photons which are not included in the 83.88%. The average probability of falsely accepting a photon as a π^0 is 4.38%, dominated by high energy photos due to the wider cluster mass distributions here. Fortunately, there are not many high-energy single photons in τ decays. The result achieved in this analysis is competitive with the ALEPH results and suggests that the proposed LAr ECAL is a promising calorimeter option for improving the π^0 reconstruction.

9.2 The hadronic migration matrix

The implementation of the π^0 reconstruction scheme enables a π^0 counting and thereby a decay channel classification of the hadronic τ decays. The inter-channel separation is based on the number of identified π^0s with a few optimizations to avoid common pitfalls. A central aspect is minimizing the number of radiation photons. Besides the restrictive cone for the genuine photons, it is also demanded that $0.2 < m_{\pi^\pm,\gamma} < 1.8$ GeV for any photon to be considered a genuine photo, with the upper limit being the τ mass. The full invariant mass distribution can be found in Appendix D.1.

The second optimization determines whether the π^0 and the $\pi^\pm$ merged into one cluster. In this instance the cluster would most likely be categorized as the $\pi^\pm$ associated cluster and the π^0 would be lost.
The merged clusters are defined as events where the associated $\pi^\pm$ cluster has $E/p > 1.2$. An E/p value exceeding this threshold is most likely because the cluster contains more than the $\pi^\pm$ particle. Such clusters are present in 0.12% of events for hadron decay channel, 2.38% of events for the $\pi^\pm\pi^0\nu$ channel, 6.50% of events for the $\pi^\pm 2\pi^0\nu$ channel and 12.06% of events for the $\pi^\pm 3\pi^0\nu$ channel. For the hadron channel, the charged pions most likely merge with radiation photons. To account for the lost π^0's, the merged clusters are included in the π^0 counting, if the event does not contain any residual single photons. The residual single photon identification already counteracts loosing π^0's, and so only merged events without these photons are considered (see Appendix D.2).
There are two complications regarding this optimization method: it does not allow for separate energy measurements of the charged and neutral pions, which is required for polarisation measurements, and it cannot account for more than one π^0 being

Recon → Gen ↓	$\pi^{\pm}\,\nu$	$\pi^{\pm}\,\pi^{0}\,\nu$	$\pi^{\pm}\,2\pi^{0}\nu$	$\pi^{\pm}\,3\pi^{0}\nu$	$\pi^{\pm}\,4\pi^{0}\nu$
$\pi^{\pm}\,\nu$	**0.9560**	0.0425	0.0010	0.0003	0.0002
$\pi^{\pm}\,\pi^{0}\,\nu$	0.0374	**0.9020**	0.0586	0.0016	0.0002
$\pi^{\pm}\,2\pi^{0}\nu$	0.0090	0.1277	**0.7802**	0.0808	0.0022
$\pi^{\pm}\,3\pi^{0}\nu$	0.0036	0.0372	0.2679	**0.5972**	0.0910

Table 9.1: The migration matrix of the hadronic the τ decays considered in this analysis. Each row shows the fraction of e.g. $\tau \to \pi^{\pm}\nu$ decays classified as each of the considered channels

contained in the $\pi^{\pm}$ cluster. The latter mainly affects the $\pi^{\pm}3\pi^{0}\nu$ channel to which the polarisation measurements are less sensitive. A more consistent method should be developed in future studies, however, for the current analysis this simple optimization is sufficient and leads to a more precise decay channel classification.

The resulting migration matrix can be seen in Table 9.1. The diagonal elements of the matrix dominate for all the decay channels, which means that the majority of events will be correctly classified for every decay mode. The precision is especially impressive for the $\pi^{\pm}\nu$ and $\pi^{\pm}\pi^{0}\nu$ channels where decays are categorized correctly for 96% and 90% of the events. This is a noteworthy result since these channels are most important for τ polarisation measurements (see section 3.1.1). For the two remaining channels, the precision decreases due to the rising combinatorics of the many photons. Precisions of 79% for the $\pi^{\pm}2\pi^{0}\nu$ channel and 60% for the $\pi^{\pm}3\pi^{0}\nu$ channel are obtained.

The $n_{\pi^0} > 1$ channels primarily show a migration of events towards channels with fewer π^{0}'s, which indicates that some π^{0}'s are not reconstructed. Nonetheless, the main migration of the $\pi^{\pm}\pi^{0}\nu$ is towards the $\pi^{\pm}2\pi^{0}\nu$ channel, suggesting that the feed-up mechanisms are also present. The migration matrix from this study shows the same tendencies for upwards or downwards migration as the migration matrix obtained by the ALEPH experiment (see Table 3.2). For instance, the considerable amount of $\pi^{\pm}\,3\pi^{0}\nu$ decays classified as $\pi^{\pm}\,2\pi^{0}\nu$ decays. This indicates that in spite of the unrealistic kinematics of the decays in this analysis, it is the same convoluted physics that complicates the two analyses. The increase in precision in the migration matrix in this analysis is therefore first and foremost a demonstration of the high performance ECAL. The results presented in Table 3.2 generally suggests that using a LAr ECAL looks promising for obtaining a precise τ decay mode separation. To further show the purity of the selection, the invariant mass of two photons in events

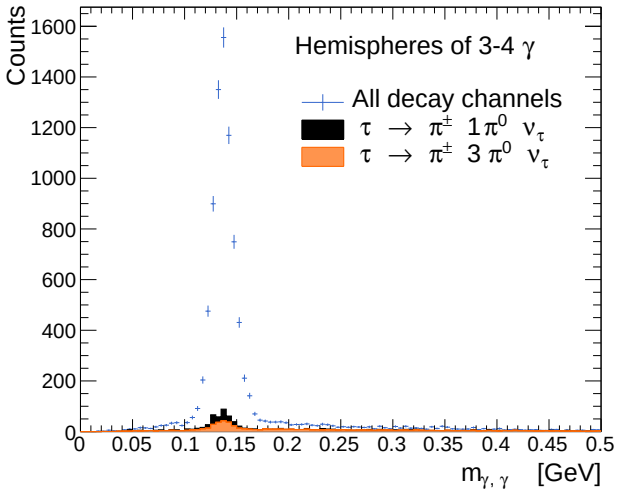

Figure 9.5: $\gamma\,\gamma$ mass of additional photons in hemispheres where one π^0 has already been identified. The first reconstructed π^0 is the most energetic. The background contributions are scaled by the their cross section relative to the $\tau \to \pi^\pm\, 2\pi^0\nu$ cross section

where one π^0 has already been identified is shown in Figure 9.5. Each background is scaled by their respective cross section (relative to the signal) and their contributions are shown. A major peak around the π^0 mass is shown with limited background. For the $\pi^\pm\pi^0\nu$ background channel, a peak at the π^0 mass shows that the second identified π^0 is actually a real π^0. This occurs when the first π^0 identified is a radiation photon being accepted as a residual single photon. Afterwards, the true π^0 is found and so the $\pi^\pm\pi^0\nu$ channel is mis-classified as the $\pi^\pm 2\pi^0\nu$ channel. However, this background contribution is small and the overall limited background supports the conclusion that the ECAL design seems well suited for achieving the desired decay mode separation.

Recon → Gen ↓	$\pi^\pm\,\nu$	$\pi^\pm\,\pi^0\,\nu$	$\pi^\pm\,2\pi^0\nu$	$\pi^\pm\,3\pi^0\nu$	$\pi^\pm\,4\pi^0\nu$
$\pi^\pm\,\nu$	**0.9859**	0.0129	0.0008	0.0001	0.0003
$\pi^\pm\,\pi^0\,\nu$	0.0351	**0.9338**	0.0300	0.0011	0.0001
$\pi^\pm\,2\pi^0\nu$	0.0084	0.1314	**0.8050**	0.0546	0.0003
$\pi^\pm\,3\pi^0\nu$	0.0031	0.0360	0.2673	**0.6138**	0.0792

Table 9.2: The migration matrix of hadronic τ decays for events not containing any radiation photons. Each row shows the fraction of e.g. $\tau \to \pi^\pm\nu$ decays classified as each of the considered channels

The biggest contribution to the decay mode mis-classifications is due to radiation photons. To show their impact on the migration matrix, the matrix is re-calculated for events without these photons. The result is presented in Table 9.2. It shows a significant enhancement of the diagonal elements of $\sim 3\%$ for the hadron, $\pi^{\pm}\pi^{0}\nu$ and $\pi^{\pm}2\pi^{0}\nu$ channels and 1.7% for the $\pi^{\pm}3\pi^{0}\nu$ channel. Identifying and dismissing these radiation photons is therefore vitally important. Dismissing the radiation photons mostly reduces the upwards migration of the decays, and an improved method for radiation photon classification in future studies would therefore mainly leave the down-wards migration. This would simplify later optimizations as it allows for mainly concentrating on the feed-down mechanisms.

10 Alternative noble liquid electromagentic calorimeters

After having conducted a thorough study of the proposed LAr ECAL, a shorter analysis investing the LKr ECAL will now be presented. The goal of this simple comparison is not determining the entire migration matrix but rather obtaining the resolved and unresolved π^0 results as this indicates the efficiency of future decay mode identifications. It is therefore not necessary to implement all analysis elements from the previous LAr ECAL study. The π^0 reconstruction only requires SPG events without charged pions, which means that the amount of fake photons is negligible. The approximation that the constructed clusters correspond to physical particles is therefore used for this study. Throughout all the analysis, the clustering limits are kept fixed at $\text{thrs}_{low} = 10$ MeV and $\text{thrs}_{high} = 20$ MeV along with the reconstruction limit at $E_{cluster} > 200$ MeV.

The π^0 reconstruction is performed analogously to the methods presented in section 9.1. First, all resolved π^0's are identified by requiring $m_{\pi^0} - 4\sigma_{m_{\gamma,\gamma}} < m_{\gamma,\gamma} < m_{\pi^0} + 4\sigma_{m_{\gamma,\gamma}}$ where $\sigma_{m_{\gamma,\gamma}}$ is the standard deviation of the invariant mass distribution of two-cluster π^0 events. Subsequently, the unresolved π^0's are identified by selecting clusters with mass $m_{clus} > 0.1$ GeV.

Since the cell size of the LKr design is only $1 \times 1 \times 2.6$ cm^3 it is important to isolate the effect this change will have from the effects of changing the ECAL materials. Therefore, a revised LAr ECAL of the same smaller cell size ($1 \times 1 \times 4$ cm^3) will be discussed first and compared to the initial LAr design.

10.1 A revised liquid argon design

As for the initial LAr ECAL, the revised ECAL must be properly re-calibrated after the clustering. These calibrations are performed in the same manner as the calibration of the intial LAr design presented in section 7.2. The result of the energy

calibration for the revised ECAL can be seen in Figure 10.1a. It shows an energy resolution of $\frac{\sigma_E}{E} = \frac{8.91\%}{\sqrt{(E)}}$ which is comparable with the initial LAr ECAL resolution of $\frac{\sigma_E}{E} = \frac{8.29\%}{\sqrt{(E)}}$.

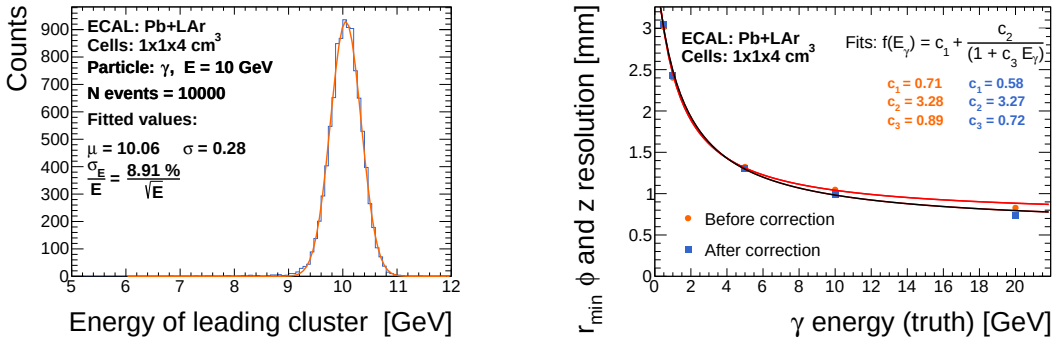

(a) Energy of the leading cluster after energy re-calibration

(b) The position resolution before and after s-curve correction

Figure 10.1: Energy calibration and position correction for the revised LAr ECAL

The result of the s-curve correction is shown in Figure 10.1b. The distributions showing full correction method can be found in Appendix E. Unlike for the initial design, this correction does not show a considerable impact on the overall angular resolution. With a smaller cell size, the discrete cell structure becomes less significant and so the s-curve smearing of angles diminishes. The s-curve correction improves the $r\phi$ and z resolution for 10 GeV photons from 1.04 mm to 0.98 mm. A comparison of the angular resolutions after the s-curve correction for both the initial and revised LAr design can be seen in Figure 10.2. It shows that the smaller cell size provides a higher resolution throughout the entire energy range.

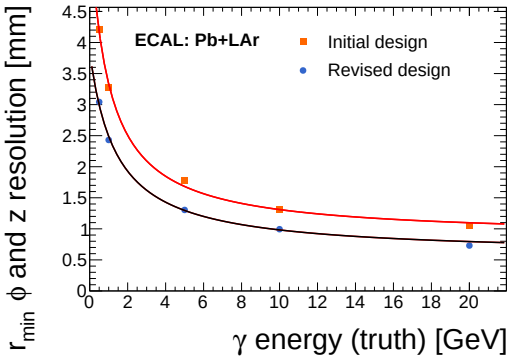

Figure 10.2: The $r\phi$ and z resolutions of the initial and revised LAr ECALs after the s-curve correction

After the re-calibration, the number of clusters can be studied. To eliminate effects of not using a FPK in this analysis, the study of the initial LAr design is repeated using the simplified method for all plots in this chapter. The number of clusters per generated single photon for each of the two cell structures can be seen in Figure 10.3a and 10.3b. They show that the smaller cells seed more clusters, most likely because they are more sensitive to energy fluctuations within a shower. The average number of so-called fake clusters per generated photon is 0.04 for the initial ECAL whereas it is 0.12 for the revised ECAL.

Figure 10.3c and 10.3d show the fraction of one- and two-cluster π^0 events as a function of the π^0 energy. For both cell structures, it is possible to detect two clusters in a fraction of the events up to the maximal energy. For the revised LAr design, this fraction is higher for all energies. However, since the number of fake clusters per generated photon is higher for the this design, some of the two-cluster events will contain one fake cluster.

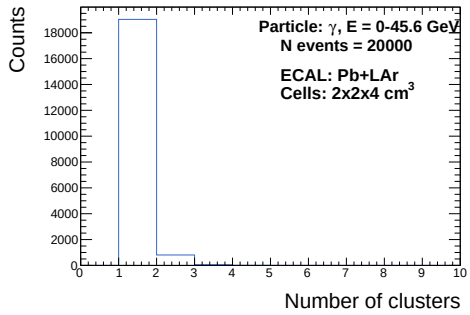

(a) Number of reconstructed clusters per generated photon in the initial LAr ECAL

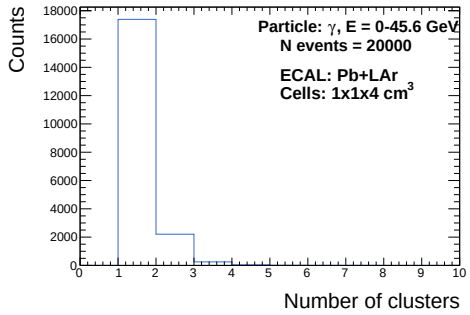

(b) Number of reconstructed clusters per generated photon in the revised LAr ECAL

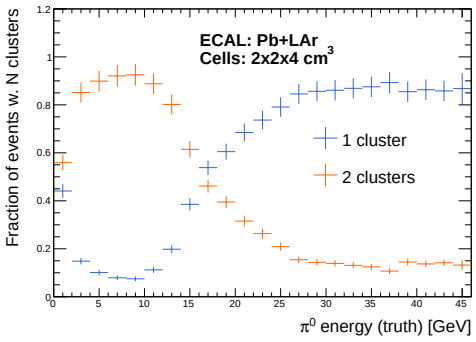

(c) The fraction of events with one or two clusters for π^0 events in the initial LAr ECAL

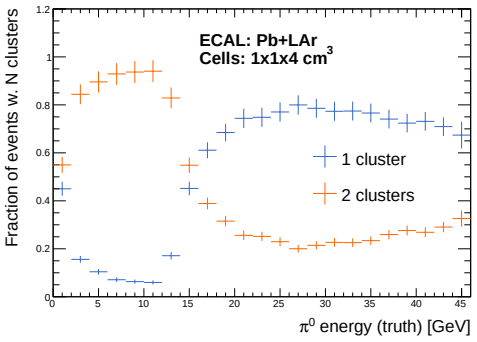

(d) The fraction of events with one or two clusters for π^0 events in the revised LAr ECAL

Figure 10.3: The number (top) or fraction (bottom) of recorded clusters per photon (top) or π^0 (bottom) for the initial and revised LAr ECAL

Figure 10.4 shows the invariant mass of two-cluster π^0 events for both the initial and revised LAr cell structures. The larger amount of fake clusters create a background distribution for the revised design. However, the figure shows a dominant peak at the π^0 mass, which indicates that most two-cluster events will contain a resolved π^0. The smaller cell sizes result in a narrower π^0 mass distribution with a width of $\sigma = 0.009$ GeV compared to $\sigma = 0.011$ GeV for the initial cells.

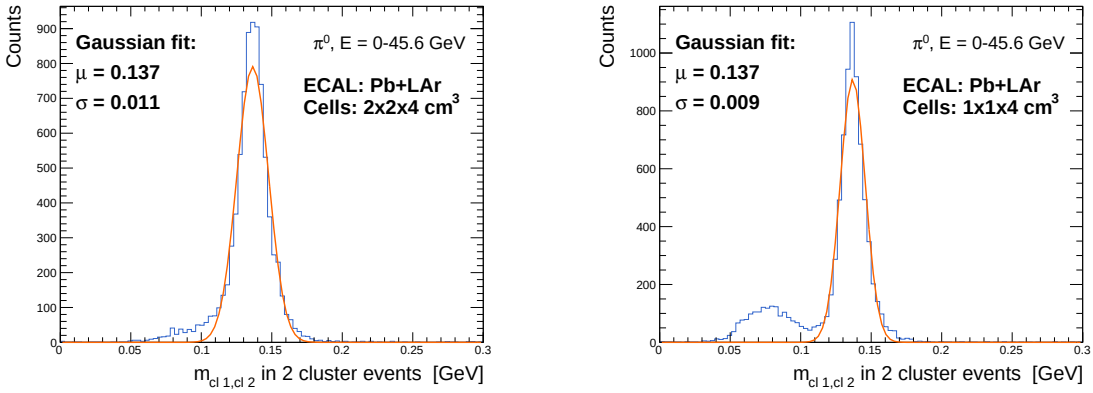

(a) For the initial LAr ECAL **(b)** For the revised LAr ECAL

Figure 10.4: The invariant mass of two clusters in π^0 events

The cluster mass distribution of single photons and one-cluster π^0 events for both cell structures is shown in Figure 10.5. It is calculated in the same manner as presented in section 8.3. The mean minor axis for the initial LAr ECAL is $\mu(minor) = 0.0058$ rad whereas it is $\mu(minor) = 0.0043$ rad for the revised ECAL. The discrepancy suggests that cell sizes of the initial ECAL contribute to the total width of the showers which means that decreasing the cell size to 1 cm might enhance the precision of the cluster mass measurements. As seen in Figure 10.5, the π^0 mass peaks are much wider for the initial LAr ECAL than for the revised design, which significantly improves the separtion of single photons and unresolved π^0's, especially for the 25-35 GeV samples.

Based on Figures 10.4 and 10.5 it is possible to implement cuts to identify resolved and unresolved π^0's. Resolved π^0s are accepted if $\mid m_{cl1,\,cl2} - m_{\pi^0} \mid < 4\ \sigma_{m_{cl1,\,cl2}}$. For the initial LAr ECAL this implies 95 MeV $< m_{cl1,\,cl2} <$ 175 MeV and for the revised detector the limits are 99 MeV $< m_{cl1,\,cl2} <$ 171 MeV. For both ECALs, unresolved photons are defined as one-cluster events with $m_{clus} > 100$ MeV.
The number of reconstructed π^0's per event can be seen in Figure 10.6. It shows that a π^0 is reconstructed in most events, for both cell structures. It additionally demonstrates that the larger amount of fake clusters for the revised LAr design does

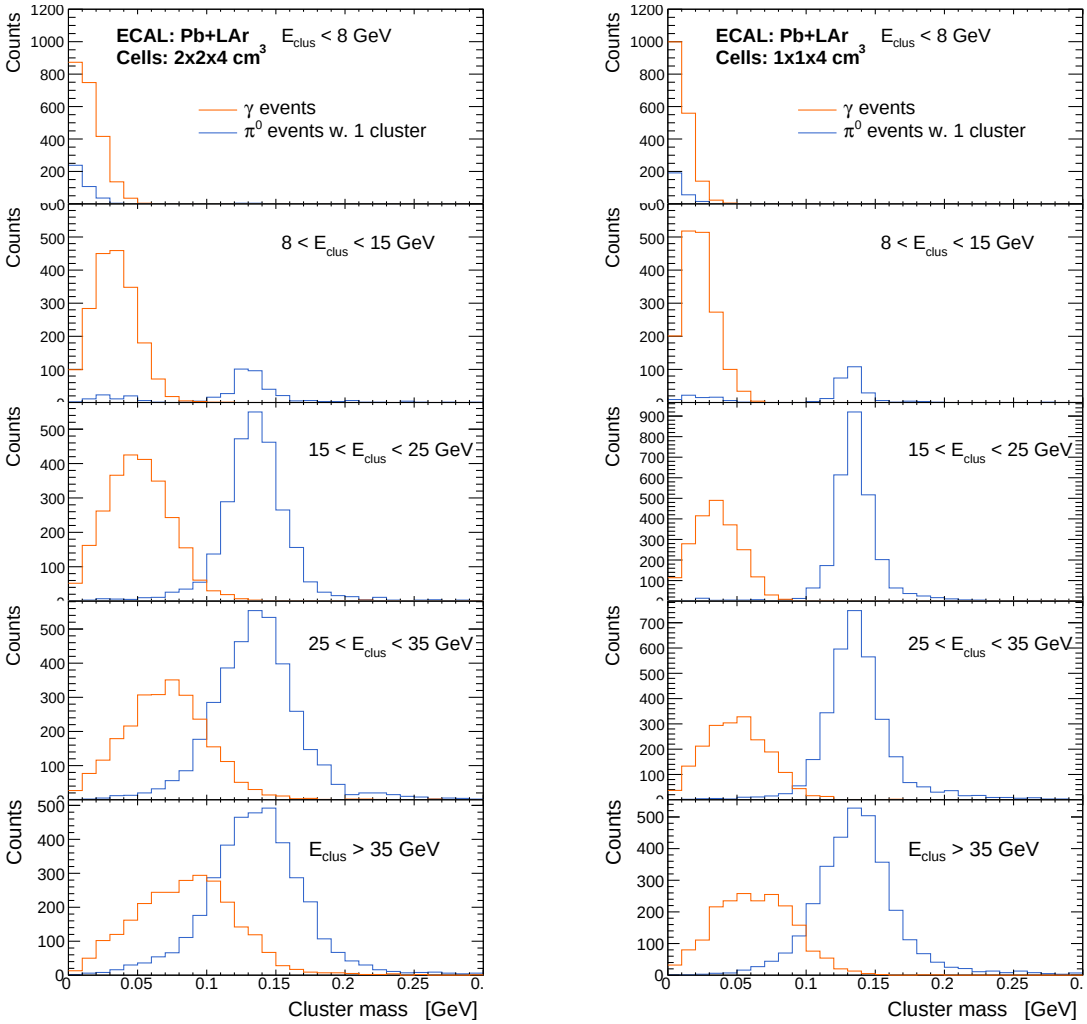

(a) For the initial LAr ECAL

(b) For the revised LAr ECAL

Figure 10.5: Cluster mass of one-cluster π^0 and single photon events

not lead to a significant amount of fake π^0's, which supports the argument that a FPK is not necessary for this simplified analysis.

The total efficiency of the π^0 reconstruction method for both the initial and revised LAr ECALs can be seen in Figure 10.7. The plots in the top row show the probability of reconstructing a π^0 in π^0 (signal) events whereas the bottom plots show the same feature but in single photon (background) events. The average probability of reconstructing a π^0 is 89.23% and 91.09% for the initial and revised designs, respectively. The reconstruction probability in the signal events exhibits the same behaviour for both cell structures. At very low energies many π^0's will be observed as residual single photons, which lowers the probability here. The probability rises with increasing π^0 energy, since more π^0's are observed as either resolved or unresolved events, with the latter dominating at higher energies. Due to the increasing smearing

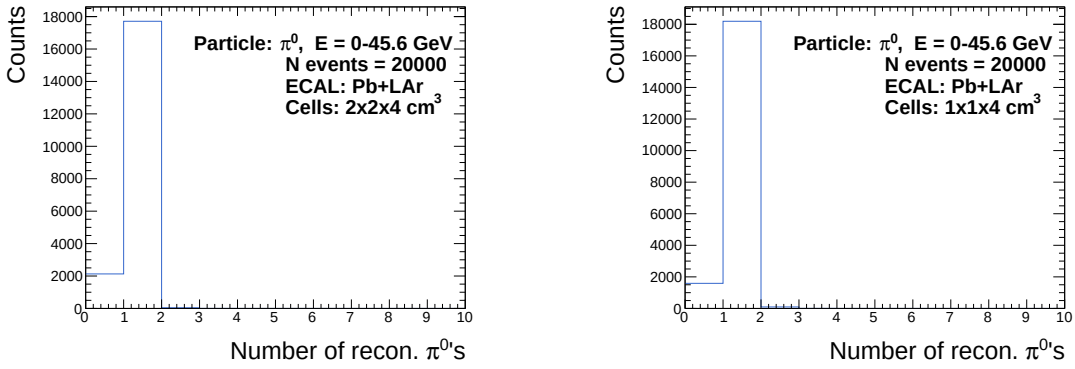

(a) For the initial LAr ECAL **(b)** For the revised LAr ECAL

Figure 10.6: The total number of reconstructed π^0's per event

of the one-cluster mass peaks at higher energies, the efficiency for the signal events decreases with higher energies whereas the probability of background accepted as π^0's increases with higher energies. The average probability of accepting a photon as a π^0 is 5.62% for the initial LAr ECAL and 2.48% for the revised ECAL, which is a substantial reduction. The higher granularity of the revised design allows more π^0's to be resolved in two clusters at lower energies and the better unresolved π^0/single photon separation reduces the amount of background accepted as π^0's. The tipping point for detecting more unresolved than resolved π^0's is $\sim$ 16 GeV for both cell structures.

The overall impression from this comparison is that the smaller cells of only $1 \times 1 \times 4$ cm^3 influence the precision of both the resolved and unresolved π^0 finding. The higher granularity improves the position resolution and resolves a larger fraction of π^0's into two clusters. The one-cluster mass distributions become narrower which enhances the separation of unresolved π^0's from the single photons. The latter reduces the number of fake π^0's significantly.
This knowledge can now be used for studying the effects of changing the absorber and active materials in the ECAL to LKr and tungsten.

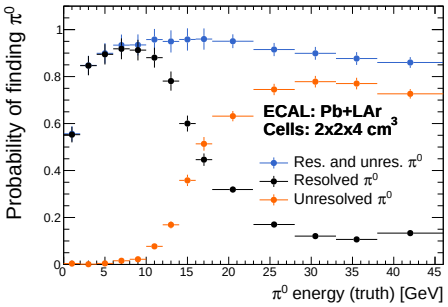

(a) The probability of reconstructing a π^0 in π^0 events for the initial LAr ECAL

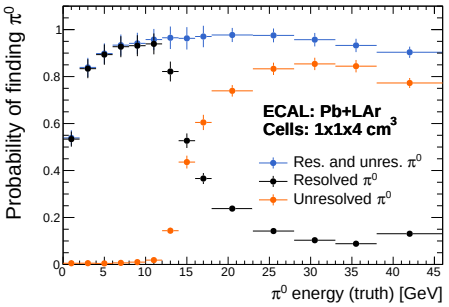

(b) The probability of reconstructing a π^0 in π^0 events for the revised LAr ECAL

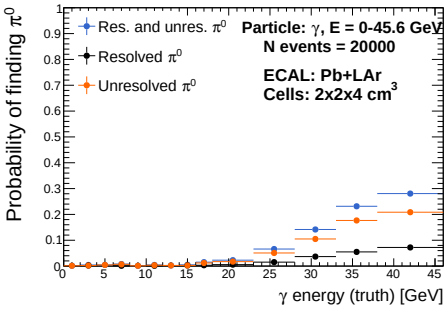

(c) The probability of reconstructing a π^0 in γ events for the initial LAr ECAL

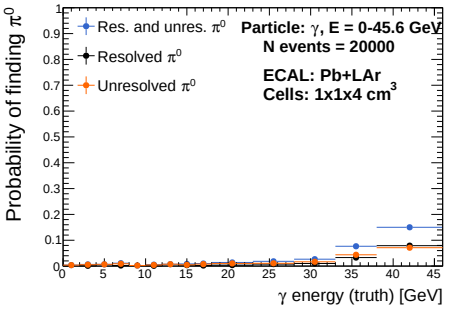

(d) The probability of reconstructing a π^0 in γ events for the revised LAr ECAL

Figure 10.7: The probability of reconstructing a π^0 in π^0 (top) and photon (bottom) events for both the initial and revised LAr ECAL

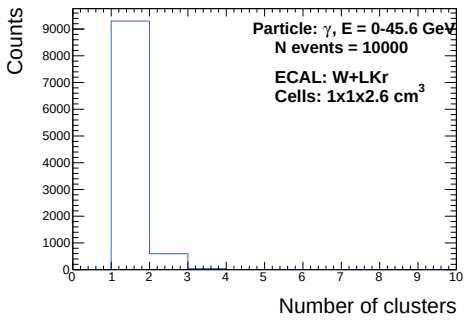

(a) Number of clusters per generated photon

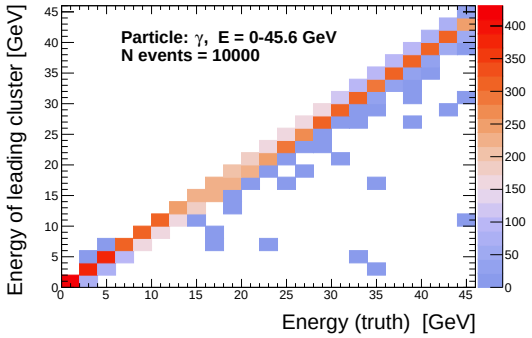

(b) Leading cluster energy vs. truth energy for photons before energy re-calibration

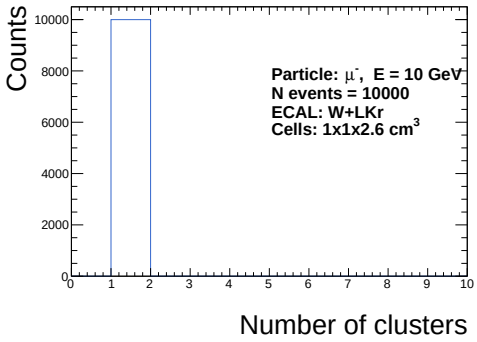

(c) Number of clusters per 10 GeV generated muon

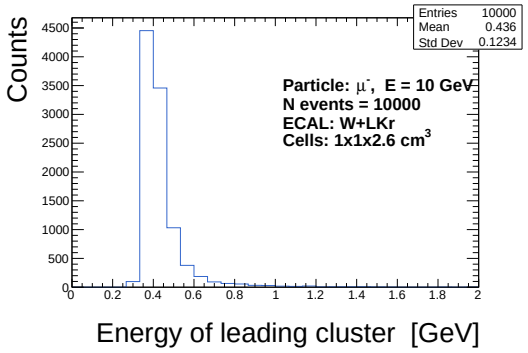

(d) Recorded energy of leading muon clusters

Figure 10.8: Photon (top) and muon (bottom) reconstruction in the LKr ECAL

10.2 A liquid krypton electromagentic calorimeter

The performance testing of the LKr ECAL is done analogously to the method presented in the previous section and its performance is compared to the revised LAr design.

It is first ensured that the clustering method is still valid for the LKr design. Figure 10.8 shows the number of reconstructed clusters above the reconstruction limit of 200 MeV for muons and photons along with their recorded energy. Figure 10.8a and 10.8c show that a cluster corresponds to a generated particle in most events for both particle species. The average number of fake clusters per photon is 0.06. This indicates that the clustering thresholds are still adequate. Figure 10.8b shows a comparison of the leading cluster energy (before the non-linear energy calibration) to

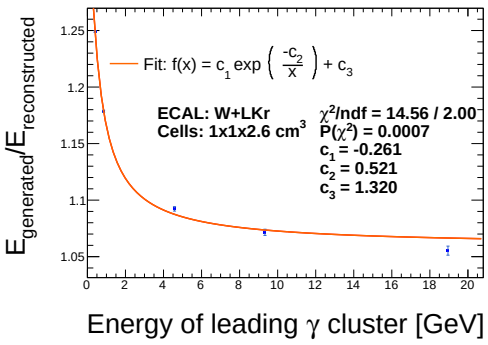

(a) The energy dependent calibration factor as a function of cluster energy

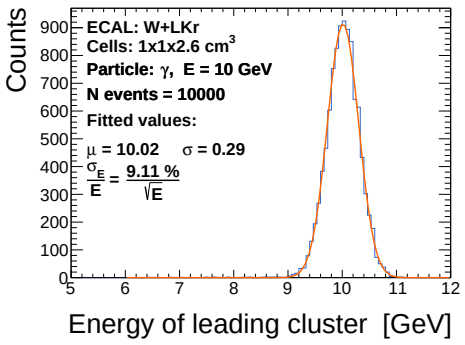

(b) The energy of 10 GeV leading photon clusters after calibration

Figure 10.9: Energy re-calibration of the LKr ECAL

the generated photon energy. It can be seen that the leading clusters in general will contain most of the initial energy of the photon. Figure 10.8d shows that the MIP energy is $E_{MIP} \sim 440$ MeV, which means that the reconstruction limit of should not dismiss MIP signals. The clustering therefore seems to reconstruct the particles as intended also for this design.

The calibration of the LKr ECAL is performed using the same methods as for the LAr ECAL. The energy is calibrated using a energy dependent correction, displayed in Figure 10.9a, which demonstrates that the calibration is most precise for lower energies as for the LAr ECAL. This calibration accounts for the inevitable energy loss of the clustering process. The energy distribution of the leading cluster of 10 GeV photons is shown in Figure 10.9b and shows an energy resolution of $\frac{\sigma_E}{E} = \frac{9.11\%}{\sqrt{E}}$. Compared to the revised LAr ECAL ($\frac{\sigma_E}{E} = \frac{8.91\%}{\sqrt{E}}$) this is a bit lower but still comparable. The resolution can however be adjusted by fine tuning the relative thickness of LKr to tungsten.

Figure 10.10a shows the $r\phi$ and z resolution before and after the s-curve correction. The s-curve correction mostly improves the resolution of higher energy photons. The position resolution of 10 GeV photons is improved from 0.93 mm to 0.76 mm in the $r\phi$ and z direction. The fits and detailed s-curve correction of the LKr ECAL and be found in Appendix F.
Figure 10.10b shows the resulting $r\phi$ and z resolution for the two ECALs. The fact that the LKr ECAL has better position resolution for the entire energy range suggests that the modest energy dispersion of the LKr ECAL materials allows for a more precise determination of the cluster position. This might lead to a better resolution of close-by photons and hence a larger fraction of resolved π^0s.

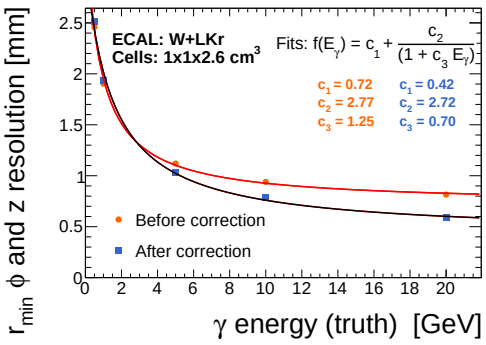

(a) The angular resolution before and after s-curve correction for the LKr ECAL

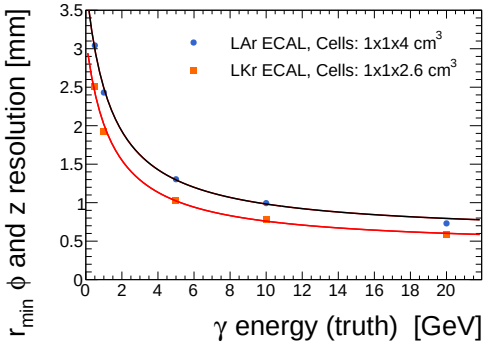

(b) The angular resolution of the revised LAr and LKr ECALs after s-curve correction

Figure 10.10: The effect of s-curve correction and total $r\phi$ and z resolution

The fraction of one- and two-cluster events for the π^0 samples is presented in Figure 10.11 for both ECALs (Figure 10.3d is re-printed for an easier comparison). It can be seen that the fraction of two-cluster events is lower for the LKr design, which is possibly due to the lower amount of fake clusters per generated photon.

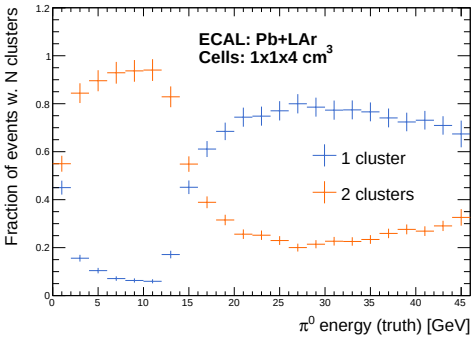

(a) For the revised LAr ECAL

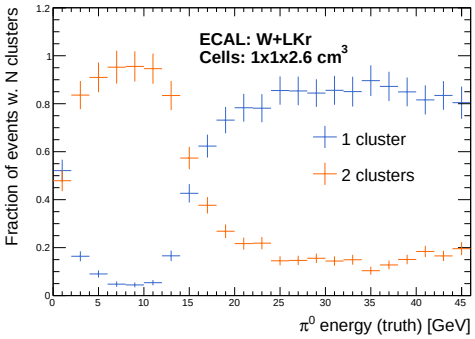

(b) For the LKr ECAL

Figure 10.11: The fraction of events with π^0 events with one or two clusters

Figure 10.12 shows the invariant mass in two-cluster events. It shows a narrow peak around the π^0 mass as well as a background distribution. The background is less significant compared to the revised LAr ECAL results (Figure 10.4b) due to the reduced amount of fake clusters. The standard deviation is 0.008 GeV which is smaller than the standard deviation of both the initial and revised LAr ECAL.

Turning to the one-cluster mass, the calculation of the mean minor axis demonstrates that $\mu(minor) = 0.0037$ rad for the LKr geometry. A comparison to the mean minor axis of the revised LAr ECAL ($\mu(minor) = 0.0043$ rad) supports the results from section 6.2.1, suggesting that the smaller Molière radius indeed give rise to narrower

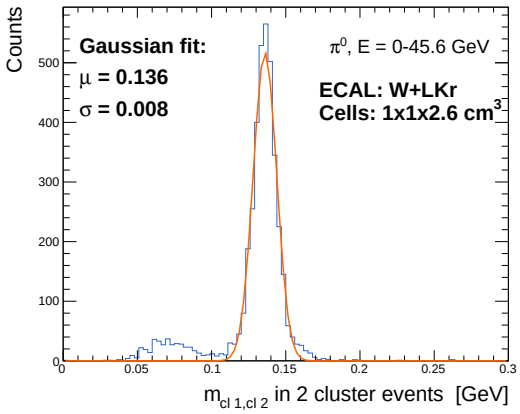

Figure 10.12: The invariant mass of two-cluster π^0 events

showers. The cluster mass of one-cluster events in the π^0 and the single photon samples can be seen in Figure 10.13. It shows narrower peaks for the LKr ECAL for both true single photons and unresolved π^0's. This is especially clear for energy ranges 25-35 GeV and $E > 35$ GeV and allows for a cleaner separation of the two. An almost ideal separation can be achieved up 35 GeV with a cut of $m_{clus} > 0.1$ GeV.

The π^0 identification for the LKr geometry requires a resolved π^0 to have an invariant mass of 103 MeV $< m_{cl1,\,cl2} <$ 167 MeV and an unresolved π^0 to have $m_{clus} > 0.1$ GeV. The total number of reconstructed π^0's can be in Figure 10.14 and shows that one π^0 is reconstructed in most events.

The overall probability of reconstructing a π^0 is displayed in Figure 10.15. Figure 10.15a and 10.15c show that probability for reconstructing a π^0 for a generated π^0 is very similar for the two designs but increases slightly to 91.17% for the LKr ECAL. The tipping point for observing more unresolved than resolved π^0's is also $\sim$ 16 GeV for the LKr ECAL. For the photon events, the probability of falsely accepting a photon as a π^0 is reduced significantly for the LKr ECAL to 1.09%. Due to the lower amount of fake clusters and the narrower resolved π^0 mass peak, the fraction of fake resolved π^0's is almost eliminated. The cleaner single photon and unresolved π^0 separation also reduces the probability of accepting background events as unresolved π^0's. The π^0 reconstruction efficiency for all three designs is summarized in Table 10.1.

Generally, the analysis of alternative ECAL designs show a significant improvement in the π^0 reconstruction efficiency for both signal and background samples when decreasing the cell size of the LAr ECAL from $2 \times 2 \times 4$ cm^3 to $1 \times 1 \times 4$ cm^3. The

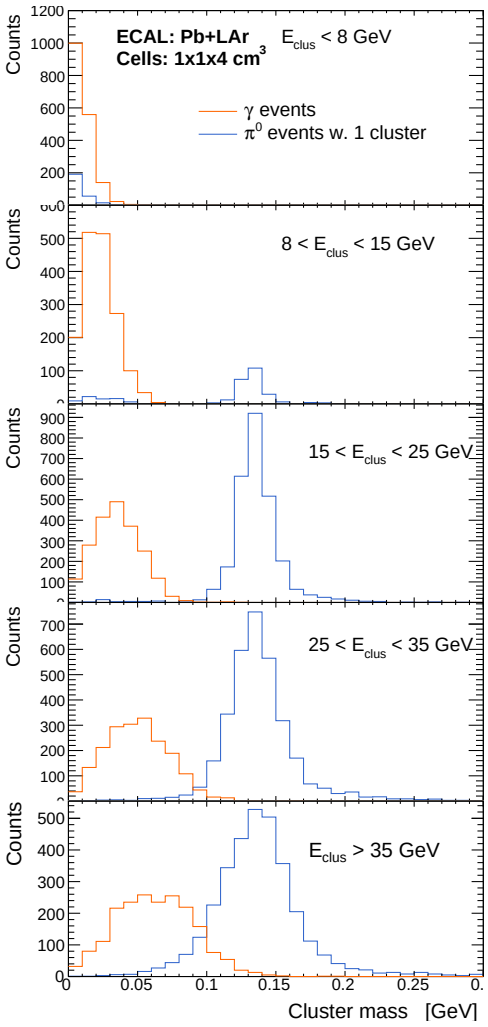

(a) For the revised LAr ECAL (20.000 events)

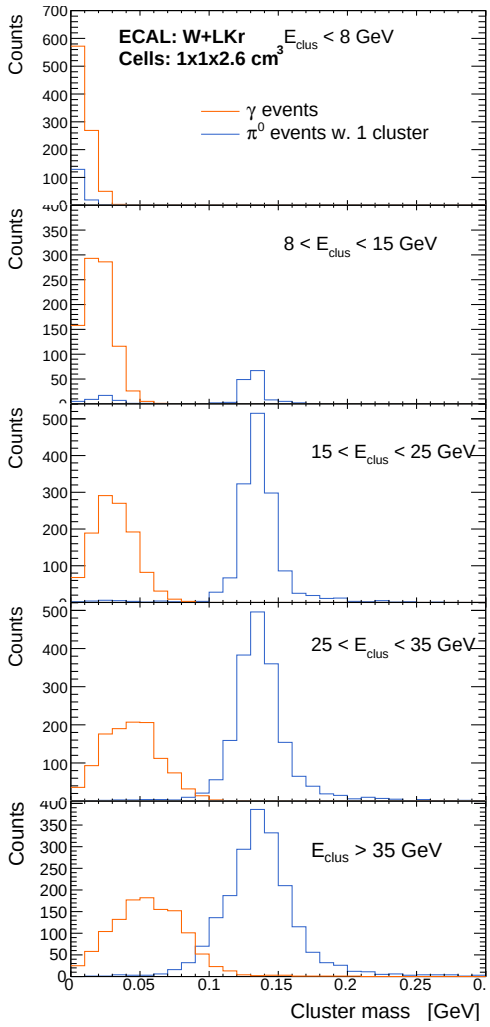

(b) For the LKr ECAL (10.000 events)

Figure 10.13: Cluster mass of single photons and one-cluster π^0 events

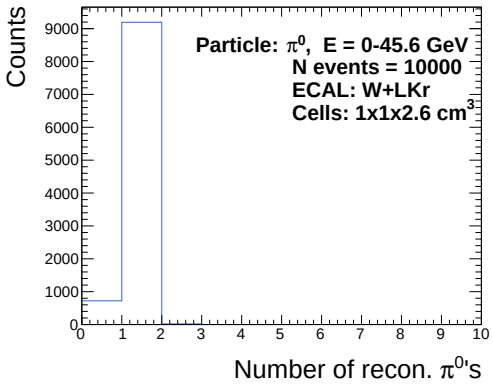

Figure 10.14: The total number of reconstructed π^0's per generated π^0 for the LKr geometry

ECAL	Efficiency	
	Signal	Background
Initial LAr ECAL	89.23%	5.62%
Revised LAr ECAL	91.09%	2.48%
LKr ECAL	91.17%	1.09%

Table 10.1: The π^0 reconstruction efficiency for the signal sample (π^0, E = 0-45.6 GeV) and background sample (γ, E = 0-45.6 GeV) for all three noble liquid ECAL designs

smaller cells also improves the position resolution. Choosing a LKr/W ECAL, results in more compact showers, due to the shorter Molière radius of the materials and improves the position resolution even further. This slightly enhances the overall probability of reconstructing a π^0, but it is mostly important for the quality of the separation of unresolved π^0's and single photons. The LKr and tungsten design seems well suited for reducing the number of photons falsely accepted π^0's and this noble liquid option therefore remains interesting.

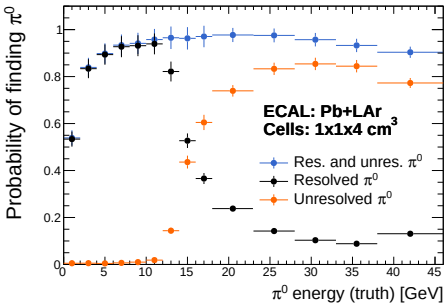

(a) The probability of reconstructing a π^0 in π^0 events for the revised LAr ECAL

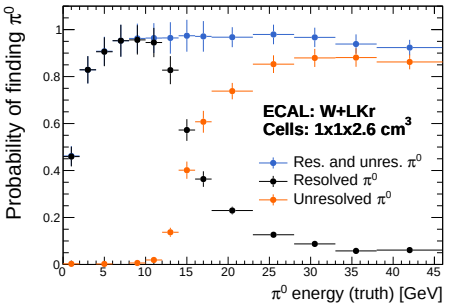

(b) The probability of reconstructing a π^0 in π^0 events for the LKr ECAL

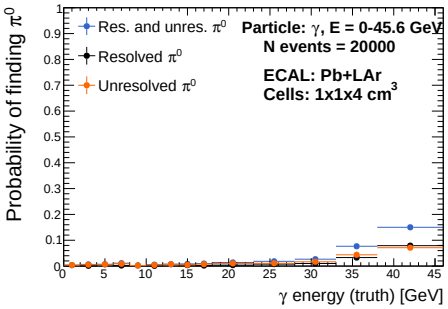

(c) The probability of reconstructing a π^0 in γ events for the revised LAr ECAL

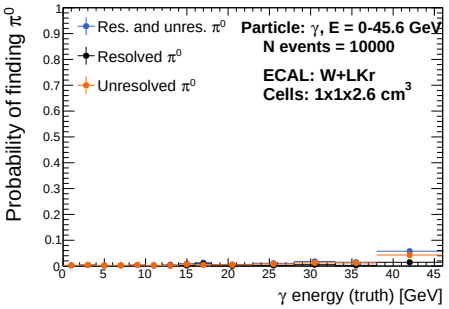

(d) The probability of reconstructing a π^0 in γ events for the LKr ECAL

Figure 10.15: The probability of reconstructing a π^0 in π^0 (top) and photon (bottom) events for both the revised LAr ECAL and the LKr ECAL

11 Conclusion

The extreme luminosities of the FCC-ee will produce 1.7×10^{11} $Z \to \tau^+\tau^-$ processes, which enables precision measurements of the τ polarisation. The measurements require a clean and well-understood separation of the τ decay channels. An inter-channel separation of the hadronic channels is especially important and relies heavily on a precise electromagnetic shower reconstruction from the calorimeters. A noble liquid sampling electromagnetic calorimeter (ECAL) consisting of layers of lead (Pb) and liquid argon (LAr) has been proposed as part of a potential calorimeter system. Its performance, based on the barrel geometry, has been studied in thesis. The calorimeter has a sampling fraction of 12.6%, corresponding to an energy resolution of $\frac{\sigma_E}{E} = \frac{7.75\%}{\sqrt{E}}$. The cell sizes of $2 \times 2 \times 4$ cm^3 establish a fine granularity, which is important when reconstructing π^0's due to the close-by daughter photons. The careful design of e.g. the electronics ensure a noise per read-out cell of 2-10 MeV at the EM scale and allows for reconstructions of low energy photons and minimum ionising particles (MIPs). The proposed design has a depth of $\sim 20X_0$ and a Molière radius of 41 mm.

Simulation studies have been performed by using both single particles and full $e^+e^- \to Z \to \tau^+\tau^-$ events at the Z peak. The shower reconstruction is achieved by a clustering algorithm. The design of this algorithm is essential since the later analysis relies upon proper particle reconstructions. The methods' success is demonstrated by the fact that it is able to reconstruct MIP signals as well as separating close-by photons. Having low (but realistic) clustering thresholds of $\text{thres}_{low} = 10$ GeV and $\text{thres}_{high} = 20$ GeV is highly important for enabling the reconstruction. The low noise levels allows for a low shower reconstruction limit of $E_{clus} > 200$ MeV and the modest, but inevitable, energy loss results in an energy resolution of $\frac{\sigma_E}{E} = \frac{8.3\%}{\sqrt{E}}$ after the clustering. The spatial resolution of the ECAL is improved by an s-curve correction from 1.95 mm to 1.28 mm in both the $r\phi$ and z direction for 10 GeV photons.

Hadronic interactions in the detector give rise to satellite clusters, also called fake photons. These clusters are a priori easily confused with single photons and a dedicated algorithm with the goal of separating the two neutral clusters has been

implemented. It successfully suppresses the number of fake photons per charged pion by approximately a factor 26 from 0.9 to 0.035 fake photons per π^+, while preserving 95.8% of the 1 GeV photon signal.

The observed π^0's are divided into two sub-categories: resolved and unresolved π^0's. For resolved π^0's, the two daughter photons are reconstructed separately in two clusters whereas they have merged into one bigger cluster for the unresolved π^0's. The resolved π^0's dominate at energies below $E_{\pi^0} < 16$ GeV. Above this point more π^0's become unresolved due to the increasingly smaller photon opening angle. Each π^0 type has a specific reconstruction scheme. The resolved π^0's are identified by combining the observed photons in pairs. The invariant mass of the pairs is then calculated, and if it is consistent with the true π^0 mass, the photon pair is accepted as a π^0. The efficiency of the resolved π^0 finding below $E < 16$ GeV is $\epsilon_{res\,\pi^0} > 98\%$.

The unresolved π^0's are identified by exploiting their wider transverse profile compared to single photon clusters. The transverse profile properties facilitate a calculation of the cluster invariant mass, which for the unresolved π^0's is observed to be consistent with the π^0 mass. This unresolved π^0/single photon identification has an efficiency of $82 - 90\%$ for $E > 16$ GeV, with the efficiency decreasing with increasing energy. The overall probability of reconstructing a π^0 is 83.9% which is competitive with ALEPH results, achieving a probability of $\sim 84\%$. Contrary to this analysis, the ALEPH results also include residual single photons, which are resolved π^0's where the partner photon is not observed due to e.g. low energy. This indicates a satisfactory performance of the LAr ECAL. The probability of falsely accepting a photon as a π^0 is 4.4% and is mostly dominated by high energy photons, which are rare in τ decays.

The ECAL performance is further investigated with the formation of the hadronic migration matrix. The migration matrix has dominant diagonal elements which indicates a successful classification. For the $\tau \to \pi^{\pm}\nu$ and $\tau \to \pi^{\pm}\pi^0\nu$ channels the fraction of correctly classified decays are 95.6% and 90.2%, respectively. The results are compatible with former ALEPH measurements. However, due to the unfortunate improbable kinematics of the simulated τ decays in this thesis (see section 6.1), these results might change slightly when correcting the data. Nonetheless, the results indicate that the ECAL design is suitable for achieving a relatively clean and well-understood separation of the decay channels. To further increase the precision of the inter-channel separation, it is necessary to develop an improved radiation photon identification method as well as providing a suitable solution for tackling events with merged $\pi^{\pm}$ and π^0 clusters.

A simplified analysis compares the π^0 reconstruction efficiency of the initial LAr ECAL with cell size $2 \times 2 \times 4$ cm^3 to a revised LAr ECAL with cell size $1 \times 1 \times 4$ cm^3. The results of the revised LAr ECAL analysis are subsequently compared to a liquid krypton (LKr) and tungsten (W) ECAL design with cell sizes $1 \times 1 \times 2.6$ cm^3. Due to the replacement of LAr/Pb with LKr/W, the Molière radius of this ECAL is only 27 mm. Increasing the granularity of the LAr design by choosing smaller cell sizes increases the position resolution in $r\phi$ and z for 10 GeV photon from 1.28 mm of the initial LAr ECAL to 0.98 mm for the revised LAr ECAL. For the LKr design the position resolution becomes 0.76 mm for 10 GeV photons. The energy resolution is similar between the designs.
The comparison of the initial and revised LAr calorimeters suggests that the smaller cell sizes resolves a larger fraction of π^0's in two clusters. The higher granularity furthermore results in a significantly better unresolved π^0 and single photon separation and thereby lowers the amount of photons accepted as π^0's. The consequence of the decreasing the cell size is that the smaller cells are more sensitive to energy fluctuations within the electromagnetic showers, which can divide one shower into several clusters. This does however not seem to affect the overall π^0 reconstruction efficiency. The overall efficiency for reconstructing a π^0 improves from 89.2% for the initial LAr (a re-calculated value using the same simple analysis method as for the other designs for an apples-to-apples comparison) to 91.1% for the revised design. The amount of background accepted as π^0's decreases from 5.6% to 2.5% with the smaller cells.

Replacing the lead and LAr with tungsten and LKr enhances the precision of both the resolved and unresolved π^0 finding. The overall probability of reconstructing a π^0 increases slightly to 91.2% and the efficiency for the background is substantially reduced to 1.1%. The probability of accepting fake resolved π^0's is almost eliminated with this design. The comparison of the three designs suggests that a higher precision in the π^0 reconstruction can possibly be achieved by decreasing the cell sizes of the LAr ECAL. The LKr design indicates a high suppression of fake π^0's and an improved position resolution, which shows great promise for this technology.

In general, this study shows that a LAr and lead sampling electromagnetic calorimeter of the proposed geometry looks promising for achieving a τ decay mode identification. Especially the good energy resolution, low noise levels and high granularity are important features of the detector. Additionally, an exact and sophisticated clustering algorithm is a necessity for maintaining the precision in the later analysis

as well as having a precise π^0 reconstruction scheme. Further investigations should be conducted to determine the optimal design and adjusting the cell size of the proposed LAr ECAL or investigating an alternative LKr and tungsten design is particularly interesting.

Bibliography

[1] FCC Collaboration, „FCC physics opportunities: Future circular collider conceptual design report volume 1“, *The European Physical Journal C*, pp. 15–31, Jun. 2019. DOI: 10.1140/epjc/s10052-019-6904-3. [Online]. Available: http://link.springer.com/10.1140/epjc/s10052-019-6904-3.

[2] FCC Collaboration, „FCC-ee: The lepton collider: Future circular collider conceptual design report volume 2“, *The European Physical Journal Special Topics*, pp. 290–324, 437–443, 504–513, Jun. 2019. DOI: 10.1140/epjst/e2019-900045-4. [Online]. Available: http://link.springer.com/10.1140/epjst/e2019-900045-4.

[3] M. Aleksa, F. Bedeschi, R. Ferrari, F. Sefkow, and C. G. Tully, „Calorimetry at FCC-ee“, pp. 4–7, Sep. 1, 2021. arXiv: 2109.00391. [Online]. Available: http://arxiv.org/abs/2109.00391.

[4] ATLAS Collaboration, „Observation of a new particle in the search for the standard model higgs boson with the ATLAS detector at the LHC“, *Physics Letters B 716.1*, 2012. DOI: 10.1016/j.physletb.2012.08.020.

[5] CMS Collaboration, „Observation of a new boson at a mass of 125 GeV with the CMS experiment at the LHC“, *Physics Letters B 716.1*, 2012. DOI: 10.1016/j.physletb.2012.08.021.

[6] M. Dam, „The τ challenge at FCC-ee“, Jul. 27, 2021, version: 1. [Online]. Available: http://arxiv.org/abs/2107.12832 (visited on 11/26/2021).

[7] Wikipedia. (2019). Standard model of elementary particles, [Online]. Available: https://commons.wikimedia.org/wiki/File:Standard_Model_of_Elementary_Particles.svg (visited on 11/26/2021).

[8] E. Richard. (2007). Elementary particle interactions, [Online]. Available: https://commons.wikimedia.org/wiki/File:Elementary_particle_interactions.svg (visited on 11/26/2021).

[9] M. A. Thomson, „Modern particle physics“, 2013, pp. 1–112, 207–327, 408–510.

[10] P. W. Higgs, „Broken symmetries and the masses of gauge bosons“, 1964. DOI: 10.1103/PhysRevLett.13.508. [Online]. Available: https://link.aps.org/doi/10.1103/PhysRevLett.13.508.

[11] M. D. Schwartz, „Quantum Field Theory and the Standard Model“, pp. 29–32, 157–192, 575–579, 587–588, 2014.

[12] M. McCullough, „An indirect model-dependent probe of the higgs self-coupling“, *Phys. Rev. D 90, 015001*, 2013. DOI: 10.1103/PhysRevD.90.015001.

[13] G. Bertone, D. Hooper, and J. Silk, „Particle dark matter: Evidence, candidates and constraints“, *Physics Reports*, no. 5, Jan. 2005, version: 2. DOI: 10.1016/j.physrep.2004.08.031. [Online]. Available: http://arxiv.org/abs/hep-ph/0404175.

[14] A. Lowe, „Neutrino physics the solar neutrino problem“, 2009. [Online]. Available: https://arxiv.org/pdf/0907.3658.pdf.

[15] M. C. Gonzalez-Garcia and M. Maltoni, „Phenomenology with massive neutrinos“, *Physics Reports*, Apr. 2008. DOI: 10.1016/j.physrep.2007.12.004. arXiv: 0704.1800. [Online]. Available: http://arxiv.org/abs/0704.1800.

[16] F. Spano', „Standard model electroweak measurements at LEP“, May 19, 2006. arXiv: hep-ex/0605093. [Online]. Available: http://arxiv.org/abs/hep-ex/0605093 (visited on 11/26/2021).

[17] M. L. Perl et al., „Evidence for anomalous lepton production in e+ e- annihilation“, *Physical Review Letters. 35 (22): 1489.*, 1975. DOI: 10.1103/PhysRevLett.35.1489.

[18] P. A. Zyla et al.. (2021). Particle data group, [Online]. Available: https://pdg.lbl.gov/2021/tables/contents_tables.html (visited on 10/18/2021).

[19] M. Dam, „Tests of the electroweak theory with the delphi detector at lep“, *PhD thesis, Departments of Physics, University of Oslo*, pp. 20–24, 1995.

[20] ALEPH Collaboration, „Measurement of the tau polarisation at LEP“, *The European Physical Journal C*, May 2001. DOI: 10.1007/s100520100689. [Online]. Available: http://arxiv.org/abs/hep-ex/0104038.

[21] ALEPH Collaboration, „Measurement of the tau polarisation at the z resonance“, *Z. Phys. C 59, 369-386*, vol. 59, 1993. DOI: 10.1007/BF01498618. [Online]. Available: http://link.springer.com/10.1007/BF01498618.

[22] ALEPH Collaboration, „Branching ratios and spectral functions of tau decays: Final ALEPH measurements and physics implications“, *Physics Reports*, 2005. DOI: 10.1016/j.physrep.2005.06.007.

[23] J. J. D. Miller D.R. Tovey. (2000 - reviewed 2019). Kinematics, [Online]. Available: https://pdg.lbl.gov/2019/reviews/rpp2018-rev-kinematics.pdf.

[24] D. E. Groom and S. R. Klein, „Passage of particles through matter“, *The European Physical Journal C*, Mar. 2000. DOI: 10.1007/BF02683419. [Online]. Available: http://link.springer.com/10.1007/BF02683419.

[25] J. E. Brau, J. A. Jaros, and H. Ma, „Advances in calorimetry“, *Annual Review of Nuclear and Particle Science*, no. 1, 2010. DOI: 10.1146/annurev.nucl.012809.104449. [Online]. Available: https://doi.org/10.1146/annurev.nucl.012809.104449.

[26] P. Hansen, „Particle detectors and accelerators lecture notes“, *University of Copenhagen*, vol. 3rd ed. Pp. 69–111, 2016.

[27] F. Brieuc. (2020). R&d on noble liquid calorimetry for FCC, [Online]. Available: https://indico.cern.ch/event/932973/contributions/4062113/attachments/2140558/3607661/20201111_LArCaloRD_FCCweek.pdf.

[28] R. Chiche, D. Fournier, and N. Morange. (2020). Exploring FCC EMB geometry with matlab, [Online]. Available: https://indico.cern.ch/event/985994/contributions/4153095/attachments/2162942/3653083/Exploring%20FCC%20EMB%20Geometry.pdf.

[29] C. Bierlich, N. Desai, and L. e. a. Gellersen. (). PYTHIA 8.3 - PYTHIA 8.3, [Online]. Available: https://pythia.org/.

[30] V. Volkl et al. (2020). FCC Software, [Online]. Available: https://hep-fcc.github.io/fcc-tutorials/software-basics/fccsw.html.

[31] S. Agostinelli, J. Allison, K. Amako et al., „Geant4 — a simulation toolkit“, 2003. DOI: 10.1016/S0168-9002(03)01368-8. [Online]. Available: https://geant4.web.cern.ch/node/1.

[32] Particle Data Group. (2014). Atomic and nuclear properties of materials for more than 300 materials, [Online]. Available: https://pdg.lbl.gov/2014/AtomicNuclearProperties/ (visited on 08/12/2021).

[33] M. Rovere, Z. Chen, A. Di Pilato, F. Pantaleo, and C. Seez, „CLUE: A fast parallel clustering algorithm for high granularity calorimeters in high energy physics“, Jan. 27, 2020. [Online]. Available: http://arxiv.org/abs/2001.09761.

[34] F. Wang, D. Han, Y. Wang et al., „Improving the spatial resolution of nica/mpd ecal with new reconstruction methods“, pp. 4–6, 2019. DOI: 10.1088/1748-0221/14/05/P05010. [Online]. Available: https://arxiv.org/abs/1902.03629.

[35] W. R. Leo, „Techniques for nuclear and particle physics experiments“, pp. 19–20, 37–44, 1994.

[36] G. James, D. Witten, T. Hastie, and R. Tibshirani, „An introduction to statistical learning“, pp. 228–236, 374–385, 2013.

[37] ALEPH Collaboration, „Tau hadronic branching ratios“, *Z. Phys. C 70, 579–608*, 1996. DOI: 10.1007/s002880050134. [Online]. Available: https://link.springer.com/article/10.1007/s002880050134.

Appendices

Appendix A Clustering

This appendix concerns the clustering method presented in chapter 7. Appendix A.1 expands on the energy re-calibration of the clusters, whereas Appendix A.2 shows the s-curve correction.

Appendix A.1 Energy re-calibration

Figure A.1 shows the energy of the leading clusters of electrons and photons before and after the energy re-calibration is performed. It can be seen that the calibration indeed re-centers the cluster energy around the initial energy of the particle for both particle species.

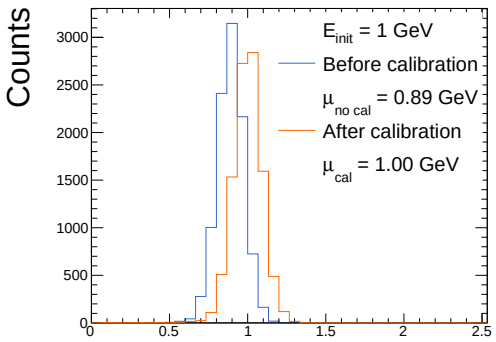

(a) Energy of leading 1 GeV photon clusters before and after the energy re-calibration

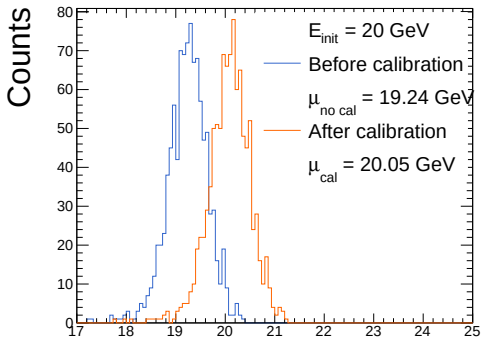

(b) Energy of leading 20 GeV photon clusters before and after the energy re-calibration

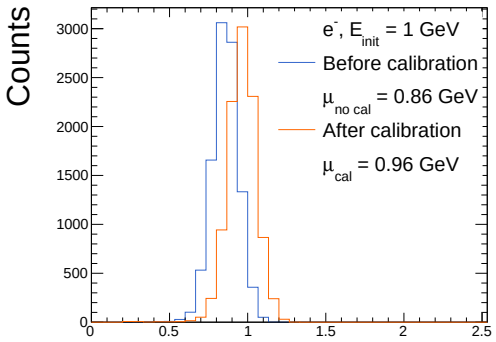

(c) Energy of leading 1 GeV electron clusters before and after the energy re-calibration

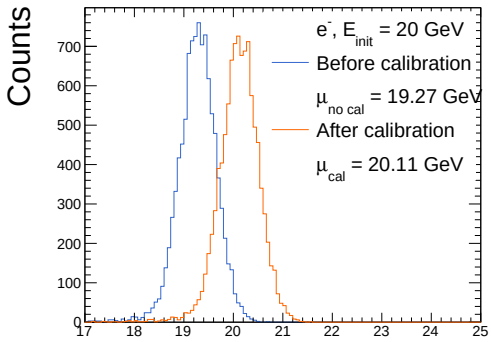

(d) Energy of leading 20 GeV electron clusters before and after the energy re-calibration

Figure A.1: The effect of energy re-calibration for photons (top) and electrons (bottom)

Appendix A.2 s-curve correction

Figure A.2 shows a fit to coordinate difference (in ϕ and z) between the position of the cluster and truth position as a function of the cluster position for $0 - 45.6$ GeV photons. It can be seen that the s-curve can be described by a sine function. The fit is used as a correction and Figure A.3 shows the angular resolutions in the $\phi-$ and z-coordinates before and after this correction has been applied for different photon energies. It can be seen that the double-peak structures are successfully eliminated by the correction and the position resolution is improved for all energies.

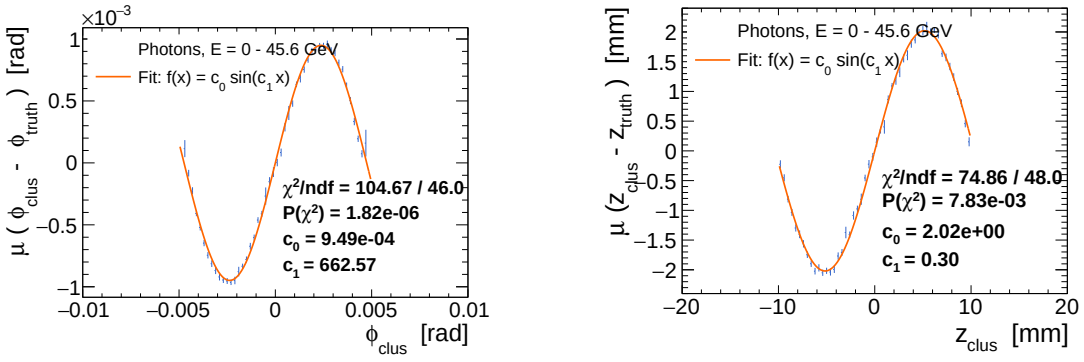

(a) ϕ coordinate **(b)** z coordinate

Figure A.2: Difference in coordinate (ϕ and z) between generated particle and reconstructed cluster versus reconstructed coordinate within one cell width fitted with a sine function

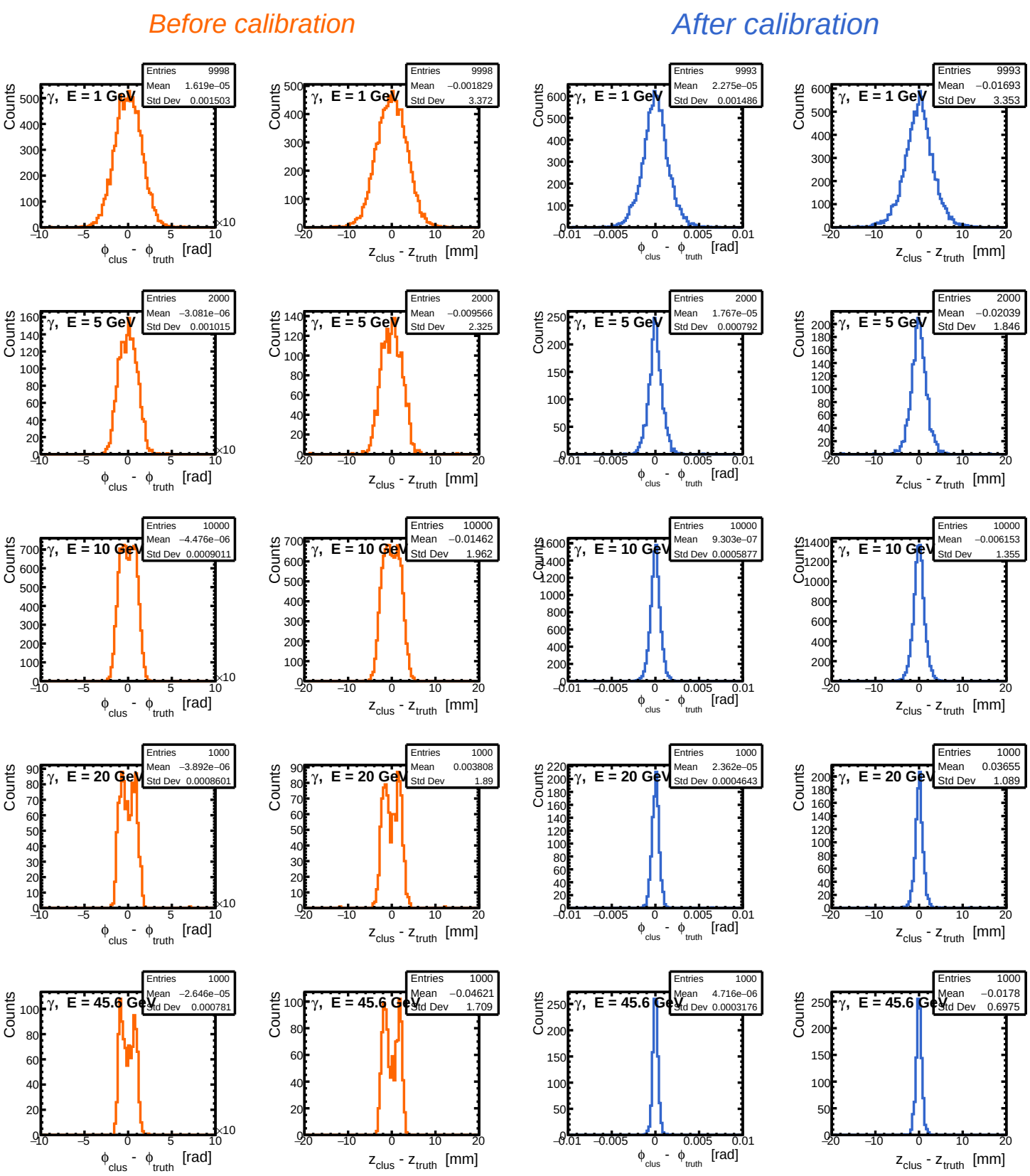

Figure A.3: The angular resolutions before and after the s-curve correction is applied for different photon energies

Appendix B $e^-/\pi^\pm$ separation

This appendix expands on the separation variables used for the electron identification. Figure B.1 shows the energy dependencies of the limits for different separation variables used in the $e^-/\pi^\pm$ separation. For all variables, the limits decrease with rising particle energy.

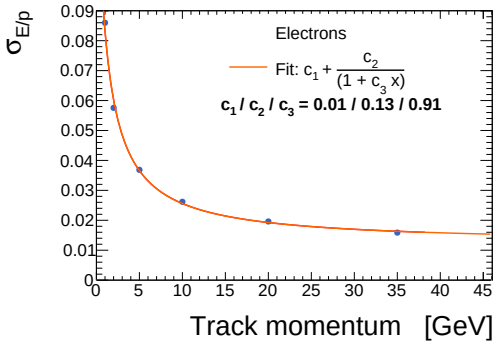

(a) Energy dependence of the standard deviation of the E/p value for electrons

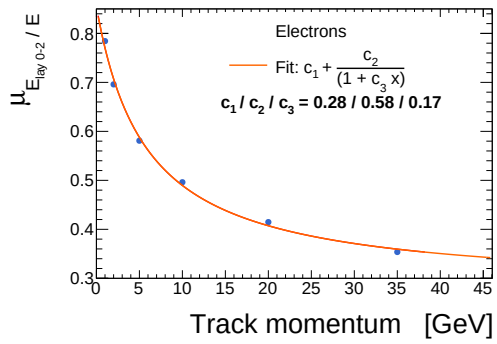

(b) Energy dependence of the mean energy fraction deposited in layers 0-3 for electrons

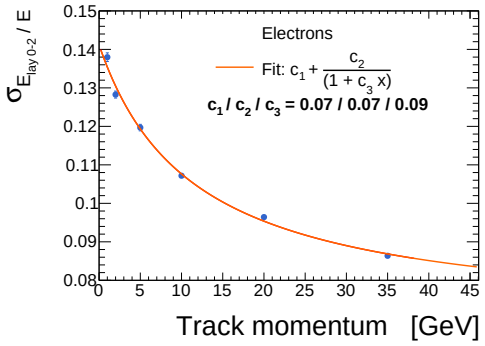

(c) Energy dependence of the standard deviation of the energy fraction deposited in layers 0-3 for electrons

Figure B.1: The energy dependence of different separation variables used in the electron identification scheme

Figures B.2 to B.4 presents the distributions of the separation variables following each cut for both signal and background samples. The signal plots contain associated clusters of 20 GeV electrons and the backgrounds plots contain associated clusters 20 GeV π^+ and π^- samples. The figures show a reduction of background events with each cut while preserving most the signal events.

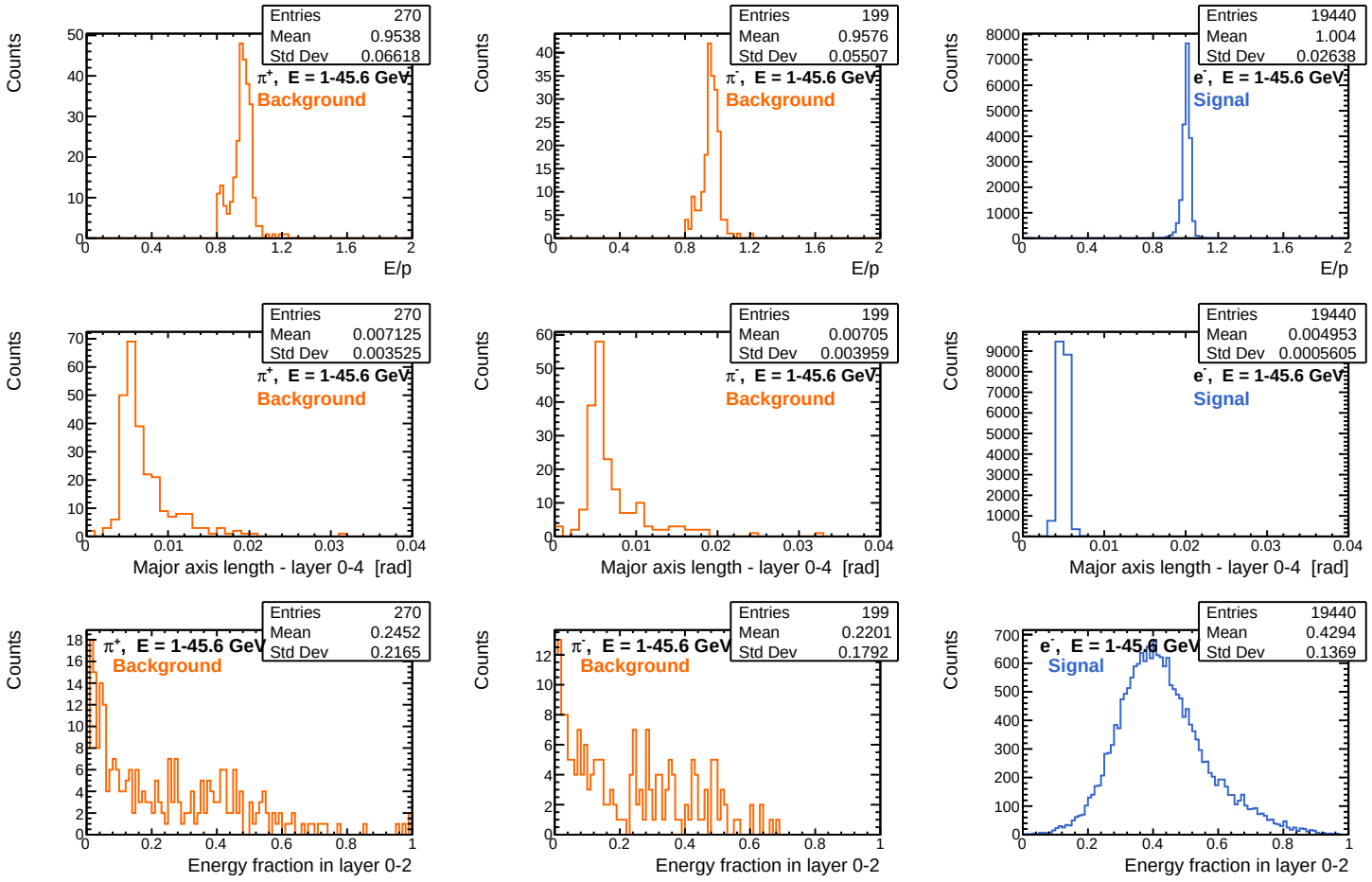

Figure B.2: Distributions of the cutting variables for electron identification for both background and signal samples after applying the cut $1-4\sigma_{E/p} < E/p < 1+4\sigma_{E/p}$ with the lower limit of $E/p > 0.8$

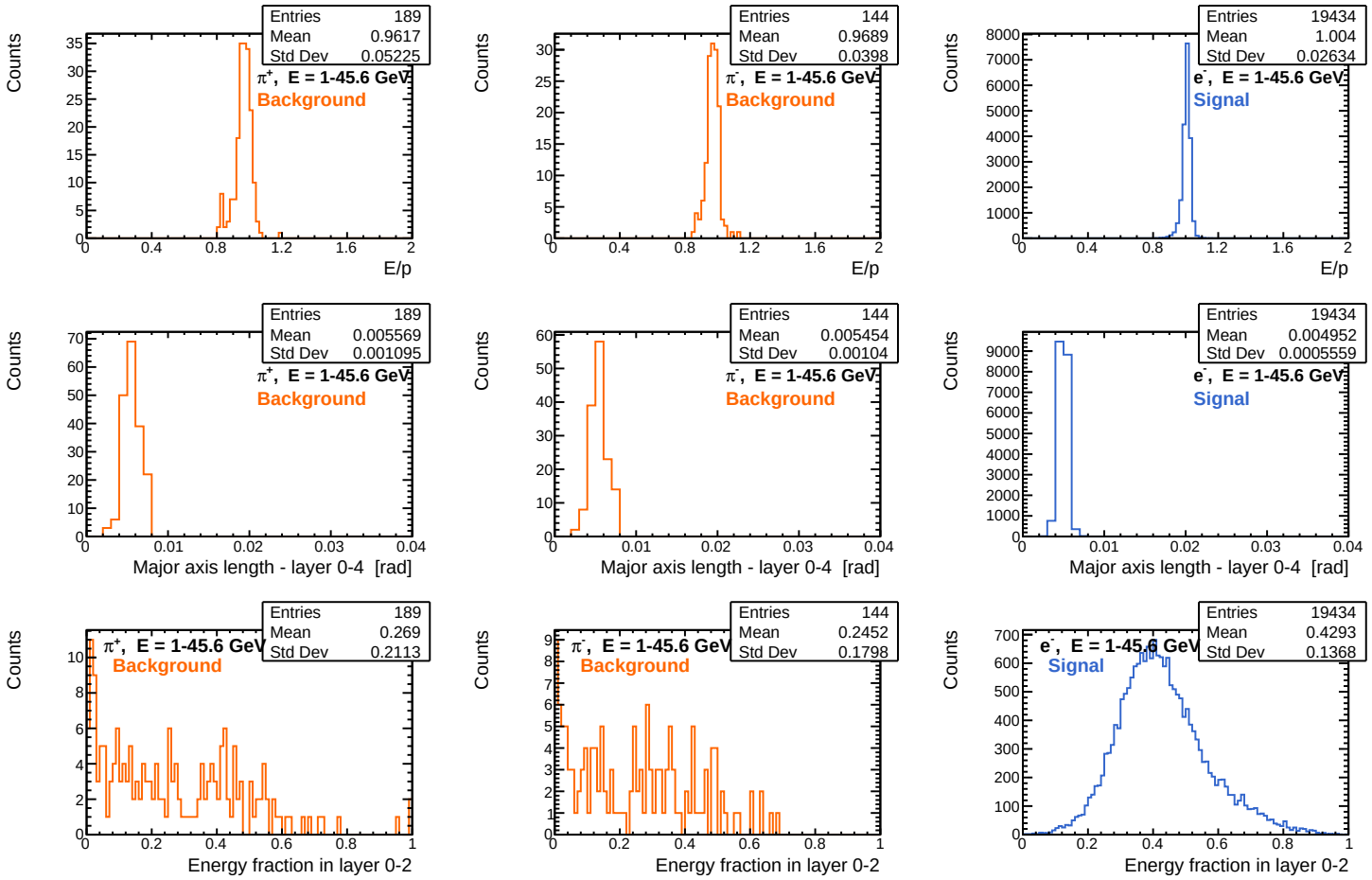

Figure B.3: Distributions of cutting variables for electron identification for both background and signal samples after applying the cut $0.002 \text{ rad} < major < 0.008 \text{ rad}$

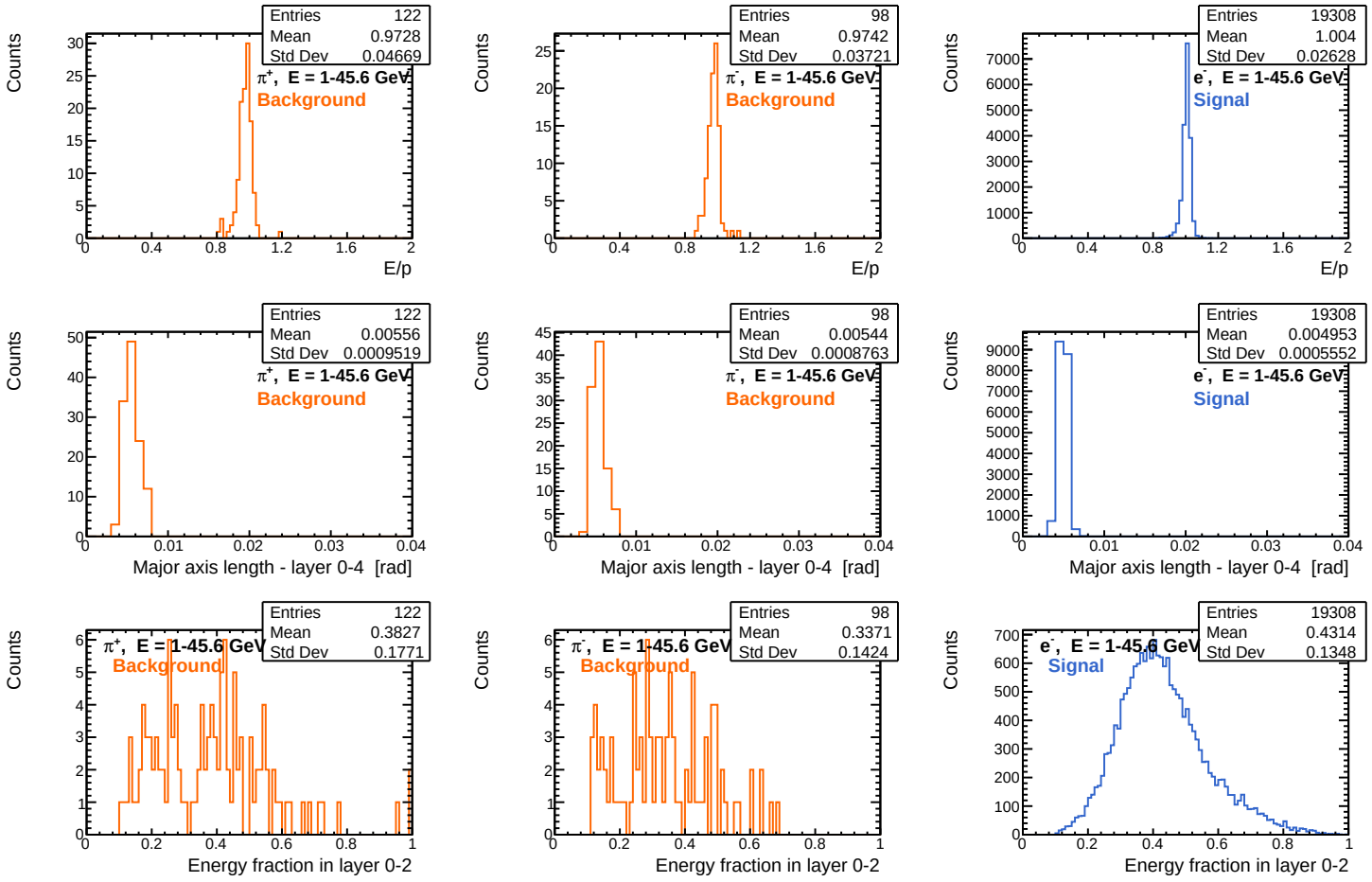

Figure B.4: Distributions of cutting variables for electron identification for both background and signal samples after applying cut $E_{lay} > \mu_{E_{lay}} - 3\sigma_{E_{lay}}$ with $E_{lay} = E_{layer\,0-3}/E$

Appendix C Fake photon killing

This appendix presents the distributions of the separation variables used for the FPK following each cut. They are displayed in Figures C.1 to C.5 for both signal and background samples. The signal is two single photon samples and the leading cluster is chosen as the genuine photon. The samples have energies $E = 0.5$ GeV and $E = 1$ GeV. The background is all non-associated clusters from a 20 GeV π^+ sample. It can be seen that the number of background events is significantly reduced with each cut while preserving most signal events.

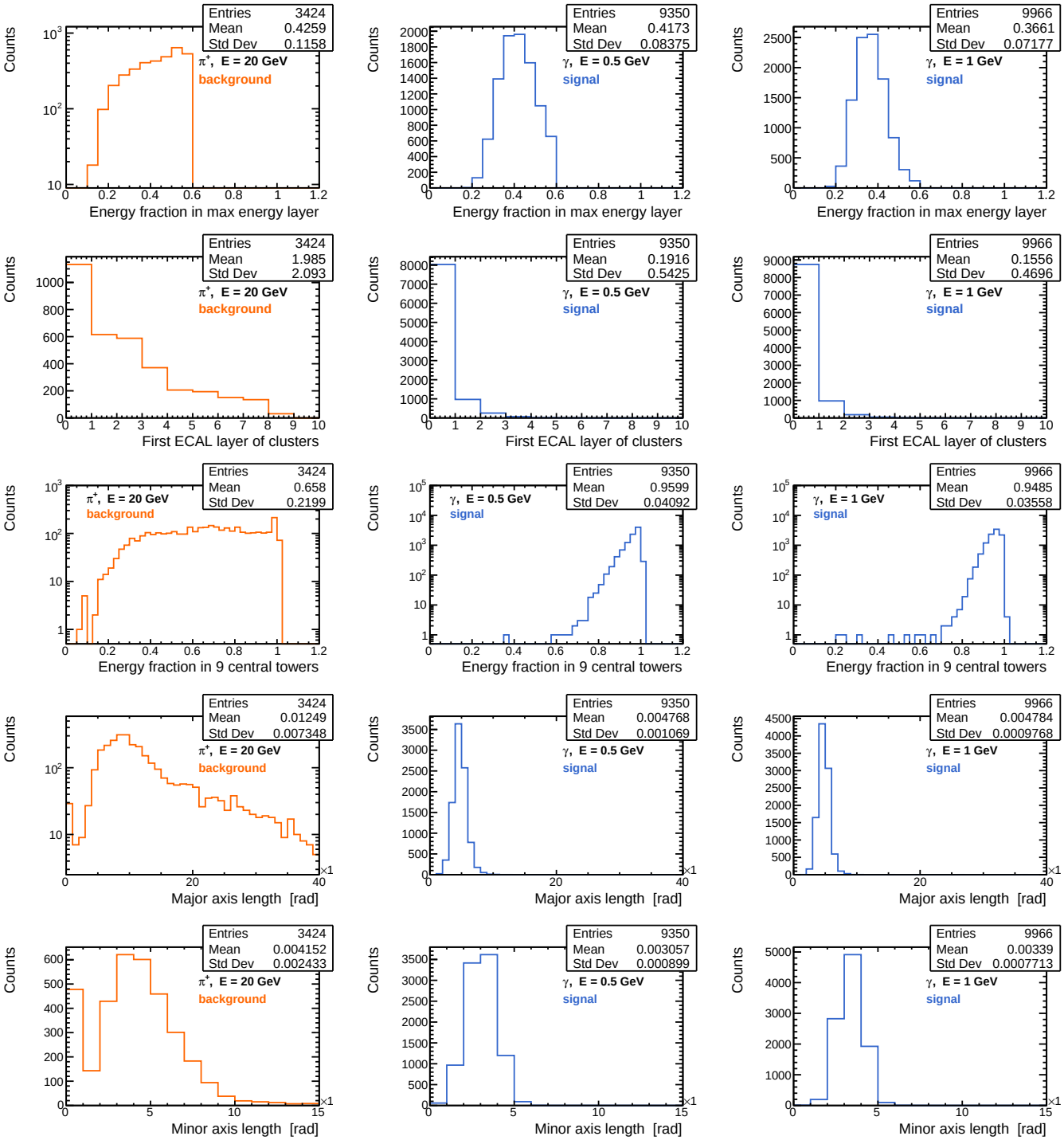

Figure C.1: Distributions of cutting variables for FPK for both background and signal samples after cut $E_{lay}/E \leq 0.6$.

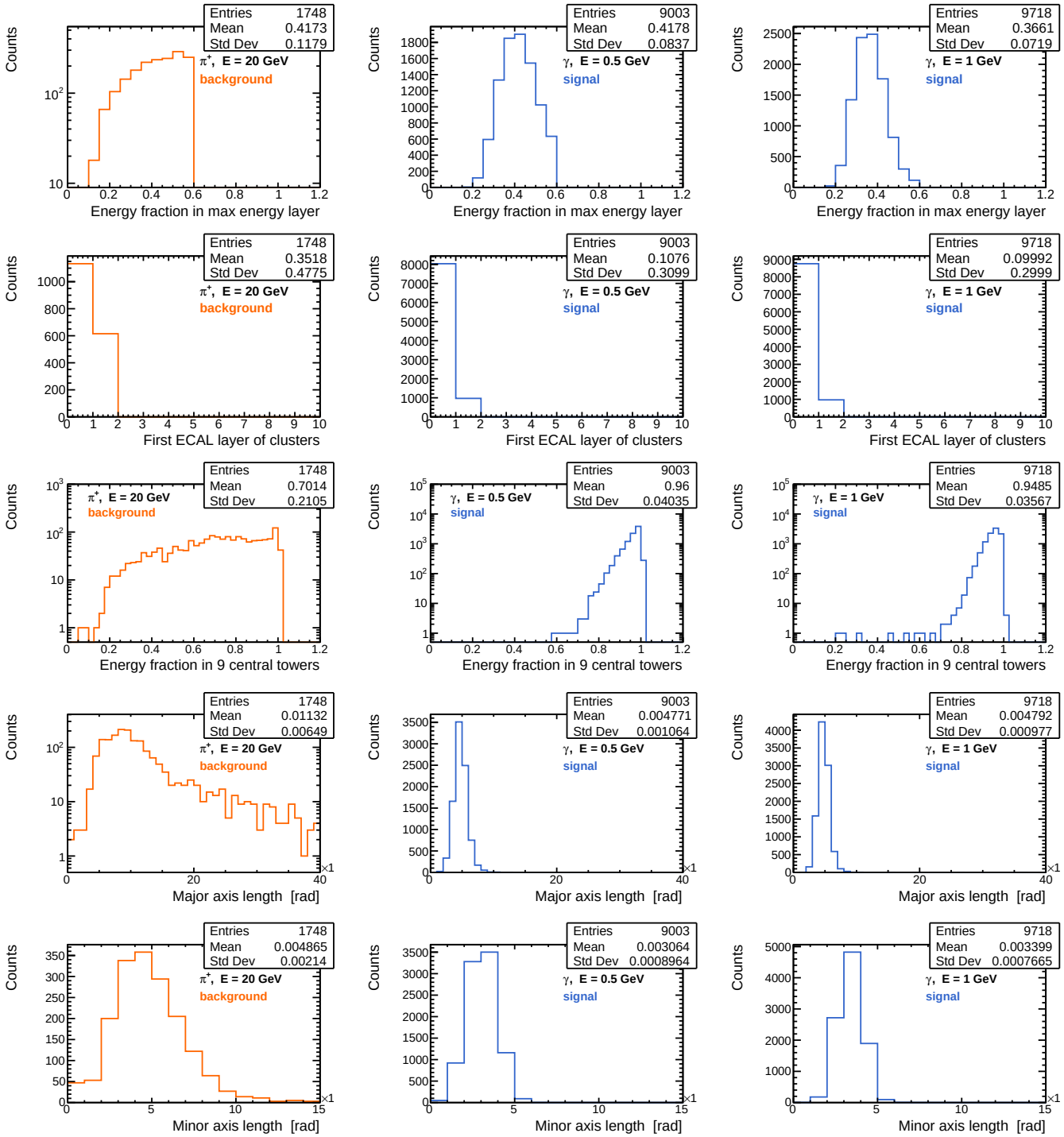

Figure C.2: Distributions of cutting variables for FPK for both background and signal samples after applying cut $Lay_{start} < 2$.

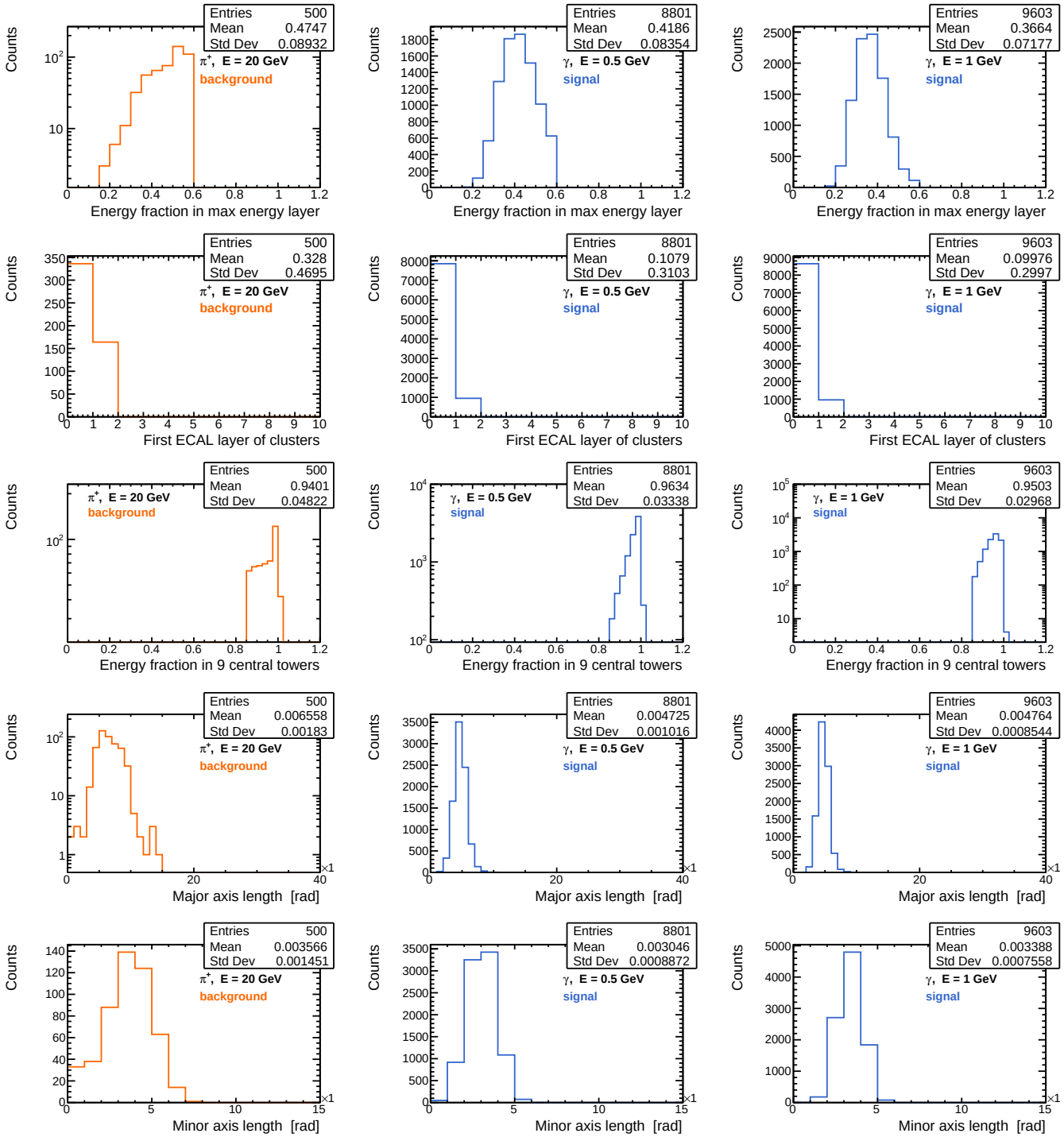

Figure C.3: Distributions of cutting variables for FPK for both background and signal samples after applying cut $E_{9\,towers}/E \geq 0.85$.

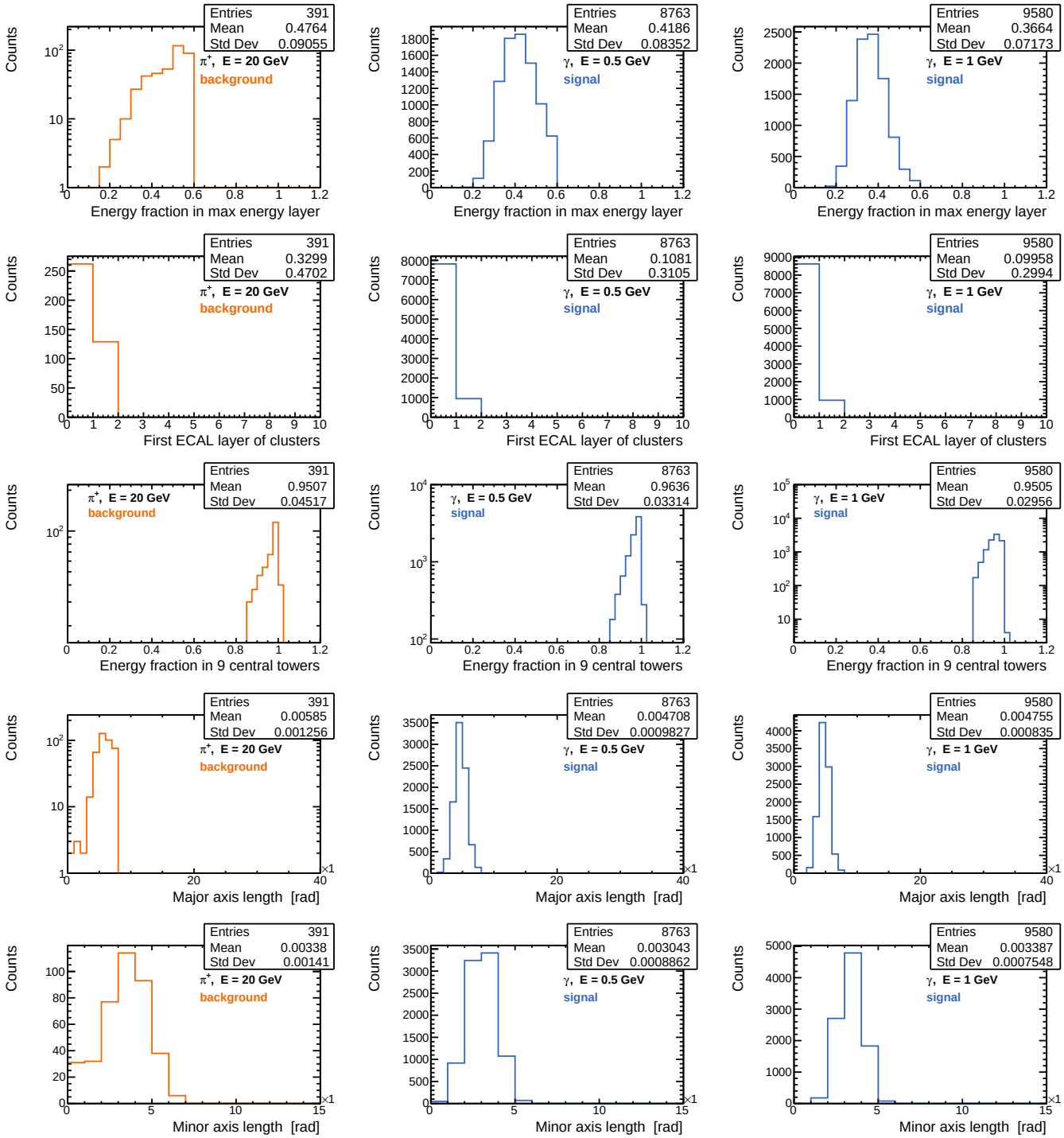

Figure C.4: Distributions of cutting variables for FPK for both background and signal samples after applying cut $major \leq 0.009$.

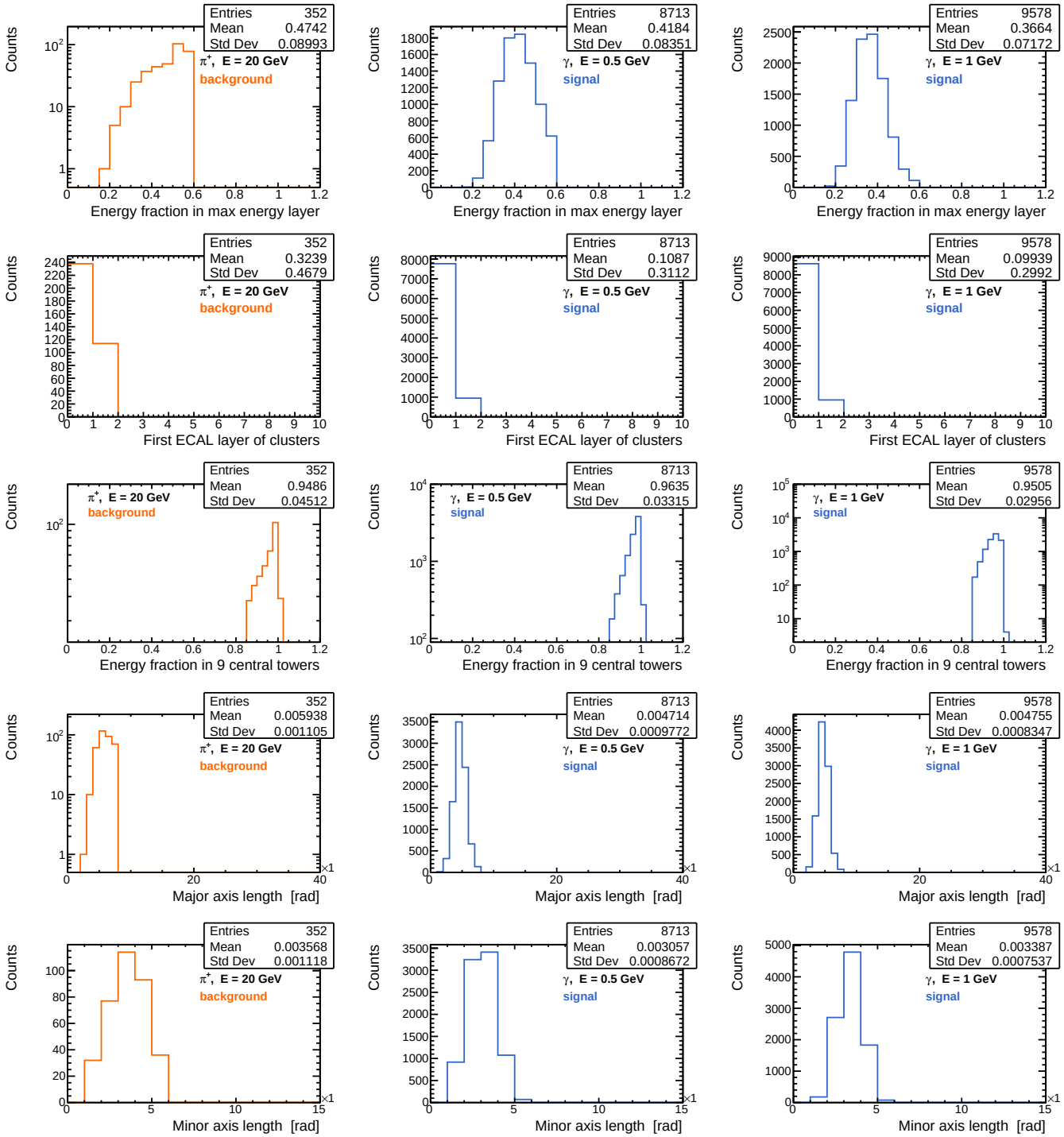

Figure C.5: Distributions of cutting variables for FPK for both background and signal samples after appplying cut $0.001 < minor \leq 0.005$.

Appendix D Optimizing the migration matrix

There are two optimization schemes implemented for the formation of the migration matrix. The first is a suppression of radiation photons and will be presented in Appendix D.1. The second is a method to tackle events where the $\pi^{\pm}$ and π^{0} clusters have merged and is presented in Appendix D.2.

Appendix D.1 Suppression of radiation photons

Figure D.1 shows the the invariant mass distribution of the charged pion and either a related and radiation photon. A cut of $0.2 < m_{\pi^{\pm},\gamma} < 1.8$ GeV is enforced to identify and dismiss the radiation photons and the limits are set based on Figure D.1. Only photons obeying this cut are considered genuine photons, even if they passed through the PFK.

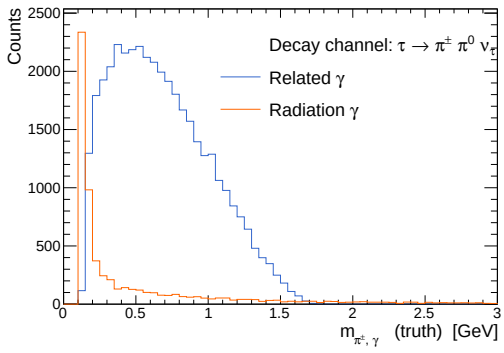

Figure D.1: The mass of $\pi^{\pm}$ and photons for both related and radiation photons

Appendix D.2 Events with merged clusters

To identify merged clusters of $\pi^{\pm}$ and π^{0}'s a limit of $E/p \leq 1.2$ is enforced. It is trivial that a cluster exceeding this value will contain more than the charged pion, but this appendix provides a more detailed discussion of the optimization concerning these events.

Figure D.2 shows the number of genuine photons in an events vs. angluar distance from the charged pion to the neutral pion. It demonstrates that the closer the

photon is to the $\pi^{\pm}$, the fewer genuine photons are observed, which means that the two clusters probably merged. It is therefore likely that events without genuine photons contain such a merged cluster. Figure D.3 then shows the E/p separation variable for these zero and two genuine photon events. The distribution for non-merged clusters have $E/p < 1.$ as expected whereas the merged clusters can have a much larger E/p-value. This parameter can therefore be used to separate the two.

For the identified merged events containing no single residual π^0's, Figure D.4 shows the difference in observed and generated π^0's. The fact that only one π^0 is merged in most events for all decay channels, justifies the approximation of counting the merged cluster as one missing π^0. For the $\pi^{\pm}3\pi^0\nu$ channel, this simplified method is less effective, but as the polarisation measurements are less sensitive to this channel, it is most important that it is optimized to the hadron and $\pi^{\pm}\pi^0\nu$ channels. The optimization generally counteracts the feed-down mechanism without disturbing the already correctly classified events and is therefore used in this analysis. However, developing an improved method is still important for future studies.

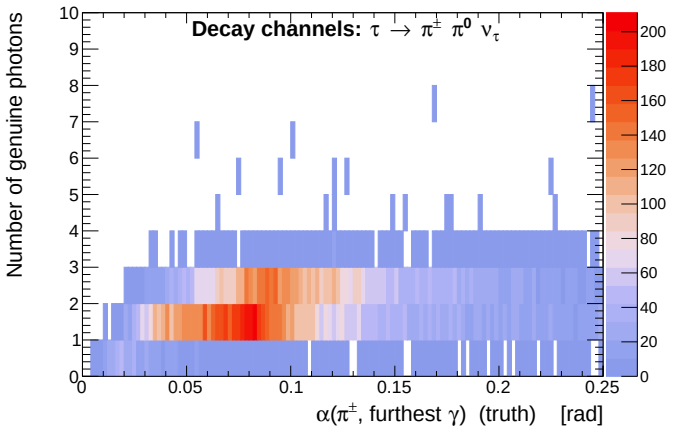

Figure D.2: The number of reconstructed genuine photons vs the angle between the charged pion and the furthest daughter photon of a π^0

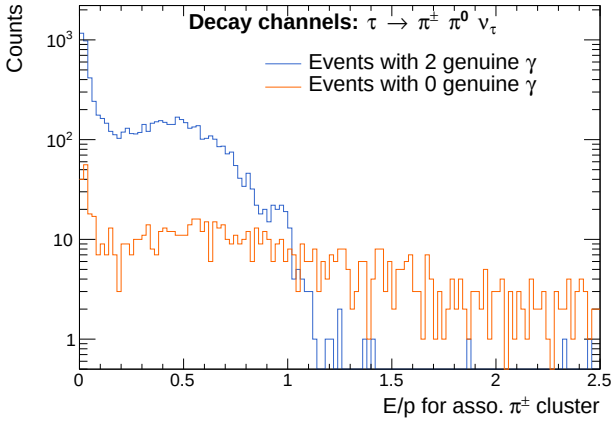

Figure D.3: The E/p value of events with and without genuine photons for the $\tau \to \pi^{\pm}\pi^{0}\nu$ channel

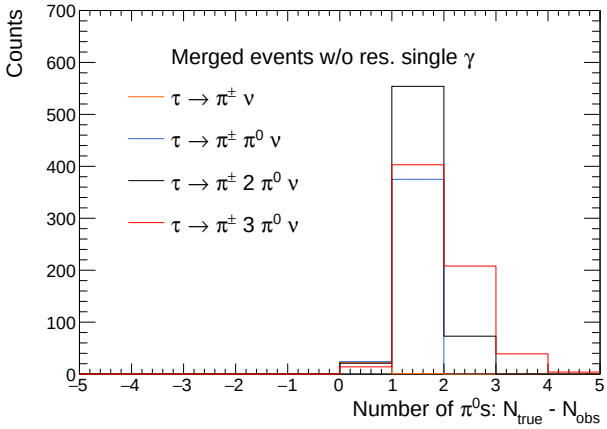

Figure D.4: The difference between observed and generated π^{0}'s in merged events

Appendix E S-curve correction for the revised LAr ECAL

Figure E.1 shows the difference between the position of the cluster and the truth position as a function of the cluster position in the ϕ and z directions for photons in the revised LAr ECAL. The figures show a clear s-curve structure. This distribution is then projected onto a 2D plot and fitted with a sine curve, which can be seen in Figure E.2. The fit result is used as a position correction. The resulting differences for the cluster and truth positions in ϕ and z are shown in Figure E.3. The correction has successfully straightened the s-curve which also increases the position resolution.

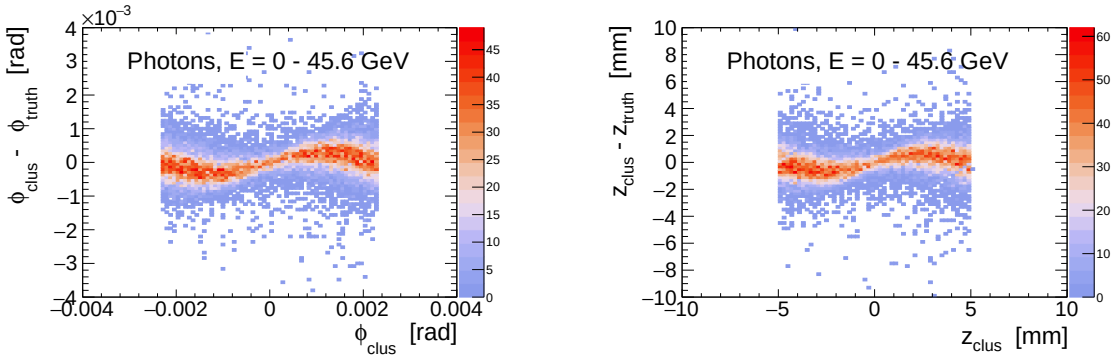

(a) ϕ coordinate **(b)** z coordinate

Figure E.1: Difference in coordinate (ϕ and z) between generated particle and reconstructed cluster versus reconstructed coordinate within one cell width

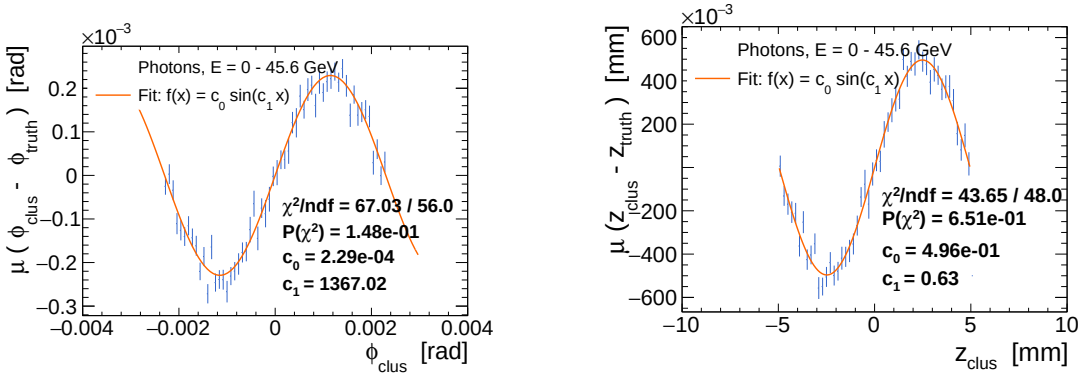

(a) ϕ coordinate **(b)** z coordinate

Figure E.2: Difference in coordinate (ϕ and z) between generated particle and reconstructed cluster versus reconstructed coordinate within one cell width fitted with a sine function

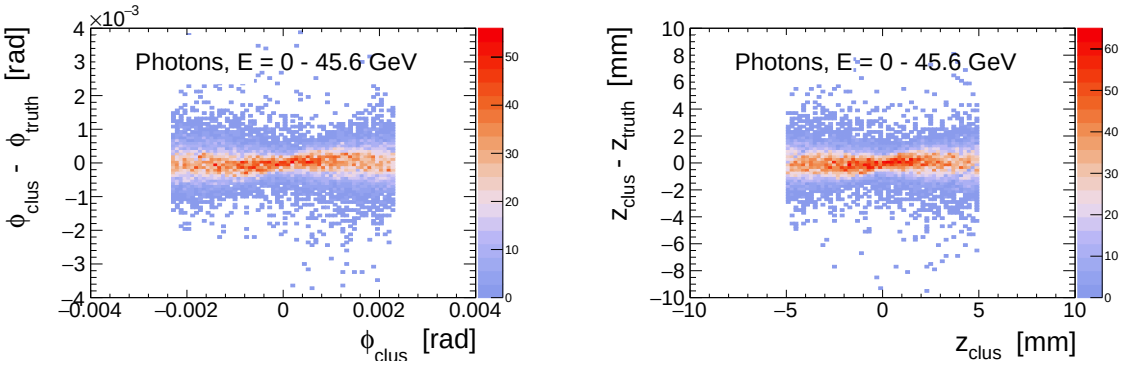

(a) ϕ coordinate **(b)** z coordinate

Figure E.3: Difference in coordinate (ϕ and z) between generated particle and reconstructed cluster versus reconstructed coordinate within one cell width after s-curve correction

Appendix F S-curve correction for the LKr ECAL

Figure F.1 shows the difference between the position of the cluster and the truth position as a function of the cluster position in the ϕ and z directions for photons for the LKr ECAL. The distribution is s-shaped due to the s-curve phenomenon. This distribution is then projected onto a 2D plot and fitted with a sine curve. This fit can be seen in Figure F.2. The fit result can be used as a position correction to increase the overall position resolution. The resulting differences in the cluster and truth positions in ϕ and z is shown in Figure F.3 and it is clear that the correction has successfully straightened the s-curve.

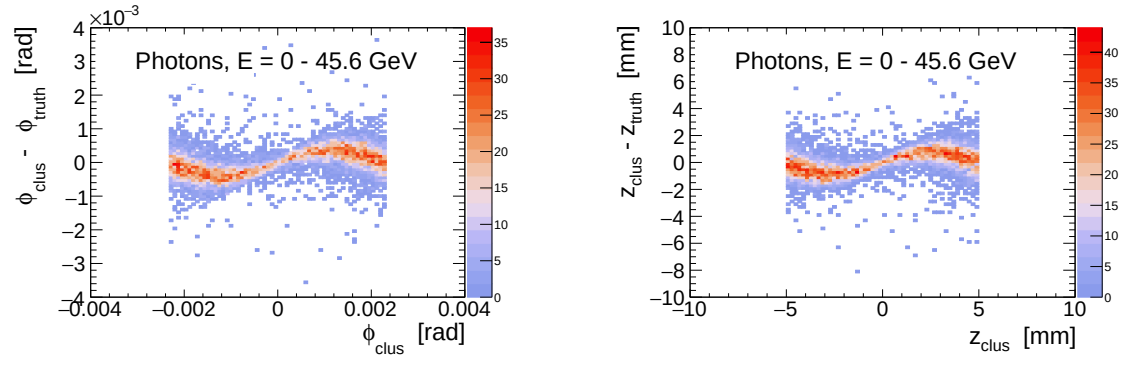

(a) ϕ coordinate **(b)** z coordinate

Figure F.1: Difference in coordinate (ϕ and z) between generated particle and reconstructed cluster versus reconstructed coordinate within one cell width

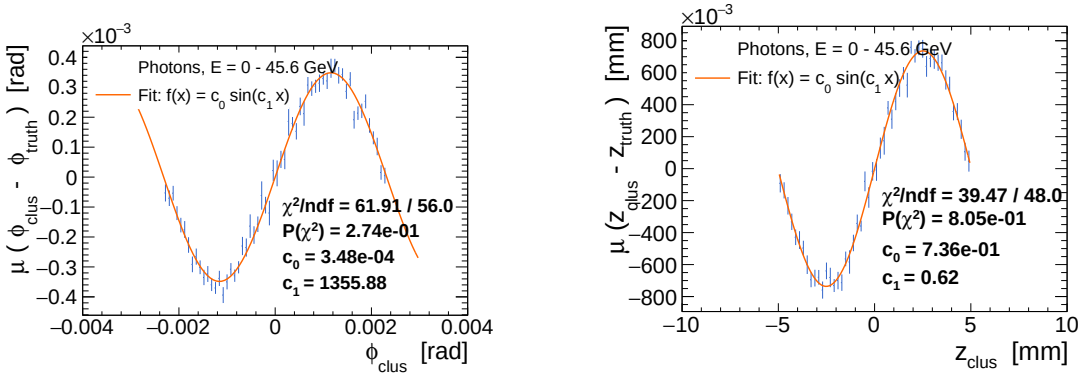

(a) ϕ coordinate **(b)** z coordinate

Figure F.2: Difference in coordinate (ϕ and z) between generated particle and reconstructed cluster versus reconstructed coordinate within one cell width fitted with a sine function

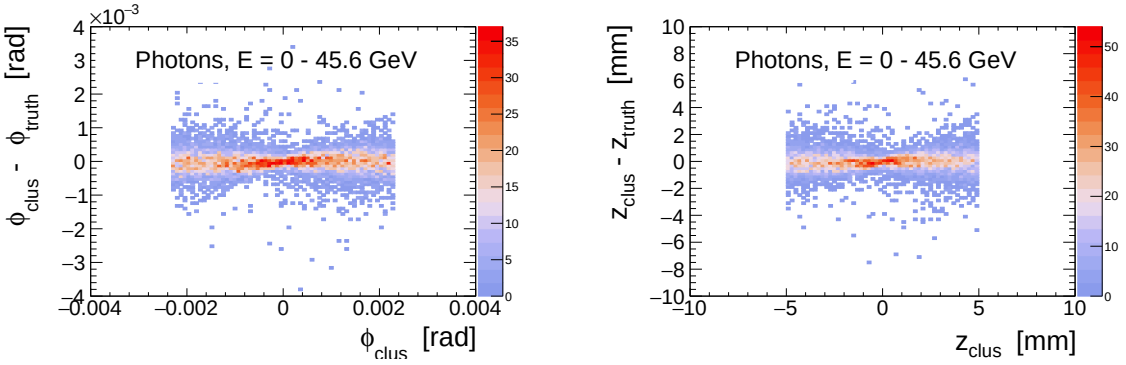

(a) ϕ coordinate **(b)** z coordinate

Figure F.3: Difference in coordinate (ϕ and z) between generated particle and reconstructed cluster versus reconstructed coordinate within one cell width after s-curve correction